“Oxidation-Nitridation of Chromium at High Temperatures and its Mitigation by Alloying”

Von der Fakultät für Georessourcen und Materialtechnik der
Rheinisch -Westfälischen Technischen Hochschule Aachen

zur Erlangung des akademischen Grades eines

Doktors der Ingenieurwissenschaften

genehmigte Dissertation

vorgelegt von **Dipl.-Ing.**

Ali Soleimani-Dorcheh

aus Khomini Shahr, Iran

Berichter: Prof. Dr.-Ing. Michael Schütze
Univ.- Prof. Dr.-Ing. Wolfgang Bleck

Tag der mündlichen Prüfung: 20. Januar 2017

Schriftenreihe des DECHEMA-Forschungsinstituts

Band 12

Ali Soleimani-Dorcheh

Oxidation-Nitridation of Chromium at High Temperatures and its Mitigation by Alloying

Shaker Verlag
Aachen 2017

Bibliographic information published by the Deutsche Nationalbibliothek
The Deutsche Nationalbibliothek lists this publication in the Deutsche Nationalbibliografie; detailed bibliographic data are available in the Internet at http://dnb.d-nb.de.

Zugl.: D 82 (Diss. RWTH Aachen University, 2017)

Printed in Germany.

ISBN 978-3-8440-5078-3
ISSN 2197-6155

Shaker Verlag GmbH • P.O. BOX 101818 • D-52018 Aachen
Phone: 0049/2407/9596-0 • Telefax: 0049/2407/9596-9
Internet: www.shaker.de • e-mail: info@shaker.de

ABSTRACT

This work investigates oxidation and nitridation in the binary Cr-Si system. Kinetics and thermodynamics of oxidation in this alloy system have been investigated with a systematic approach. Oxidation and nitridation behavior of each individual phase (solid-solution phase, Cr_{ss} and silicide phase, A15) were studied separately by investigating the oxidation and nitridation kinetics for short and long term exposures, thermodynamic stability, and post-exposure characterization of the scale, and subscale morphologies. Results revealed that in both phases chromium is the predominant element in the oxidation process which made such alloys major chromia formers. It was found, however, that the role of localized SiO_2 formation in reducing oxidation kinetics is significant. The oxidation rate of chromium was reduced by more than an order of magnitude upon the addition of only 3 at.% Si. The impact of SiO_2 increased further with increasing Si content. The A15 Cr_3Si silicide phase produced a continuous SiO_2 layer at long term exposures. When combined in a two-phase eutectic alloy, both solid-solution and A15 silicide phases oxidized cooperatively via primary depletion of chromium which led to the dissolution of the Cr_{ss} phase and formation of an A15 layer at the alloy-scale interface. The influence of nitrogen as an important oxidant in air was investigated for pure chromium and the binary Cr-Si alloys and it was shown that a chromium subnitride layer exclusively grew via inward diffusion of nitrogen. The positive role of Si in hindering nitridation was significant. It was revealed that the A15 silicide is stable at any nitrogen pressure at high temperatures and showed almost no solubility for nitrogen. As a continuous barrier in the subsurface region of the two phase eutectic $Cr-Cr_3Si$ alloy, it offered a self-protecting character against internal nitridation. Further development of this alloy system was conducted after exploring the ternary Cr-Ge-Si system in the high chromium range (Cr > 80 at.%). Si and Ge showed interchangeable solubility in both solid-solution Cr_{ss} and A15 phases, and addition of Ge stabilized the A15 phase by supporting the peritectic reaction in the $Cr-Cr_3Ge$ system. The microstructure of the eutectic alloy remained fine-lamellar when up to 2 at.% Ge was added. Using this approach, nitridation, as the most important challenge in the development of chromium alloys, was significantly improved as the alloy microstructure remained unaffected from internal nitridation for a period of 1000 hours oxidation at 1200°C in air. Finally, the optimized oxidation behavior of binary and ternary alloys was discussed with regards to the morphology and adhesion of the chromia scale.

KURZFASSUNG

In der vorliegenden Arbeit wird die Nitrierung und Oxidation im Cr-Si Binärsystem untersucht. Die Kinetik und Thermodynamik beider Reaktionen sind mittels eines systematischen Ansatzes beschrieben. Die Nitrierung und Oxidation einzelner Phasen wie beispielsweise dem Cr-Mischkristall und der A15-Silizidphase wurden mittels Kurz- und Langzeitauslagerungen, thermodynamischen Stabilitätsberechnungen und Charakterisierung von Oxidschicht und Substrat untersucht. Die Ergebnisse zeigen, dass Chrom in beiden Phasen das dominierende Element im Oxidationsprozess ist. Dies macht diese Legierungsklasse vorwiegend zu Chromoxidbildnern. Die lokale Bildung von SiO_2 wurde trotzdem beobachtet, welches einen signifikanten Einfluss auf die Oxidationsresistenz des Werkstoffs zeigt.

Eine Zugabe von lediglich 3 atom% Si zu Chrom erzielte eine Verbesserung der Oxidationsbeständigkeit um mehr als eine Größenordnung. Der positive Einfluss von SiO_2 wurde durch weitere Si-Zugabe erhöht. Die A15-Silizidphase (Cr_3Si) bildet sogar eine durchgängige SiO_2-Schicht während Langzeitauslagerungen.

Die Kombination beider Phasen im Rahmen eines eutektischen Gefüges führt zu einer gleichzeitigen Oxidation mit vorwiegender Chromverarmung. Dies ruft eine Auflösung der Chrom-reicheren Phase bzw. des Chrommischkristalls und eine damit einhergehende Bildung einer A15-Silizidschicht in der Randzone hervor.

Der Einfluss von Stickstoff als ein wichtiger Oxidant in Luft wurde sowohl für reines Chrom als auch für die binären Cr-Si-Legierungen untersucht. Das innere Wachstum einer Chromnitridschicht in der Substratrandzone beweist eine explizite Einwärtsdiffusion von Stickstoff. Es wurde beobachtet, dass Si eine besondere Rolle spielt um die Nitrierung zu verhindern. Die A15-Silizidphase zeigte hervorragende Stabilität unter jeglichen Stickstoffpartialdrücken bei hohen Temperaturen und eine nur sehr geringe Löslichkeit für Stickstoff. Als eine kontinuierliche Barriere in der Randschichtzone der zweiphasigen Cr-Cr_3Si-Legierung bietet die A15-Phase selbstschützenden Charakter gegen innere Nitrierung.

Diese Legierungsklasse wurde nach intensiver Untersuchung des ternären Cr-Ge-Si Systems im hochchromhaltigen (Cr > 80 atom.%) Bereich weiterentwickelt. Si und Ge zeigten eine austauschbare Löslichkeit sowohl im Chrommischkristall als auch in der A15-Phase. Die Zugabe von Ge stabilisiert die A15-Phase durch eine gezielte Förderung der peritektischen Reaktion im Cr-Cr_3Ge-System. Die Mikrostruktur der eutektischen Legierung bleibt bis zu einer Zugabe von 2 atom. % Ge fein-lamellar. Mittels dieses Ansatzes konnte der Wiederstand gegen Nitrierung als eine der größten Herausforderungen in der Entwicklung von Chromlegierungen deutlich verbessert werden. Die Mikrostruktur der Legierung blieb vor innerer Nitrierung während Oxidationstests von 1000 Stunden bei 1200°C an Luft bewahrt.

Das optimierte Oxidationsverhalten der binären und ternären Legierungen wird in Bezug auf Morphologie und Haftung der Chromoxidschicht diskutiert.

ACKNOWLEDGEMENTS

The present work has been conducted at the DECHEMA-Forschungsinstitut, Frankfurt am Main. The project was financially supported by the German Research Foundation (DFG) which is gratefully acknowledged.

Foremost, I would like to thank DECHEMA-Forschungsinstitut, specially the Chief Executive, the head of high temperature materials group, and the advisor of this work Prof. Michael Schütze, for the trust, support, and for sharing his excellent knowledge with me.

I express my deepest gratitude to Dr. Mathias Galetz, the supervisor of this work, for his unreserved support and guidance over the past four years.

My sincere thank goes to my co-advisor and committee member, Professor Wolfgang Bleck, the head of the department of Ferrous Metallurgy at RWTH Aachen University, for providing the chance to submit this work at the RWTH Aachen.

Prof. Wolfgang Donner at Darmstadt University of Technology is thanked for performing x-ray diffraction measurements. Ms. Shan Chin of ThermoCalc is thanked for thermodynamic activity calculations. Professor George Smith of Oxford University is thanked for his valuable discussions. Dr. Rick Durham is thanked for proofreading the thesis.

I would like to especially thank my colleagues and friends at the High Temperature Materials group of the DFI, for the friendly and warm atmosphere that they provided during my stay which made me enjoy working at the HTW and for many ordinary moments they made extraordinary for me.

Not least, I would like to thank my family, especially my wife, for her understanding, patience, and assistance during writing this thesis.

CONTENTS

LIST OF TABLES

LIST OF FIGURES

LIST OF SYMBOLS

T	Temperature
m	Mass
t	time
G°	Standard free energy
x	Oxide thickness
x_{sc}	Oxide thickness under the chromia single crystal
k_p	Parabolic rate constant in air
k_v	Linear volatilization rate
k_p^{ox}	Parabolic rate constant in oxygen
k_p^{nit}	Parabolic rate constant in nitrogen
Ω	Oxide volume per unit quantity of diffusing species
C_x	Concentration
D	Inter-diffusion coefficient
ϕ	Average grain size
δ	Grain boundary width
P_{O_2}	Oxygen partial pressure
P_{N_2}	Nitrogen partial pressure
Q	Activation energy
K_{eq}	Equilibrium constant
M_{O_2}	Molecular weight of oxygen
f_{cr}	Mass fraction of Cr in Cr_2O_3
A	Surface area
δ	Grain boundary width
μ	The ratio of oxygen anions to metal cations in oxide
$N_{c,Si}$	Critical concentration of Si
V_A	Molar volume of alloy

1 INTRODUCTION

High temperature materials play a key role in gas turbine engines used for aircrafts and power plants providing modern transportation and enable us to have reliable source of power generation. The development of such engines has always been dependent upon materials. In order to operate safely and efficiently, they require materials which can withstand extreme conditions such as high temperature, high pressure and corrosive environments. Over the past 70 years, the development of these engines has relied on the development of nickel base superalloys which are the most studied and the most sophisticated high temperature structural materials. Over time, their high temperature capability has been increased from around 700°C to the current 1150°C thanks to material development strategies including additions of more than 13 alloying elements to stabilize microstructure, enhance mechanical properties, and increase oxidation resistance [1].

A further increase in operating temperature nowadays is achieved by designing complex cooling systems in turbine blade structures (see Figure 1-1). Nevertheless, cooling systems decrease the efficiency when added to the turbine blade structure (Figure 1-1). On the other hand, a further increase of temperature is limited, since even the most advanced single crystal nickel base superalloy starts to soften beyond 1150°C [2]. The ever increasing demand for higher efficiencies to reduce the fuel consumption and accordingly the CO_2 emission is still urging the materials science community to develop a novel alloying system which can go beyond the capability of nickel base superalloys [1,3-5].

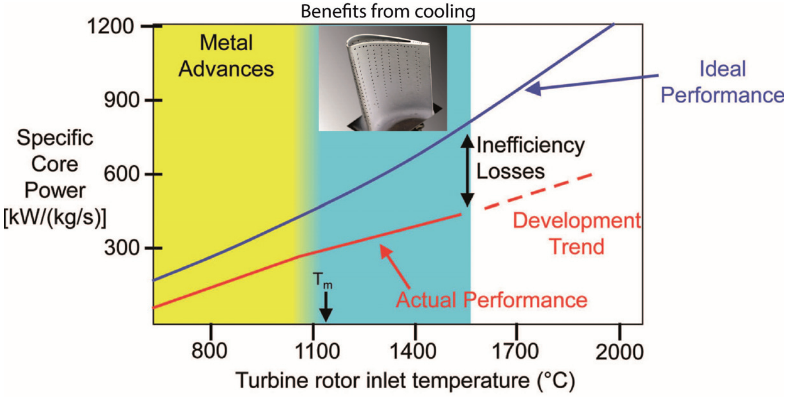

Figure 1-1. The relation between thermal efficiency and turbine inlet temperature in jet engines (after Lemberg et al. [4], with kind permission from John Wiley and Sons).

Intermetallic reinforced refractory alloys based on Mo, Nb, and Cr have recently been considered as possible candidates for high temperature structural applications [5-10]. Among these alloys, Cr-based alloys offer interesting physical and mechanical properties including high specific modulus of elasticity, low-density, high oxidation resistance and high creep resistance.

Several classes of chromium alloys strengthened with Laves phase Cr_2X (X= Ta, Nb, Hf, Zr, etc.) or A15 phase (Cr_3Si) have been recently developed and classified as "in-situ composites" [11-14]. The Cr-Cr_3Si eutectic alloy offers a lamellar microstructure with a toughening chromium solid-solution phase and an intermetallic A15 silicide (Cr_3Si) phase providing improved mechanical strength at high temperatures. Studies on these alloys in the literature are limited to those on the mechanical properties of the single phase Cr_3Si and the Cr_{ss}-Cr_3Si system [15-17]. Bei and coworkers showed that the microstructural parameters such as lamellar spacing can be tuned during solidification which provides diverse mechanical properties [18]. They showed later that the micro-alloying of Re and Ce improves the stability of the lamellar microstructure at high temperatures [19]. Based on the attractive physical properties and mechanical and microstructural stability at high temperature, it is clear that Cr-Cr_3Si alloys show high potential as candidates for future high temperature structural applications [2].

Nevertheless, the oxidation behavior of this class of alloys and generally the Cr-Si system has not yet been systematically studied. In addition, it is known that nitridation plays a significant role during oxidation in atmospheric air. It was found that the room temperature brittleness of chromium is to a high extent correlated to the impurity contents such as nitrogen [20-22]. Even worse, when exposed to nitrogen containing atmospheres such as air at high temperatures, inward diffusion of nitrogen in chromium forms a brittle nitride phase which drastically reduces the life time of the material at high temperatures [23].

Germanium alloying in several binary and ternary silicide systems was found to be beneficial for high temperature oxidation resistance [24,25]. Binary Cr-Si [26] and Cr-Ge [27] systems show a similar Cr solid-solution and an intermetallic phase with A15 structure (Cr_3Si and Cr_3Ge) in the chromium-rich parts within a nearly similar range of composition (13-22.4 at.% Si and 11.8-20.3 at.% Ge for Cr-Si). The unique feature that makes the ternary system interesting is that Cr_{ss} and the intermetallic phase undergo a eutectic and peritectic transformation in Cr-Si and Cr-Ge systems, respectively.

In this work, the high temperature oxidation and nitridation behavior of chromium-silicide based alloys in binary Cr-Si and ternary Cr-Ge-Si systems is studied. First, a systematic study is conducted to understand the high temperature oxidation and nitridation behavior in the Cr-Si binary system. The major focus is to investigate thermodynamics and kinetics of oxidation (nitridation) for each individual phase and correlate them to the behavior of the two phase eutectic alloy. Based on expected improvements from Ge, the Cr-Ge-Si system at the high chromium end (Cr > 80 at.%) is studied next. The influence of germanium additions on the microstructural evolution and crystallographic structure of the two phase Cr_{ss}-A15 system is studied and the unknown part of the phase diagram at the high chromium end is experimentally assessed. Finally, the high temperature oxidation and nitridation behavior of the ternary Cr-Ge-Si alloys was studied and an optimized composition with highest oxidation (nitridation) resistance is determined.

2 STATE OF THE ART

Chromium is widely utilized as an alloying element in engineering alloys such as stainless steels and Ni-based alloys due to the formation of a protective chromia scale (Cr_2O_3). Nevertheless, pure chromium and Cr-based alloys have not become engineering structural materials because of their brittleness and poor ductility at both ambient and elevated temperatures. It is known that Cr, as a bcc metal is inherently brittle at room temperature due to the limited number of primary dislocation slip systems in their crystal structures. However, it was found that the ambient temperature brittleness of chromium can be significantly improved by increasing its purity [28-31].

When exposed to air at high temperatures, embrittlement can also be induced via formation of brittle subnitride underneath the oxide scale [32,33]. Further, the oxidation resistance of chromium decreases at high temperatures (T> 1000°C) due to a high scaling rate and oxide volatilization [34-36].

Unlike other refractory candidates for high temperature structural applications (such as Mo-based and Nb-based alloys), chromium alloys have not been consistently studied and the data are rather scattered. Intensive work has been done during the 1950s on developing ductile chromium via the iodide electro refining purification process [21,22,28,29,37]. Considerable research has also been conducted during the 1950s and 1970s to understand the oxidation kinetics of chromium and the behavior of the chromia scale at high temperatures [38,39,39-41]. Nevertheless, many issues such as mass transport in the chromia scale, oxidation kinetics, effects of multi-oxidant atmospheres, effects of alloying elements on oxidation and mechanical properties of chromium etc. remain unclear. Due to the drawbacks mentioned above, the interest in chromium was short lived and further studies on the development of Cr-based alloys were suspended for decades.

The ever increasing demands to develop novel alternative alloys for high temperature applications and the promising properties of chromium including high melting point (1907°C), low density of 7.15 g/cm^3 (~20% lower than most nickel-base superalloys), high thermal conductivity (two to four times higher than most superalloys), and competitive pricing, have recently attracted attention to develop novel Cr-based alloys [20,42,43]. Room temperature ductility, high temperature strength, and high temperature oxidation resistance (at T> 900 °C) are still the major challenges.

In the following, the oxidation behavior of chromium and chromium alloys starting from the earlier works of Gulbransen, Hagel, Lillerud and Kofstad [39,41,44] and ending with the most recent studies are reviewed. The effect of experimental parameters such as temperature, oxygen partial pressure, and multi-oxidants on the kinetics of oxidation and the stability of oxidation products are discussed. Finally, recent trends in the development of Cr-based alloys are summarized.

2.1 Thermodynamics of chromium oxidation

Chromia (Cr_2O_3) is the most stable form of chromium oxides at high temperatures. It has a corundum structure consisting of a hexagonal close packed sublattice of anions with 2/3 octahedral sites occupied by chromium. Cr_2O_3 is stable when the oxygen partial pressure in the environment is greater than the equilibrium partial pressure of the oxide (also known as dissociation pressure).

$$2Cr + \frac{3}{2}\,O_2 = \,Cr_2O_3 \tag{1}$$

$$\Delta G^{\circ} = -1{,}120{,}270 + 259.83\mathrm{T}\ \mathrm{Jmol}^{-1} \tag{2}$$

The Ellingham-Richardson diagram, Figure 2-1, is utilized to show the standard free energy of formation for oxides as a function of temperature, and equilibrium oxygen partial pressure [34,45]. Cr_2O_3 belongs to the most stable oxides (together with Al_2O_3 and SiO_2), i.e. the equilibrium partial pressure is extremely low and a very low amount of oxygen in an atmosphere is sufficient to form a stable protective layer of these oxides.

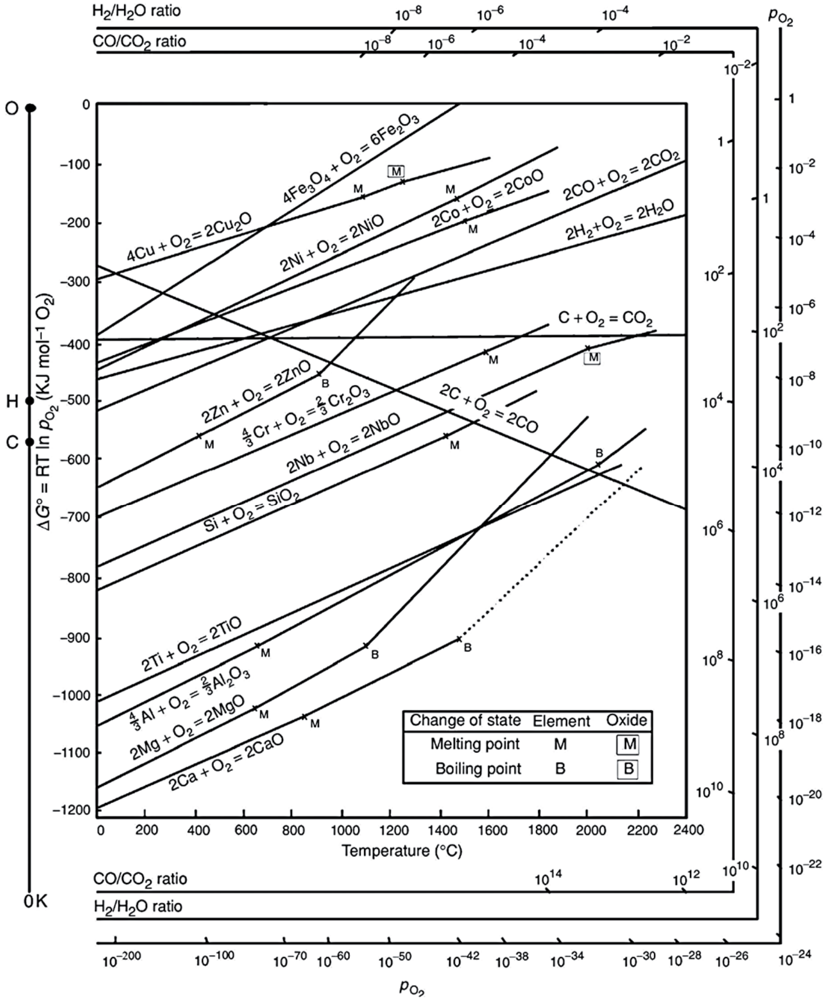

Figure 2-1. Ellingham-Richardson diagram for selected elements. After [46].

2.2 Oxidation kinetics

Formation of an adherent, compact and continuous scale which prevents the direct contact between the metal substrate and the oxidizing gas is required for protection at high temperatures. For oxidation of chromium to proceed further, it is then necessary that one or both ions are transported through the Cr_2O_3 scale. Wagner showed that the growth of the compact scale is controlled by the diffusion of ionic species through the scale that ideally follows a parabolic relation:

$$x^2 = 2\,k_p t \tag{3}$$

where x is the scale thickness, t is the exposure time, and k_p is the parabolic rate constant [47]. According to Wagner's theory of oxidation, the mass transport of anions and cations along the scale occurs based on two distinct driving forces: the electric field and the chemical potential gradient across the oxide scale. He related the parabolic rate constant to the diffusion rate of ionic species in the oxide scale using Eq. 4:

$$k_p = \Omega D(C_1 - C_2) \tag{4}$$

where Ω is the oxide volume per unit quantity of diffusing species, D is the diffusion constant, and C_1 and C_2 are the concentrations of diffusing components at the metal-scale and scale-gas interfaces, respectively [45]. However, Wagner's theory describes an ideal situation based on the following assumptions [46]:

a. The oxide scale is adherent and compact.

b. The ionic (electronic) diffusion across the scale is the rate-controlling step.

c. Thermodynamic equilibrium is established throughout the scale and at both the metal–oxide and oxide–gas interfaces.

d. Oxygen solubility in the metal is neglected.

e. The metallic substrate is pure.

2.3 Chromia growth mechanisms

The growth mechanism of a Cr_2O_3 scale has been previously studied for a wide range of temperatures [35,41,48]. It can be generally regarded as a mechanism involving two major steps: a) initial oxidation or thin film growth b) second stage oxidation or thick film oxidation. The initial oxidation stage is related to the formation of a thin oxide film while second stage oxidation is considered when the oxide film has a thickness higher than 1µm.

The mechanism of oxidation at each stage was studied by Young and Cohen [49]. As they oxidized chromium at moderate temperatures (300-600°C), an abrupt transition was observed in oxidation kinetics. In addition, a distinct difference was observed in the structure and morphology for the grown chromium oxide. The diffraction pattern of the oxides showed a transition from a randomly oriented fine grained chromia deriving from the initial oxidation stage to a strongly oriented fibrous grain structure at higher oxide thicknesses [49]. Hope and Ritchie verified that an amorphous chromia film forms at the initial stage of oxidation below 300°C, while above 400°C it starts to crystallize [50]. The finer grain structure of the initially grown oxide provides a higher density of preferred diffusion path ways for mobile species and leads to a uniform film thickening. On the other hand, a lower density of diffusion paths at the later oxidation stage (at higher temperatures) causes the formation of ridges and nodules which correspond to local transport paths through the oxide film.

Greogry et al [48] detected a transition temperature of 350°C above which the oxidation behavior obeys the parabolic law (thick film) while below it follows the logarithmic rate law (thin film). The parabolic relation is applicable up to the range of 800 [51] to 900°C [34] to describe the chromium oxidation kinetics. At higher temperatures it deviates from the ideal parabolic behavior due to volatilization, loss of metal-oxide contact, and formation of mechanical defects i.e. wrinkles, buckling and cracking [51-54].

2.4 Defect structure in Cr_2O_3

Chromia is a non-stoichiometric oxide with Cr deficiency. Its non-stoichiometry is however, very small. Experimental data on the self-diffusion behavior and electrical conductivity of chromia revealed a complex defect structure in chromia [55-66]. It is known that chromia is an intrinsic electronic conductor at temperatures above 1000°C [58,59]. Thermoelectric measurements by Young et al. and Kofstad et al. at high temperatures showed that chromia is an n-conductor at low oxygen activities (down to the decomposition oxygen partial pressure) and a p-conductor at near atmospheric oxygen activities [55,58,59]. Furthermore, self-diffusion studies by Hagel and Seybold, Hochioni et. al. and later Sabioni et al. indicated that the self-diffusion coefficient of chromium is inversely related to the oxygen partial pressures at partial pressures close to the decomposition pressure of chromia [61-65,67]. Considering both electronic conductivity and self-diffusion behavior of chromia at high temperatures, it could be concluded that the defect structure in chromia depends on oxygen partial pressure. The above mentioned observations indicate that point defects with positive effective charge e.g. Cr interstitials ($Cr_i^{\cdot\cdot\cdot}$) predominate at reduced oxygen partial pressures. At near atmospheric partial pressures, however, defects with negative effective charges e.g. chromium vacancies (V_{Cr}''') predominate. It should be mentioned that due to the extremely slow self-diffusion rate of Cr (e.g. 10^{-17} cm^2s^{-1} at 1000-1300°C), an equilibrated state cannot be obtained in reasonable time scales. Thus, assuming the equilibrium state for thermally grown chromia on a pure Cr substrate, it can be concluded that the chromium self-diffusion process at the oxide-substrate interface is controlled by chromium interstitials ($Cr_i^{\cdot\cdot\cdot}$) while the process is controlled by chromium vacancies (V_{Cr}''') at scale-oxygen interface.

2.5 Effective parameters on oxidation kinetics

The parabolic oxidation kinetics of chromium depends significantly on the oxidizing conditions such as temperature, oxygen partial pressure (P_{O_2}), and oxidizing components. The study of parameters affecting the oxidation kinetics of chromium at high temperatures is mainly limited to the early works from the 1980s-1990s. Due to the importance of these effects their conclusions are briefly summarized below.

2.5.1 Effect of temperature

Figure 2-2 illustrates an updated summary of k_p values reported for chromium at temperatures above 900°C [34,35,41,54,60,68,69].

A noticeable difference of up to four orders of magnitude in parabolic rate constant values can be noted. This difference was attributed to the specimens surface conditions, experimental parameters, and measurement methods (e.g. continuous and discontinuous gravimetry [68]). Experimental parameters such as metal microstructure, surface conditions [34], and metal impurities (such as hydrogen and sulfur) [70-73] are reported to affect the oxidation kinetics of chromium metal. Most of these parameters directly affect the oxide morphology, which in turn, leads to different oxidation rates [54]. For instance, Caplan and Sproule reported more than eight times higher oxidation rates for electro-polished chromium than for etched chromium under similar oxidizing conditions [54]. This difference was attributed to the difference between a monocrystalline and a polycrystalline chromia layer formed on etched chromium and electro-polished chromium, respectively. Polycrystalline chromia is known to grow much faster as a result of the grain boundary contribution in the diffusion process [45,54]. It is surprising, however, that despite significant scatter in the parabolic rate constants no recent experimental data has been found to further investigate this problem.

Figure 2-2 also indicates that oxidation kinetics shows a typical Arrhenius dependence on temperature,

$$k_p = k_0 exp\left(\frac{-Q}{RT}\right) \tag{5}$$

where Q is the activation energy of oxidation, T is temperature, R is the gas constant, and k_0 is a constant which is typical for each metal [45]. A list of activation energies for the Cr/Cr_2O_3 system in oxygen atmosphere is given in Table 2-1. Considering the above discussed reasons, it is not surprising that scattering activation energies are reported for similar oxidizing atmospheres.

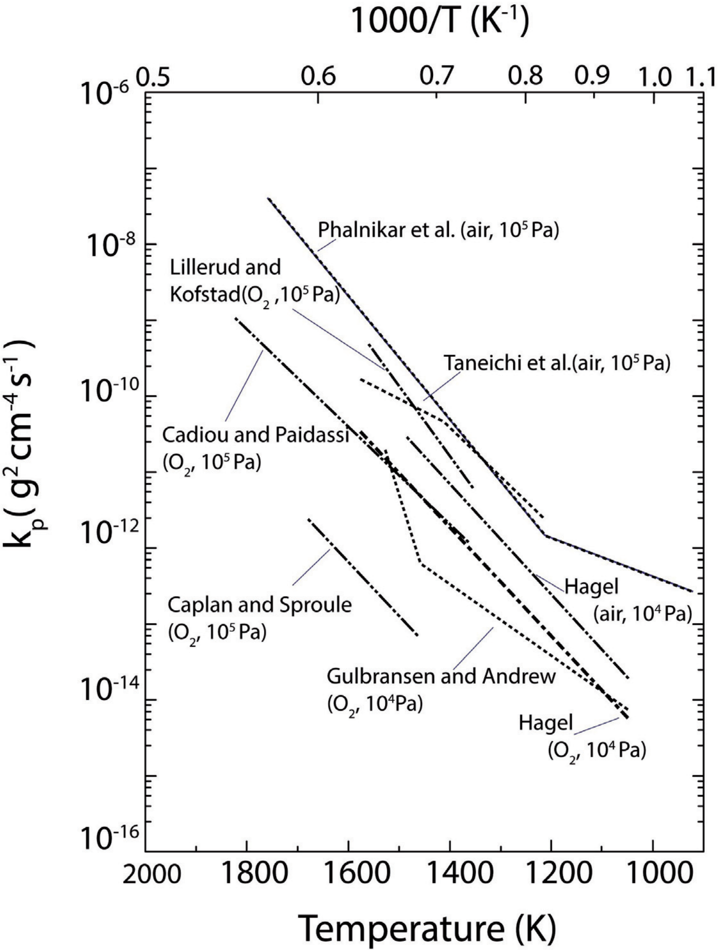

Figure 2-2. The parabolic rate constant values (k) for oxidation of pure chromium as a function of temperature in different studies. After [68].

Table 2-1. Reported activation energies for oxidation of chromium.

Gas	*T(°C)*	*Q (kJmol^{-1})*	*Reference*
O_2 (1atm)	980-1200	243	[54]
O_2 (0.1atm)	700-950	156	[39]
O_2 (0.1atm)	1000-1100	248	[39]
O_2 (0.1atm)	700-900	277	[35]
O_2 (1atm)	900-1075	330	[44]

2.5.2 Effect of oxygen partial pressure

The effect of oxygen partial pressure on the parabolic kinetics depends, to a high extent, on the experimental conditions. Thus, a comparison between different works with different experimental conditions with regards to surface treatment, impurity level, and the components of the low P_{O_2} atmosphere would lead to inconsistent results.

Kofstad and Lillerud showed the oxidation kinetics of chromium at constant oxygen pressures between 7× 10^{-7} and 1 atm. (using pre-vacuum and dosing oxygen) at 1000°C and revealed a negative dependence of oxidation kinetics on P_{O_2} [44,60]. Such behavior is not in agreement with a diffusion-controlled mechanism based on Wagner's theory and the unusual P_{O_2} dependence was attributed to the morphology and microstructure of the oxide scale during growth as extensive buckling, cracking, and wrinkling took place at low oxygen partial pressures. Comparing this behavior with the morphology of oxide at higher P_{O_2}, it is concluded that (1) scale deformation and cracking result from large stresses and strains in the scale during growth and (2) the plasticity of oxide extensively increases at lower P_{O_2} [52] which results in extensive formation of wrinkles and ridges in the chromia scale. They also proposed that near the metal-scale interface chromium ion interstitials are the predominating defects while at near atmospheric pressures chromium vacancies predominate. This has been proven in diffusion studies and conductivity measurements conducted in a temperature range of 1100-1600°C [58,59,59]. However, Hagel measured the influence of P_{O_2} on the parabolic rate constant of chromium oxidation and found no significant correlation as the dependence on P_{O_2} was very small with a ratio of $k_p \propto \mathrm{P}_{O_2}^{\frac{1}{\mathrm{n}}}$ with n ≈ 40 [41].

Extremely low oxygen partial pressures can be obtained using different gas mixtures such (Ar)H_2-H_2O and CO-CO_2 mixtures. By controlling the ratio of the gas components, any desired oxygen partial pressure can be achieved. However, different gas mixtures having the same P_{O_2} may not result in similar oxidation kinetics as each individual gas component such as hydrogen, H_2O, N_2, or CO have their own influence on oxidation by accelerating or decelerating the oxidation reaction or by stabilizing other oxidation products such as carbides or nitrides [70,74-77]. The study of Polman et al. on the oxidation of pure chromium at 900°C in 1%CO/CO_2 (P_{O_2}= 1× 10^{-2} atm) and 1.5% H_2O/H_2 (P_{O_2}= 9.8× 10^{-21} atm) atmospheres showed a gradually higher oxidation rate than at atmospheric oxygen pressure [77]. Further studies of Hänsel and Young on the oxidation of pure chromium in multi-oxidant atmospheres at reduced oxygen partial pressures confirmed such findings [74,78].

2.6 Nitridation in oxidizing atmospheres

The majority of fundamental studies on the oxidation behavior of chromium and its alloys focuses on single-oxidant atmospheres with a wide range of oxygen pressures. Most technical atmospheres comprise multi-oxidants [45]. Besides air, as the most common example, oxidation studies were conducted in other multi-oxidant atmospheres such as CO-CO_2-N_2, O_2-N_2, N_2-O_2-H_2O, H_2-H_2O-N_2, CO-CO_2-N_2-SO_2 and effects of additional oxidants on the thermodynamic stability of oxidation products were investigated [75,78,79]. Each of these gas mixtures represents a practical atmosphere for high temperature applications such as in gas turbines, fuel cells, steam crackers etc.

During the oxidation process in multi-oxidant atmospheres, additional oxidation products such as nitrides (Cr_2N, CrN), carbides ($Cr_{23}C_6$, Cr_7C_3) and sulfides (CrS, Cr_3S_4) can form besides oxides [78,80]. The phase stability diagrams for Cr-O-N, Cr-O-S, and Cr-O-C are utilized to predict the stability of oxidation products at given technical atmospheres [75,78,81].

Although most of the studies on oxidation of chromium were focused on oxidation in oxygen atmospheres at different pressures [39,44,54,56], limited studies were conducted on oxidation of pure chromium in air at high temperatures [23,32,82]. Therefore, the major focus here is to address the thermodynamics and kinetics of the Cr-O-N system at high temperatures. For other multi-oxidant atmospheres, readers are referred to the detailed works of Zheng et al.[75,78] and Hänsel et al. [79,83-85].

2.6.1 Thermodynamics of nitridation

Nitrogen is a soluble interstitial element in chromium at high temperatures. Mills showed that the solubility of nitrogen in chromium depends on temperature [86]:

$$\log(\mathrm{wt.\%N}) = \frac{-6765}{\mathrm{T}} + 3.62 \tag{6}$$

Further addition of nitrogen can form chromium nitride (CrN) and chromium subnitride (Cr_2N) which are stable in a wide range of temperatures (see Figure 2-3) [87].

To investigate the relevance of nitrides for oxidation in air, thermodynamic phase stability diagrams are calculated for the Cr-O-N system (see Figure 2-4). It is shown that at high nitrogen partial pressures, chromium nitride (CrN) can be stable, but it requires comparatively high nitrogen pressures (see Figure 2-4). However, CrN is not stable at temperatures higher than 1049°C and nitrogen pressures of 1 atm. and below. Thus, Cr_2N is the only stable nitride compound in exposures under atmospheric pressures at temperatures above 1049°C. The phase stability diagram with inserted reaction path over the oxide scale down into the metal subscale zone is illustrated in see Figure 2-4b.

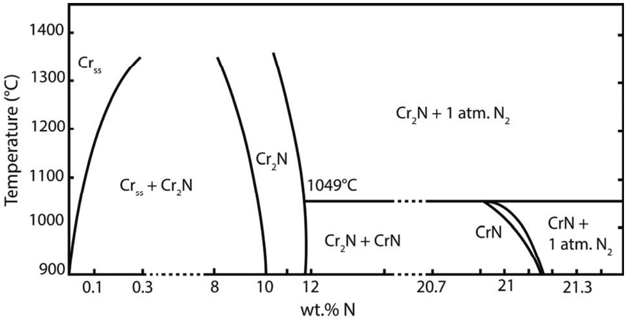

Figure 2-3. Cr-N phase diagram between 900 and 1350°C [87].

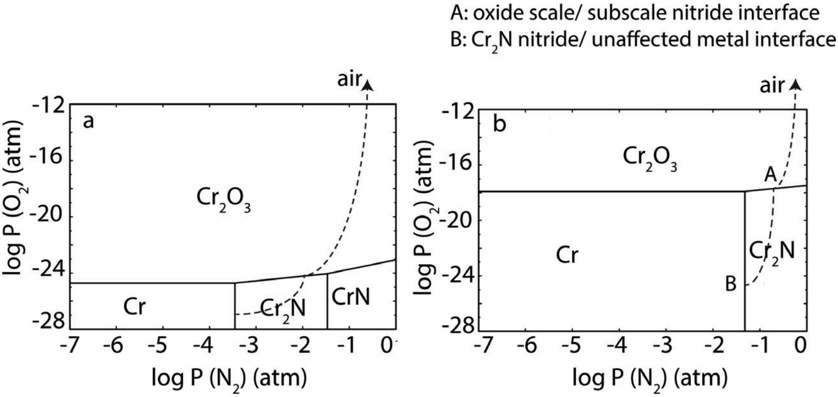

Figure 2-4. The Cr-O-N phase stability diagram at a) 900°C and b) 1200°C with inserted reaction path (FactSage).

2.6.2 Nitridation kinetics

Schwerdtfeger was the first to show that the growth of chromium subnitride (Cr_2N) is a function of inward diffusion of nitrogen in Cr_2N [88]. It was shown that the rate of chromium nitridation follows parabolic kinetics with much higher rates compared to oxidation (measured at 1100-1310°C in N_2-H_2 atmosphere) [88,89]. The intrinsic diffusivity of nitrogen in the sub-nitride Cr_2N was determined using the parabolic rate constant and Wagner's theory (D_N=4.2× 10^{-8} cm^2s^{-1} at 1200°C) [88,90,91].

When chromium is oxidized in air (N_2-O_2, P = 1 atm), chromium subnitride Cr_2N forms under the chromia scale. According to the phase stability diagram (Figure 2-4), Cr_2N is stable at low P_{O_2} and high P_{N_2}. It is known that the nitride phase significantly alters the mechanical properties of chromium via embrittlement and increasing hardness. Thus, it is of great importance to consider the formation and growth mechanism of the subnitride when studying the oxidation of chromium and its alloys at high temperatures. Despite this importance, little is known about Cr-nitridation. For instance, the effect of subnitride formation on the oxidation kinetics of chromium in e.g. air or the simultaneous transport of oxygen and nitrogen through the scale and the metal substrate are still not clear. Hagel has first separately studied the kinetics of nitridation and oxidation of chromium. He concluded that the parabolic rate constant of chromium for nitridation in nitrogen is at least one order of magnitude higher than that of oxidation in a pure oxygen atmosphere [41]. In agreement with Hagel's results, Schwerdtfeger, Seybolt, and very recently Michalik and coworkers reported significantly higher nitridation rates than oxidation rates of chromium at 950-1000°C in N_2-O_2 atmospheres, indicating that the thermally grown chromia scale is permeable for nitrogen at temperatures higher than 950°C [33,83,88].

When chromium subnitride Cr_2N forms under the oxide scale, it is logical to assume that the further oxidation process occurs via oxidation of the Cr_2N layer (Figure 2-5) and oxidation of Cr_2N occurs via the following reaction [92]:

$$\frac{2}{3}\mathrm{Cr_2N} + \mathrm{O_2} = \frac{2}{3}\,\mathrm{Cr_2O_3} + \frac{1}{3}\,\mathrm{N_2} \qquad (7)$$

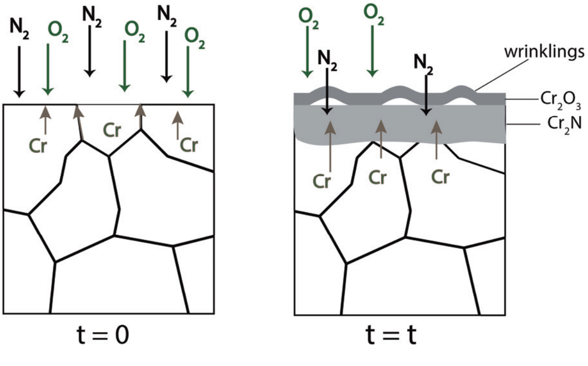

Figure 2-5. Schematic illustration of the high temperature oxidation of chromium in N_2-O_2 atmospheres.

Seybolt reported, however, that the oxidation rate of Cr_2N is equal to that of chromium metal at 1000°C [33]. Thus, the thermogravimetric data cannot resolve the formation of a subnitride layer during isothermal oxidation in air as both Cr_2N and Cr metal show similar rates of oxidation [23].

The mechanism under which the conditions for thermodynamic stability of the subnitride Cr_2N are met (i.e. very low P_{O_2} and near atmospheric P_{N_2}) is still under debate [23,33,68,81]. Some argue that this condition is solely provided by inward atomic transport of nitrogen via permeation along the chromia scale. Recently, Young et al. used atom probe tomography to show that carbon penetrates through Cr_2O_3 grain boundaries [84]. It was believed that nitrogen shows similar behavior as carbon. Nevertheless, no experimental evidence has been reported yet. Others argue that defects such as micro-cracks, micro-porosities, micro channels, or other imperfections which form during the scaling process can provide nitrogen molecular transport co-occurring with oxygen consumption via oxidation [75,84,93]. However, a clear experimental proof showing the mechanism is not known yet.

2.7 Volatilization of chromium

Formation of volatile species during oxidation makes the mechanism of oxidation and its kinetics more complex and can have an influence on the scatter of oxidation rate data.

During oxidation of chromium at high temperatures, oxidative evaporation of Cr_2O_3 as CrO_3 occurs under oxidizing atmosphere [94]:

$$\mathrm{Cr_2O_3}\ (\mathrm{s}) + \tfrac{3}{2}\ O_2(\mathrm{g}) = 2\mathrm{CrO_3}(g) \tag{8}$$

$$\Delta \mathrm{G}^{\circ} = 472{,}800 - 118.5\ \mathrm{T} \quad \mathrm{Jmol^{-1}} \tag{9}$$

This reaction is important at temperatures higher than 1000°C and at high P_{O_2} as this volatilization reaction has been found to be proportional to P_{O_2}

$$P_{CrO_3} = \mathrm{K}_{\mathrm{eq}}^{1/2} . \mathrm{P}_{\mathrm{O_2}}^{3/4} \tag{10}$$

where K_{eq} is the equilibrium constant of Eq. 8, P_{O_2} is the oxygen partial pressure, and $P_{CrO_3}$is the partial pressure of CrO_3 [35,40,41]. The Kellogg diagram is used to show the stability and partial pressure of the volatile oxide species at different temperatures and oxygen partial pressures. Figure 2-6 illustrates this diagram for volatile species of the Cr-O system ($P_{Cr_xO_y}$) versus P_{O_2} at a fixed temperature (1250K) and versus temperature at a fixed P_{O_2} (1 atm), respectively [46,95]. The vertical line in Figure 2-6a indicates the equilibrium P_{O_2} for the Cr(s)/Cr_2O_3 system. Besides CrO_3, Cr metal itself also develops high vapor pressures at high temperatures. Other volatile species of the Cr-O system are less important as their partial pressures are negligible in dry atmospheres. The horizontal line for Cr(g) in Figure 2-6a shows that the $P_{Cr(g)}$ does not depend on the oxygen partial pressures in pressure ranges less than the equilibrium P_{O_2} for the Cr/Cr_2O_3 reaction. At the Cr/Cr_2O_3 interface, $P_{Cr(g)}$ becomes comparable to P_{CrO_3} at the Cr_2O_3/O_2 interface (see Figure 2-6a). Furthermore, the vapor pressure of chromium $P_{Cr(g)}$ increases linearly with temperature and approaches the vapor pressure of P_{CrO_3} at T>1000K (see Figure 2-6b). Detailed thermodynamics of volatile species in the Cr-O system are discussed in [95,96].

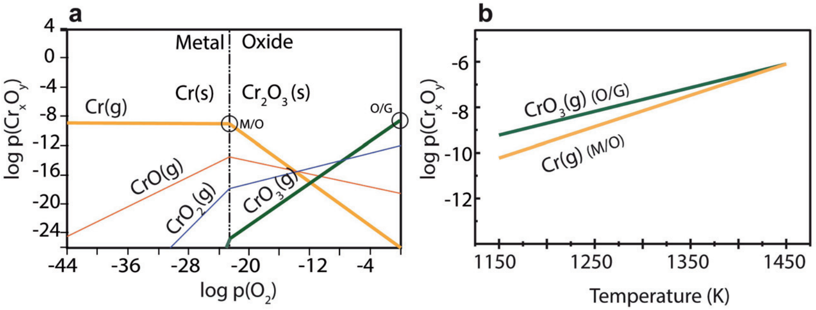

Figure 2-6. a) The partial pressure of volatile species in the Cr–O system at 977°C, b) The partial pressure of volatile species versus temperature for an oxygen partial pressure of 1 atmosphere [46].

2.7.1 Kinetics of volatilization

Volatile species have to be considered in the oxidation behavior of chromium due to their high partial pressure at high temperatures (see Figure 2-6). The most significant volatile species in the dry Cr-O system are the Cr metal at P_{O_2} below the equilibrium partial pressure for the stability of Cr_2O_3 and CrO_3 above the equilibrium P_{O_2}.

Tedmon [97] first modeled the effect of volatilization on the oxidation kinetics of chromium. He considered Wagner's theory of growth and added a negative term for scale thinning as a result of evaporation of the compact Cr_2O_3 layer. Equation 11 describes the Tedmon's model:

$$\frac{dx}{dt} = \frac{k_p}{x} - k_v \tag{11}$$

where x, is the oxide thickness, k_p is the parabolic rate constant in terms of thickness ($cm^2 s^{-1}$) and k_v is the evaporation rate constant ($cm\ s^{-1}$). Tedmon also presented the integrated form of Eq. 11 which represents the relation between time and scale thickness (x).

$$t = \frac{k_p}{k_v} - \frac{k_v}{k_p}\, x - \ln\left(1 - \frac{k_v}{k_p\, x}\right) \tag{12}$$

The physical description of Eq. 12 is that initially rapid oxide growth occurs compared to the volatilization rate. Eq. 12 illustrates how oxide growth slows down as the oxide scale thickens. This behavior is usually termed “paralinear” oxidation and is often observed for chromia-forming alloys in $O_2 + H_2O$ atmospheres or in dry oxygen above 1000°C (Figure 2-7) [36,40,98].

Thermogravimetry is widely utilized for studying oxidation kinetics of metals and alloys. In order to describe the growth kinetics with thermogravimetric data, it is required to convert Eq. 12 to mass change data using a relation between mass gain and scale thickness. Taimatsu [36] used a mathematical approach to convert the thickness-related formulation to a mass-change-related one by assuming the compact bulk density of chromia (5.21 g cm^{-3}) and the following relation to describe the paralinear kinetics.

$$(\Delta m/A) = k_p^{1/2}\, t^{1/2} - \left(2/3 + f_{Cr}/3\right) k_v t \tag{13}$$

where $\Delta m/A$ is mass change per unit area and f_{Cr} is the mass fraction of Cr in Cr_2O_3 ($f_{Cr} = 0.684$). Thus, $\left(2/3 + f_{Cr}/3\right)$ equals 0.895. The thermogravimetric results for Y-doped Cr at 1200°C were successfully fitted by the mathematical interpretation of Taimatsu [36]. Interestingly, an oversimplified combination of mass gain and volatilization terms in the form of

$$(\Delta m/A) = (k_p\ t)^{1/2} - k_v t \tag{14}$$

which was first used by Hagel [41] can also successfully describe the experimental data with similar accuracy as Taimatsu’s version, because the coefficient in Eq. 13 $\left(2/3 + f_{Cr}/3\right)$ is close to unity. Therefore, it is reasonable to fit experimental thermogravimetric results with Hagel’s equation [14,41,81,99]. It should be mentioned that k_p in Eq. 13 and Eq. 14 is not identical with k_p in the ideal parabolic rate law for oxidation which is based on pure diffusion control for oxide growth. k_p in these equations has been derived from either experimental data or a simplification that assumes direct superposition of parabolic growth and linear volatilization.

The kinetics of volatilization in chromium oxidation depends on temperature following an Arrhenius relation. Hagel is to the best of the author's knowledge the only reference who reported a temperature dependence of the volatilization of chromia during oxidation.

$$k_v = 0.214 \exp(^{-204200}/_{RT})\ (gcm^{-2}s^{-1}) \tag{15}$$

where, k_v is the volatilization rate and R is the gas constant [41].

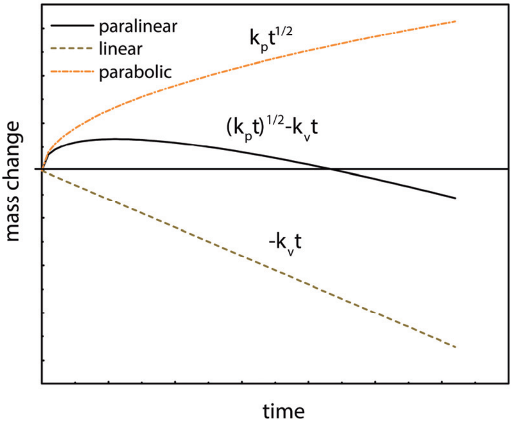

Figure 2-7. Typical mass change with time showing parabolic growth, linear volatilization, and paralinear kinetics

2.8 Trends in the development of Cr-based alloys

Unlike for other refractory alloys where research focuses mainly on one target alloy system (e.g. Nb-Nb_5Si_3 in Nb-based [100-102] or Mo-Si-B in Mo-based alloys [10,103]), to date several chromium-based alloys are under debate. The goal is to have an alloy which can withstand high temperatures with high oxidation resistance, creep resistance, and strength. Trends in the development of chromium alloys according to their mechanical characteristics were reviewed by Gu et al. [104].

The lack of low temperature ($T< 0.3\ T_m$) ductility is a significant weakness of chromium and its alloys which hinders its application for engineering applications. Many alloying strategies were undertaken to understand and improve the ductility of chromium at room temperature. Several parameters such as crystal structure, purity, grain structure, and alloying elements determine the ductility of chromium. Several theoretical and experimental studies proved the effect of interstitial impurities on the ductility of chromium at room temperature which were reviewed by Gu et al. [104].

Recently, Gao et al. screened a group of 22 elements and their influence as alloying elements on the mechanical properties of chromium at room and at high temperatures [105]. The Poisson ratio was taken as the screening parameter and the calculated tendency of the alloying effect on ductility of chromium was in agreement with existing experimental work. Nb, Mo, Ru, Rh, Ta, W, Re, Os, Ir, Pt, Pd, Hf, Ti, V, Zr, Fe, Co, Ni, Al, Si, Ga, and Ge have considerable solubility in Cr. Other elements in the periodic table have negligible solubility in Cr-based alloy on a first principle approach [105]. Their results predicted vanadium as a strong chromium ductilizer and Re and Fe as moderate ductilizers. Al, Ge, and Ga were predicted to embrittle chromium when alloyed in solid-solution [105-107].

Gu et al. experimentally studied the tensile properties of chromium alloyed with up to 3 at.% Ag. They showed that the optimum tensile properties can be obtained for Cr-2 at.% Ag which improved the yield strength and elongation by 34% and 64%, respectively [108].

Vanadium can also be beneficial for the mechanical properties of chromium [109,110]. Although vanadium is the only element in the periodic system which forms a complete solid-solution with chromium, the following considerations should be taken into account when vanadium is alloyed. Dogan et al. reported that commercial vanadium contains 0.1-0.2 wt% carbon which introduces vanadium rich precipitates of the composition $C_{20}Cr_{25}V_{55}$ at grain interiors and grain boundaries [111]. Even worse in oxidizing atmospheres, V_2O_5 can form which is not desired as it melts at 670°C [112].

The so-called Rhenium-ductilizing effect has been observed for Cr-alloys [20]. An analogous effect is observed for Ru when added up to 3 at.% as it resulted in up to 1.5% elongation at room temperature [113].

Besides alloying, removing the residual interstitial impurities such as nitrogen and oxygen was the main strategy to improve the ductility of chromium at room temperature [20]. Doping chromium with rare earth elements (such as Y, Ce, and La) which have high affinities to nitrogen and oxygen can improve the Cr-ductility via formation of stable oxides or nitrides [114]. Since both interstitial elements and the doped rare earth elements are usually concentrated at grain boundaries, fine ceramic particles will be dispersed at grain boundaries which can also enhance the high temperature strength and creep resistance of alloys. However, doping rare earth elements is technically challenging due to the segregation of these elements during quenching and possible formation of low temperature eutectics (e.g. Cr-Ce at 781°C).

Moreover, the solubility of these elements in chromium is limited as the solubility of Ce and Y is less than 1 at.% [115]. Recently, Lei et al. employed mechanical alloying at room temperature to homogeneously distribute and dope Y in Cr [116].

The application of oxide dispersions in ductilizing chromium was first suggested by Scruggs et al. in the 1960s. They reported that additions of MgO to powder metallurgical chromium can markedly improve its ductility [117]. It was proposed that MgO forms an $MgCr_2O_4$ spinel phase which getters the residual nitrogen in pure chromium. This hypothesis was recently challenged by Brady et al. who correlated the influence of the MgO dispersions with grain refinements which in turn, affects the ductility of chromium alloys [118].

Chromium alloys based on Laves phase chromides (Cr_2X, X=Nb, Ta, Hf, Zr, etc.) and silicides (A15 Cr_3X, X=Si, Pt, etc.) provide high melting points and high temperature strength and high creep resistance [119]. But the high Ductile-Brittle Transition Temperature (DBTT) of these intermetallic phases (>1000°C), deteriorates the toughness and ductility even at moderate temperatures. Thus, a toughening Cr solid-solution phase (Cr_{ss}) can be added to these phases in order to increase the ductility at lower temperatures. A subgroup of this class of materials are “in-situ composites” which has been appointed to alloys with fine microstructure composed of a solid-solution toughening phase and an intermetallic strengthening phase. The term “in-situ” is given due to the simultaneous formation (usually as a eutectic reaction) of both phases during solidification [2] and the term “composite” is given due to the co-existence of a toughening and strengthening phase.

The Cr_{ss}-Cr_3Si system forms a lamellar eutectic structure consisting of Cr_{ss} and the Cr_3Si A15 phase [8]. In this system, the A15 intermetallic phase is a source of high temperature strength, creep strength, and oxidation resistance and Cr_{ss} is the potential source of ductility. The A15 structure has a cubic microstructure composed of two sublattices for Si and Cr atoms. Studies on this alloying system are limited to the mechanical properties of single phase Cr_3Si and the Cr_{ss}-Cr_3Si system [15-17]. Mo additions are found to be beneficial for the high temperature mechanical properties of Cr-Si silicides. Since the Mo-Si system is analogous to the Cr-Si system, Mo can substitute Cr in intermetallic silicides (eg. $(Cr, Mo)_3Si$ and $(Cr, Mo)_5Si_3)$) [15,120]. Studies of Raj et al. showed that Mo can sharply increase the high temperature strength and creep resistance of chromium silicides [15,120].

2.8.1 Oxidation Resistance Considerations

Refractory metals have a considerable solubility in chromium and are known to be beneficial to the mechanical properties [20]. Experimental studies however, revealed that alloying them in solid-solution (Re, W, Mo, Nb and Ta) is rather detrimental for increasing the oxidation resistance of chromium [121,122]. In the case of Ta and W, Royer and coworkers recently reported very poor oxidation behavior of the Cr-30Mo-30W alloy at 1100°C due to the massive volatilization of MoO_3 [121]. The oxidation behavior of the binary Cr-Cr_2Nb and Cr-Cr_2Ta alloys at high temperatures also revealed poor oxidation resistance with rapid oxidation rates and extensive scale spallation [123]. In this system, the eutectic Cr-Cr_2Nb phase showed worse oxidation resistance than both single-phase Cr(Nb) solid-solution and Cr_2Nb intermetallic [12]. On the other hand, Cr-Cr_2Ta alloys showed better oxidation resistance compared to Cr-Cr_2Nb alloys at 1100°C. In contrast to the Cr-Cr_2Nb alloy, the oxidation resistance of the Cr-Cr_2Ta eutectic was better than either that of single phase Cr(Ta) or that of Cr_2Ta alloys [12]. Recently, Bhowmik and coworkers showed that additions of Si can increase the oxidation resistance of Cr-Cr_2Ta alloys at 1100°C. However, their results showed lower oxidation resistance when exposed at 1300°C [124]. Later, they showed that the co-additions of Si and Re can improve the oxidation resistance of the Cr-Cr_2Ta system [125]. The oxidation resistance of chromium alloys can be improved by up to three orders of magnitude which is promising for their potential for high temperature structural applications.

SiO_2 is more stable than chromia at ultra-high temperatures (1000-1700°C) [45,126]. Thus, addition of Si to single phase chromium can be beneficial for oxidation resistance [81,124,127]. Experimental studies showed that up to 5 at.% addition of Si is soluble in Cr without crossing the solvus line (see Figure 2-8a)[128]. The oxidation behavior of Cr-Cr_3Si alloys has only been rarely studied and little is known about the mechanism of oxidation in the binary Cr-Si alloy system. On the other hand, it is known that the oxidation behavior of single phase alloys is different from that of two-phase alloys [13,129]. Considering the promising physical properties of chromium-silicide alloys such as low density and high creep resistance [17,19,120,130-132], their oxidation behavior should also be systematically studied.

Germanium alloying in several binary and ternary silicide systems was found to be beneficial for high temperature oxidation resistance [24,25]. Binary Cr-Si [26] and Cr-Ge [27] systems are analogous in the Cr-rich parts (compare Figure 2-8a and Figure 2-8b) with both solid-solution Cr and A15 intermetallic phases (Cr_3Si and Cr_3Ge) at a nearly similar range of composition (13-22.4 at.% Si and 11.8-20.3 at.% Ge for Cr-Si). Cr_{ss} and intermetallic phase undergo a eutectic and peritectic transformation in the Cr-Si and Cr-Ge systems, respectively which makes the ternary Cr-Ge-Si system unique. Considering these facts, the influence of Ge on microstructure, crystallography, phase stability, and oxidation behavior of the two-phase Cr-Cr_3Si will be studied and discussed in this work.

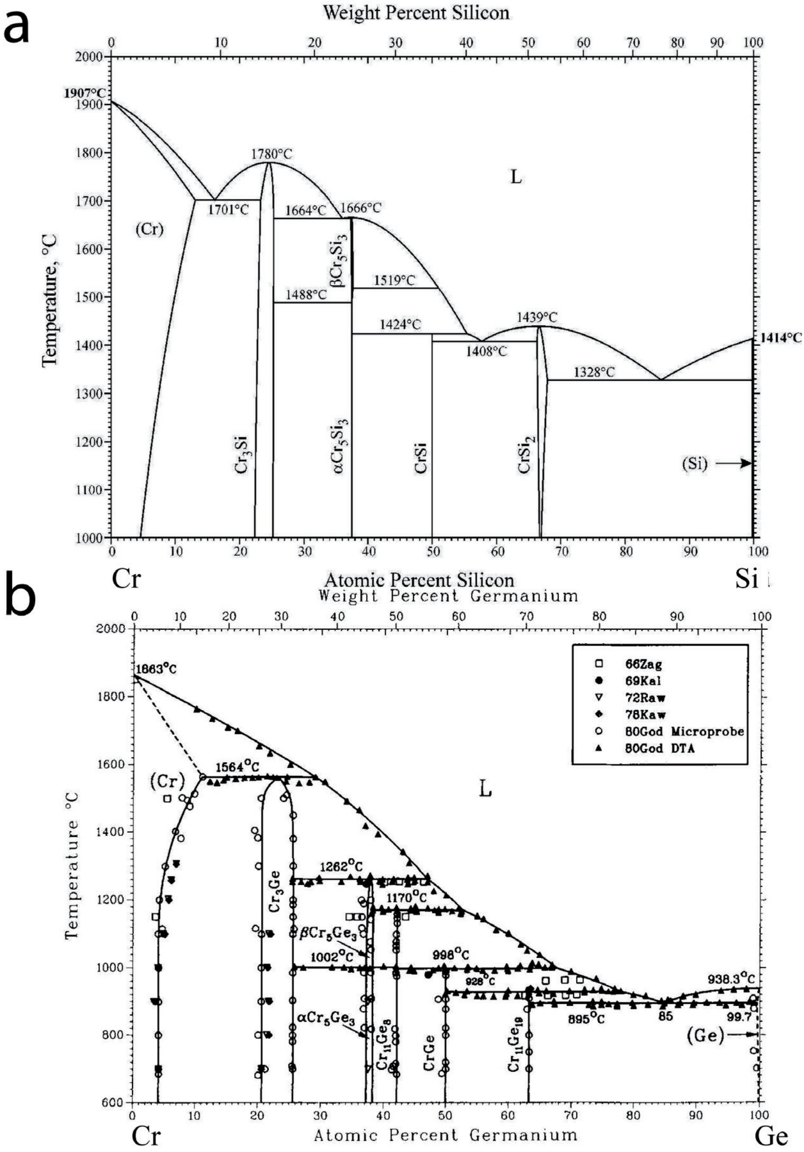

Figure 2-8. Equilibrium phase diagrams for a) Cr-Si and b) Cr-Al systems.

3 OBJECTIVES OF RESEARCH

The main objectives of this research are to elucidate the high temperature oxidation behavior of the Cr-rich (Cr > 75 at.%) Cr-Si based alloys in air. More importantly, nitridation, as a key challenge for the development of Cr-based alloys which is usually neglected during oxidation studies, will be the focus of this study. The oxidation mechanism of the two phase eutectic Cr-Cr_3Si will be investigated. Finally, the eutectic alloy will be modified with germanium to further improve the oxidation and nitridation resistance.

The following general approach is used to meet the main objectives of research:

- Oxidation of pure chromium is investigated and the effect of nitridation on oxidation behavior is determined
- The kinetics and thermodynamics of oxidation and nitridation of individual phases in the Cr-Cr_3Si system are studied.
- The key phase contributing to both oxidation and nitridation resistance of the eutectic Cr-Cr_3Si alloy is identified
- Further improvements will be done by addition of a ternary alloying element (in this case Ge) to enhance the resistance of the target alloy in air at high temperatures.
- The role of Ge in the microstructural evolution and physical metallurgy of the Cr-Cr_3Si system is also explored

.

4 EXPERIMENTAL PROCEDURE

4.1 Materials

Drop cast ingots with an approximate total weight of 7g and nominal compositions listed in Table 4-1 and Table 4-2 were prepared using the arc melting method. Chromium (99.995 wt %, Alfa Aesar), silicon (99.9999 wt %, Alfa Aesar) and germanium (99.999 wt %, Alfa Aesar) pieces were melted on a water cooled copper mold under high purity Ar atmosphere using a compact arc melter (MAM-1, Edmund Bühler, Germany). To capture the residual oxygen, a Zr getter was melted before melting the starting materials. Ingots were turned over at least six times and re-melted to avoid inhomogeneity. Coupons with square geometries (4×4×2 mm) were cut from the center of each ingot, using electric discharge machining (EDM). All surfaces of alloy coupons were ground with 500 grit SiC papers to ensure similar surface conditions. Figure 4-1 shows the casting set up and the arc melting process used to fabricate the alloys.

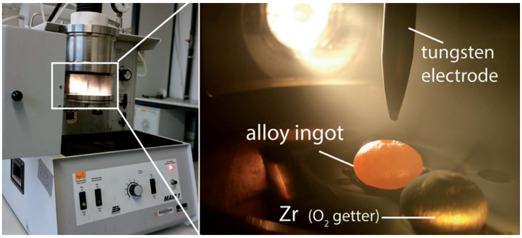

Figure 4-1. The arc melting apparatus used for casting of model alloys.

4.2 Cr-Si alloys

Four binary Cr-Si alloys were selected from the chromium rich part of the Cr-Si phase diagram (Cr > 75 at.%). Pure chromium is used as a reference to compare the oxidation behavior of the alloys. The nominal compositions of the studied binary alloys are listed in Table 4-1.

Table 4-1. Nominal compositions of Cr-Si binary alloys

Alloy designation	*Pure Cr*	*S3*	*S16*	*S19*	*S25*
Cr (at.%)	100	97	84	81	75
Si (at.%)	0	3	16	19	25

4.3 Cr-Ge-Si alloys

A single phase and 10 two-phase ternary alloys with nominal compositions listed in Table 4-2 were fabricated. Constant Cr content and various Si and Ge contents were selected for the two-phase alloys to track the composition and microstructural change upon substitution of Si with Ge.

Table 4-2. Nominal compositions of studied Cr-Ge-Si alloys.

Alloy composition (at.%)	*S2G1*	*SG1*	*SG2*	*SG4*	*SG6*	*SG8*
Cr	97	84	84	84	84	84
Si	2	15	14	12	10	8
Ge	1	1	2	4	6	8
Alloy composition (at.%)	*SG10*	*SG12*	*SG14*	*G16*	*S18G1*	
Cr	84	84	84	84	81	
Si	6	4	2	0	18	
Ge	10	12	14	16	1	

4.4 Solution heat treatment

The equilibrium phase diagram of the ternary Cr-Ge-Si system was assessed using heat treated alloys. As-cast specimens were annealed at 1350°C for 100 hours in a tube furnace (Carbolite, Germany) under Ar-5 vol.%H_2 flow and using titanium chips as an oxygen getter. After heat treatment the alloys were cooled down to room temperature in the furnace.

4.5 Continuous thermogravimetry

Thermogravimetric measurements at 1350°C were conducted using a microbalance (Sartorius Micro M25-D-V, Germany) which was equipped with a vertical tube furnace. The alloy coupon was attached to the balance with an alumina rod attached with platinum wire endings and held inside the hot zone of the furnace. The length of Pt-wire was kept limited to the ending parts due to Pt-volatilization at high temperatures. The balance was stabilized at room temperature after synthetic air was introduced to the furnace chamber at a linear flow rate of 203.7 cmh^{-1}. A heating rate of 20 $Kmin^{-1}$ was applied up to the test temperature of 1350°C. Isothermal exposure was conducted for up to 100h and finally the sample was cooled down to room temperature in the furnace. A reference measurement was performed with the same test parameters in order to exclude instrumental artifacts including the thermal drift and Pt-wire volatilization (if any). The reference profile was subtracted from the specimen's mass gain profile.

TG-measurements at 950°C, 1050°C and 1200°C were conducted by a Netzsch STA 449-F3 (Netzsch GmbH, Germany) with a balance resolution of 0.1 μg. The schematic view of the setup is illustrated in Figure 4-2. Oxidation kinetics and nitridation kinetics of the alloys were investigated by exposure in synthetic air (N_2-21%O_2, Air Liquide) and forming gas (N_2-5%H_2, Air Liquide), respectively. For exposures in N_2-5%H_2, the chamber was evacuated twice prior to the measurements to ensure the removal of O_2 traces. A heating rate of 10 K/min and a linear flow rate of 217 cmh^{-1} were applied for all measurements. Isothermal exposures were conducted for up to 50 hours. The TG-measurement was repeated for random specimens to verify the reproducibility of the test.

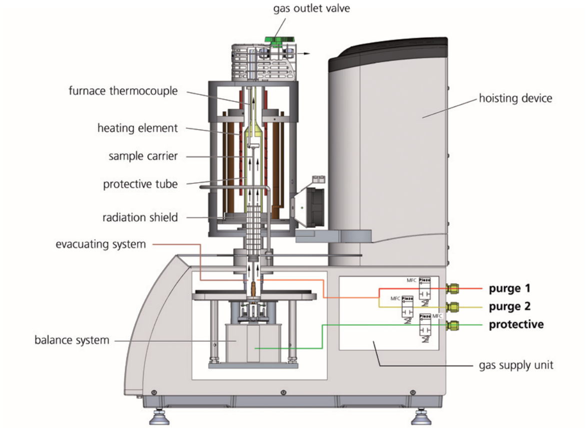

Figure 4-2. Schematic view of the thermogravimetric apparatus (with kind permission from Netzsch Gerätebau GmbH).

Specimens used for oxidation experiments were ground (600 grit SiC paper), weighed, and degreased in acetone in an ultrasonic cleaner before being introduced to the furnace chamber.

4.6 Discontinuous thermogravimetry

Long-term discontinuous thermogravimetric tests were conducted at 1200°C in a tube furnace in synthetic air atmosphere with a 203 cmh^{-1} linear flow rate. The samples were placed separately in alumina crucibles and inserted/removed from the furnace after time intervals of 50, 200, 500, and 1000 hours of cumulative exposure. After each removal, samples were weighed and re-inserted into the furnace.

4.7 Acoustic emission analysis during isothermal oxidation

Acoustic Emission (AE) is based on high frequency elastic waves which are generated as a result of stress induced structural changes in materials. The frequencies of these waves are much higher than those of the environment noise and therefore, clearly detectable. In this work, AE was used to characterize the formation of scale defects during isothermal oxidation of chromium. Two wave guide wires were spot welded on the two sides of a pure Cr specimen. The other side of each wire was soldered to cone sensors which were connected to an amplifier and a computer which recorded the AE signals (Figure 4-3). The specimen was inserted in a cylindrical furnace operated at 1050°C. The exposure was isothermally continued for 100h in air while defect formation in the oxide was monitored using the AE system.

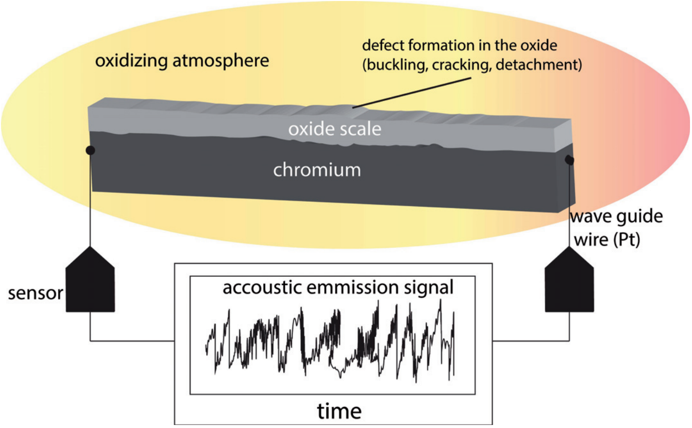

Figure 4-3. The schematic illustration of the acoustic emission apparatus utilized during isothermal oxidation of chromium.

4.8 Metallography

Alloy cross-sections were prepared by mounting specimens in hot epoxy resins, grinding through 1200 grit SiC paper, and polishing with diamond (3 and 1 µm) and colloidal silica (0.02 µm) pastes.

The oxidized specimens were sputtered with gold and coated with electroplated nickel before being mounted in epoxy resins. The electroplated nickel layer protects the oxidation products during metallographic preparation and avoids the loss of contrast at the specimen-epoxy interface during microscopic investigations [81].

Macroscopic images of specimens after experiments were documented using a Leica stereo microscope. Optical microscopy at higher magnifications (up to 1000-times) was conducted using a Leica DMLA microscope.

A Philips XL40 electron microscope equipped with an energy dispersive x-ray spectrometer (EDS) was used for detailed microscopic analysis of alloy microstructure, morphology, and chemical composition of the oxide scales. Backscattered electron (BSE) and secondary electron (SE) modes were used, respectively, to investigate the alloy microstructure and the topology of the oxides. EDS was mainly used for analyzing chemical composition of the oxide scales and remnants.

The actual composition of the studied alloys as well as semi-quantitative line scans and element distribution maps of the oxidized alloys were characterized by wavelength dispersive spectrometry (WDS) using a JEOL JXA-8100 electron probe micro analyzer (EPMA). Multipoint grids (10×10) of spot measurements were performed at three different zones to obtain the actual composition of alloy. Post-oxidized cross-sections were investigated with both element distribution maps and quantitative line scans using 15kV and one micrometer step size. Pure Cr, Si, and Ge were used as standards to characterize alloy composition. Oxidized alloys were quantitatively characterized using Fe_4N and Al_2O_3 standards for nitrogen and oxygen, respectively.

4.9 X-ray diffraction

X-ray diffraction was used to investigate the crystal structure of the alloys and the oxide scales. Alloys structures were characterized by a Bruker D8 advanced diffractometer with Cu-K_α radiation. The Nelson-Riley extrapolation method was used for precise determination of the lattice constants [133].

After oxidation, the oxide scales were crushed into powder and studied by x-ray powder diffraction using a STOE Stadi P diffractometer in transmission geometry. The diffractometer was equipped with a molybdenum x-ray tube (Mo-$K\alpha 1 = 0.71073$ Å), and a curved Ge-(111)-monochromator. Patterns were collected in an angular range of 5–50° (2θ). Phase identification was performed by comparing the patterns to the PDF database.

As will be shown later, single crystals of chromia form on the thermally grown scales formed on Cr-Si and Cr-Si-Ge alloys. The single crystalline structural investigation was conducted on a single crystal using the STOE Stadi P diffractometer in a range of 5-25° (2θ). Rietveld refinement was performed using the full-matrix least-squares method.

4.10 Thermodynamic calculations

Thermodynamic calculation was used to predict the stability diagrams and activity of elements in the alloy systems at the testing temperatures. FactSage 6.5 was used to calculate stability diagrams for Cr-O-N system. Activity profiles for the Cr-Si and the Cr-Ge-Si systems were calculated by the ThermoCalc program using the TCAL4 database and the recently obtained CALPHAD dataset for the Cr-Ge-Si system [134].

5 RESULTS

5.1 Kinetics of oxidation and nitridation of pure chromium

Oxidation and nitridation kinetics of pure chromium were investigated using thermogravimetry. The influence of single oxidants (i.e. nitrogen, and oxygen) on the overall oxidation kinetics of chromium in synthetic air was studied by isothermal exposure conducted in Ar-20%O_2, N_2-5%H_2, and synthetic air (N_2-21%O_2).

Figure 5-1 shows the isothermal oxidation kinetics of pure chromium at 950, 1050, and 1200°C in all studied atmospheres. It is obvious that specimens exposed at higher temperatures show higher mass gains. For instance, the final mass gain of pure Cr after 50h oxidation in synthetic air is 4.49, 9.37, and 21.70 mg/cm^2 at 950°C, 1050°C, and 1200°C, respectively. The mass gain curves are fitted using Eq. 14 (the continuous lines in Figure 5-1) using Origin 2015 (OriginLab Corporation, Northampton, USA) to quantify the oxidation kinetics. In order to differentiate the effect of each oxidant, the parabolic constants obtained for chromium exposed in synthetic air, nitrogen and oxygen are termed as k_p , k_p^{nit}, and k_p^{ox}, respectively. It should be noted that the k_p values are derived from experimental data and do not directly correspond to the ideal k_p of the diffusion controlled oxidation. The term k_v is assigned to the linear volatilization rate of chromium oxide when Cr was exposed to either oxygen or synthetic air atmosphere. The determined kinetics parameters are listed in Table 5-1.

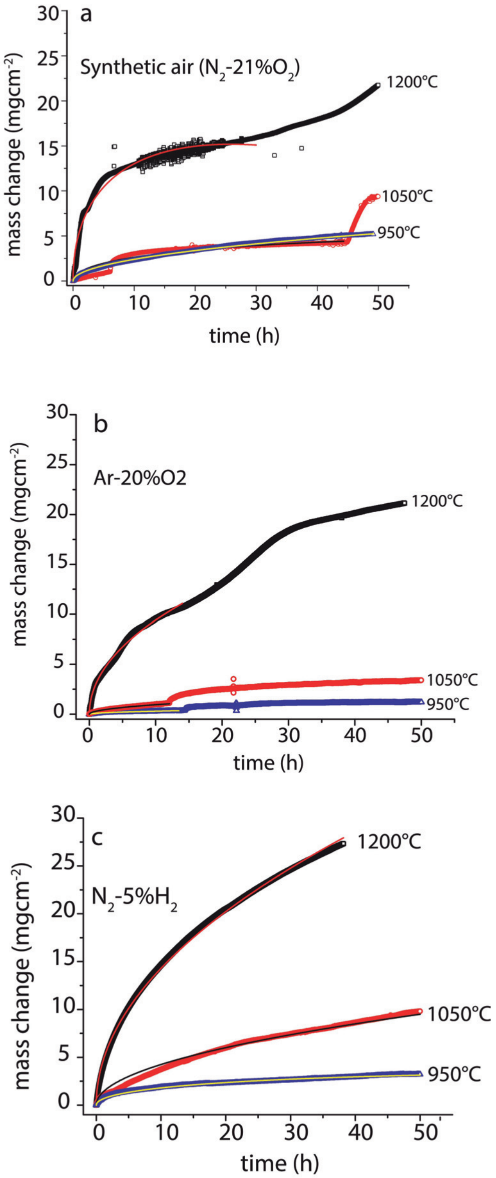

Figure 5-1. The influence of temperature on high temperature oxidation-nitridation kinetics of pure chromium in a) synthetic air, b) Ar-20%O_2, and c) N_2-5%H_2.

Table 5-1. Determined kinetic parameters for pure chromium exposed to single and multi-oxidant atmospheres at various temperatures.

Atmosphere	*Parameter*	*Temperature*		
		1200°C	1050°C	950°C
Synthetic air (N_2-21%O_2)	k_p ($g^2cm^{-4}s^{-1}$)	8.8 ×10^{-9}	2.7 ×10^{-10}	1.6 ×10^{-10}
	k_v ($gcm^{-2}s^{-1}$)	1.4 ×10^{-7}	1.3 ×10^{-8}	9.7 ×10^{-10}
Nitrogen (N_2-5%H_2)	k_p^{nit} ($g^2cm^{-4}s^{-1}$)	5.7 ×10^{-9}	5.0 ×10^{-10}	1.3 ×10^{-10}
Oxygen (Ar-20%O_2)	k_p^{ox} ($g^2cm^{-4}s^{-1}$)	2.7×10^{-9}	2.5×10^{-11}	3.4×10^{-12}
	k_v ($gcm^{-2}s^{-1}$)	1.0×10^{-8}	1.7×10^{-10}	1.3×10^{-9}

Figure 5-2 illustrates the temperature dependence of k_p , k_p^{nit}, and k_p^{ox} for the temperature range of 950-1200°C. A distinguished difference is observed between the values of the parabolic rate constant in synthetic air (k_p) and Ar-20%O_2 atmosphere (k_p^{ox}). This difference is smaller at higher temperatures. On the other hand, the mathematical sum of k_p^{nit}, and k_p^{ox} at each temperature is shown in Figure 5-2 which shows approximately an overlap with the k_p curve obtained from experiments in synthetic air, according to Eq. 16.

$$k_p \approx k_p^{nit} + k_p^{ox} \tag{16}$$

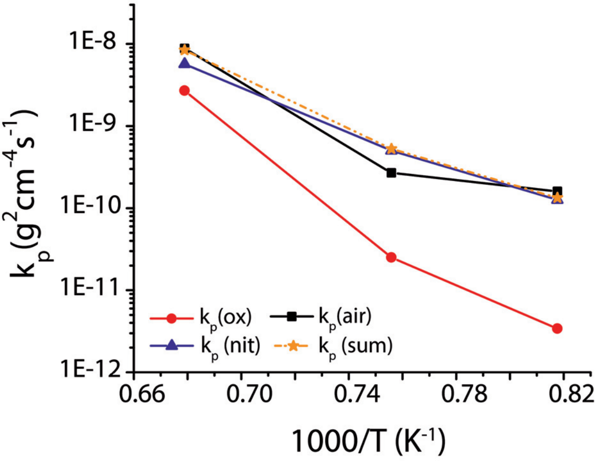

Figure 5-2. Temperature dependency of the parabolic rate constant for oxidation and nitridation of pure chromium in synthetic air, N2-5%H2, and Ar-20%O2.

It is noteworthy that abrupt discontinuities are observed in the mass change curves measured in Ar-20%O_2 and synthetic air (see Figure 5-1). The large discontinuities were not taken into account for the fitting range to ensure higher accuracy and avoid scattered data.

The nature of large discontinuities was revealed by post exposure cross section microscopy of oxidized specimens after thermogravimetry. These discontinuities are typical features observed for oxidation of pure chromium [44,56]. Figure 5-3a shows that the scale formed on pure Cr is composed of multilayers showing different morphologies: a thick, dense outer layer on top which shows significant wrinkling and a second layer underneath which shows fine columnar chromia grains towards the inner side of the outer layer (see the inset in Figure 5-3a). This implies that detachment is occurred at high temperature as significant oxide growth after detachment is evident. To investigate oxide scale detachment during isothermal exposure, an acoustic emission test was performed during isothermal oxidation of pure chromium at 1050°C (Figure 5-3b). During isothermal oxidation at this temperature two major acoustic emissions were heard after approximately 6h and 37h which are closely coincident with discontinuities in the corresponding TG-curve (see Figure 5-1a). The strongest emission is observed during cooling at the end of the 100h exposure (Figure 5-3b).

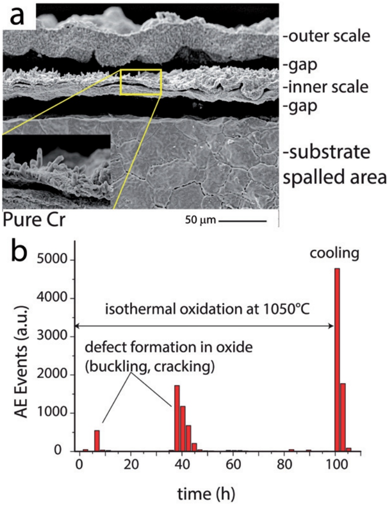

Figure 5-3. a) Cross section of chromia scale after 50h isothermal exposure at 1050°C in synthetic air, b) the acoustic emission profile during 100h isothermal exposure at 1050°C.

5.2 As-cast microstructure of Cr-Si alloys

The actual composition of binary Cr-Si alloys listed in Table 5-2 indicates that alloys with the intended nominal compositions could successfully be fabricated by drop casting without significant deviation from the nominal composition (compare with Table 4-1).

Table 5-2. Actual compositions of binary Cr-Si alloys.

Alloy designation	*S3*	*S16*	*S19*	*S25*
Cr (at.%)	97.0 ± 0.2	84.2± 0.3	82.1± 0.7	74.4 ± 0.2
Si (at.%)	3.0 ± 0.2	15.8 ± 0.3	17.9 ± 0.7	25.6 ± 0.2

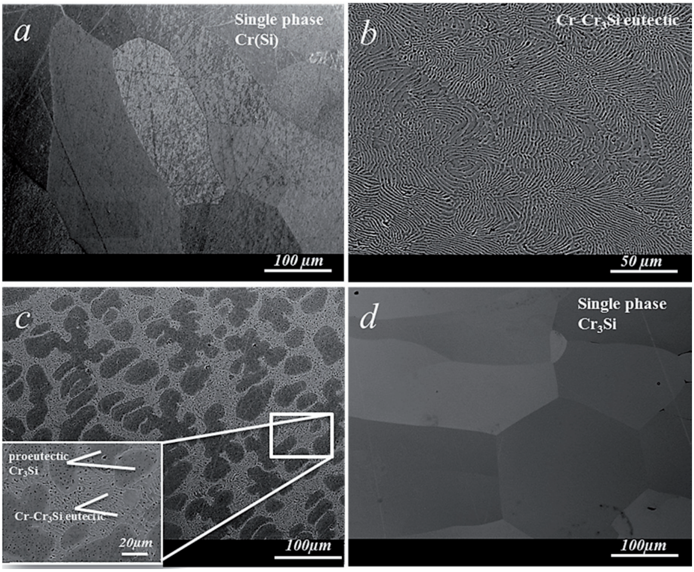

Figure 5-4. Microstructural evolution of chromium alloys with addition of Si. a) single phase solid-solution S3 (SE mode), b) eutectic Cr-Cr_3Si alloy S16, c) hyper-eutectic alloy S19, d) single phase silicide alloy S25 [81] (with kind permission from Springer Science and Business Media).

According to the Cr-Si equilibrium phase diagram (Figure 2-8a) Si has up to ~13 at.% solubility in chromium. The solubility limit decreases with decreasing temperature to ~4 at.% at 1000°C [26]. As a representative alloy for the Cr(Si) solid-solution phase, 3 at.% Si was chosen (alloy S3). The microstructural appearance of the as-cast alloys is illustrated in Figure 5-4a-d. Increasing the Si content to 15.8 at.% leads to a eutectic lamellar microstructure composed of Cr(Si) and Cr_3Si lamellae (Figure 5-4b). No primary Cr(Si) or Cr_3Si was observed in the microstructure of this alloy, confirming solely eutectic solidification of alloy S16. However, it is noteworthy that although the Cr-Si phase diagram has been well studied, diverse eutectic points between 15-16 at.% Si have been reported for the Cr-Cr_3Si system [26,128,135,136].

Alloy S19 showed a hyper-eutectic microstructure with Cr_3Si as the primary phase surrounded by an interconnected network of Cr-Cr_3Si lamellae (Figure 5-4c). Increasing the Si content to 25.6 at.% resulted in single phase Cr_3Si (Figure 5-4d) which is in accordance with other descriptions of the Cr-Si system [26,128].

5.3 Microstructure of Cr-Ge-Si alloys

Ternary Cr-Ge-Si alloys were developed based on the mutual substitution of Si and Ge at constant Cr contents. The actual compositions of ternary alloys listed in Table 5-3 are in good agreement with the nominal compositions chosen for these alloys. The evolution of the microstructure upon increasing the Ge/Si ratio is shown in Figure 5-5. By substitution of 2 at.% Si with Ge, the lamellar Cr-Si eutectic microstructure (Figure 5-5a) is slightly distorted (Figure 5-5b) but remained fine. Further increase of the Ge/Si ratio altered the microstructure more significantly, as alloy SG4 features a coarser microstructure composed of a continuous network of A15 phase surrounding the irregularly shaped Cr_{ss} primary phase (Figure 5-5c). It is noteworthy that as Ge is added to the alloys, the gray scales representing the Cr_{ss} phase in BSE images switch from darker levels (in comparison with the A15 phase) to brighter levels due to the higher atomic weight of germanium compared to that of chromium and silicium. Alloy SG8 shows a similar microstructure as alloy SG4 (Figure 5-5d). Alloys with Ge/Si ratios > 50% show microstructures with Cr_{ss} primary dendrites embedded in an A15 matrix (Figure 5-5e-f). Figure 5-5f illustrates the binary Cr-Ge peritectic microstructure consisting of Cr_{ss} dendrites embedded in the A15 matrix.

Table 5-3. Actual compositions of ternary Cr-Ge-Si alloys measured by EPMA.

Alloy composition (at.%)	*SG1*	*SG2*	*SG4*	*SG6*	*SG8*
Cr	83.8 ± 0.4	83.1 ± 0.1	83.6 ± 0.1	84.2 ± 0.6	84.5 ± 0.5
Si	15.3 ± 0.4	14.6 ± 0.1	11.9 ± 0.2	9.9 ± 0.4	7.8 ± 0.2
Ge	1.0 ± 0.0	2.4 ± 0.1	4.5 ± 0.0	5.9 ± 0.2	7.6 ± 0.3
Alloy composition (at.%)	SG10	SG12	SG14	G16	S18G1
Cr	84.7 ± 0.1	84.2 ± 0.5	83.7 ± 0.3	84.7± 1.1	81.1 ± 0.4
Si	5.3 ± 0.2	3.7 ± 0.2	1.95 ± 0.1	0	17.8 ± 0.4
Ge	10.0 ± 0.3	12.2 ± 0.4	14.3± 0.2	15.3 ± 1.1	1.1 ± 0.0

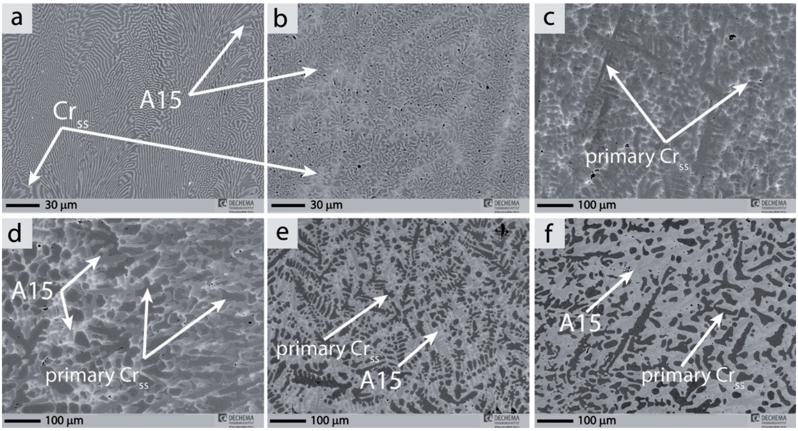

Figure 5-5. Evolution of the as-cast microstructure of Cr-Ge-Si alloys upon mutual Si-Ge substitution. Alloy (a) S16, (b) SG2, (c) SG4, (d) SG8, (e) SG12, and (f) G16.

5.3.1 Post-annealed microstructures

The microstructures illustrated in Figure 5-5 showed that when Ge is added, micro-segregation of Ge (brighter grey scales) to the A15-Cr_{ss} phase boundaries occurs during solidification. It should be noted that increasing the Ge/Si ratio leads to increased micro-segregations at these regions. After annealing for 100h at 1350°C, an equilibrium microstructure is obtained as solidification induced features are eliminated (Figure 5-6). Several microstructural features can be noted after annealing; a) microstructural coarsening, b) precipitation of intermetallic phases in the chromium solid-solution phase, and c) homogeneous distribution of Ge at the phase boundaries.

The distribution of Si and Ge in the Cr_{ss} and A15 phases was obtained by EPMA element distribution maps (see Figure 5-7). As Figure 5-7 shows, although the microstructures are more homogeneous, still some levels of coring can be observed for high Ge/Si ratios. Germanium is homogeneously distributed in the Cr_{ss} phase of the alloys SG2, SG4, and SG8, SG12, while segregation of Ge and Si occurred within the A15 phase. Si is concentrated inside the A15 phase and shows lower signals at the phase boundaries (Figure 5-7).

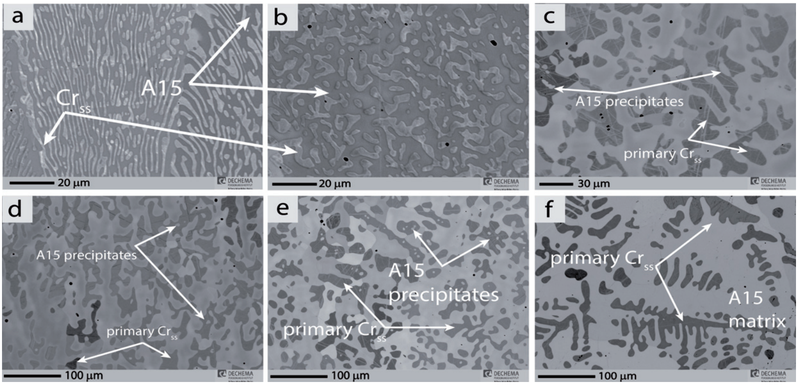

Figure 5-6. Evolution of the as-cast microstructure of Cr-Ge-Si ternary alloys after 100h annealing at 1350°C.

Precipitation of the A15 silicide phase inside the coarse solid-solution dendrites is evident in Figure 5-6 and Figure 5-7. The amount of precipitation increases as the Ge/Si ratio increases (see Figure 5-7). Image analysis of the annealed alloys in Figure 5-7 indicates that the A15 phase volume fraction increases with increasing Ge/Si ratio (Figure 5-8).

5.3.2 Partitioning of Si and Ge in Cr_{ss} and A15 phases

The quantitative partitioning of Si and Ge in both Cr_{ss} and A15 phase is shown in Figure 5-9. Partitioning of Ge and Si in both phases shows an inverse linear relation to the Ge/Si ratio in the alloys (Figure 5-9a,c). It is clearly shown that Si and Ge can substitute each other within the solubility limits of both Cr_{ss} and A15 phase (Figure 5-9c). The linear increase in the Ge content of the A15 phase co-occurs with the linear decrease of Si as the Ge/Si ratio increases. Figure 5-9b and Figure 5-9d shows the solid solubility limit of Cr_{ss} and the A15 phase in the ternary system indicating that while the solubility limit of Cr increases with increasing Ge/Si ratio, it decreases in the A15 phase.

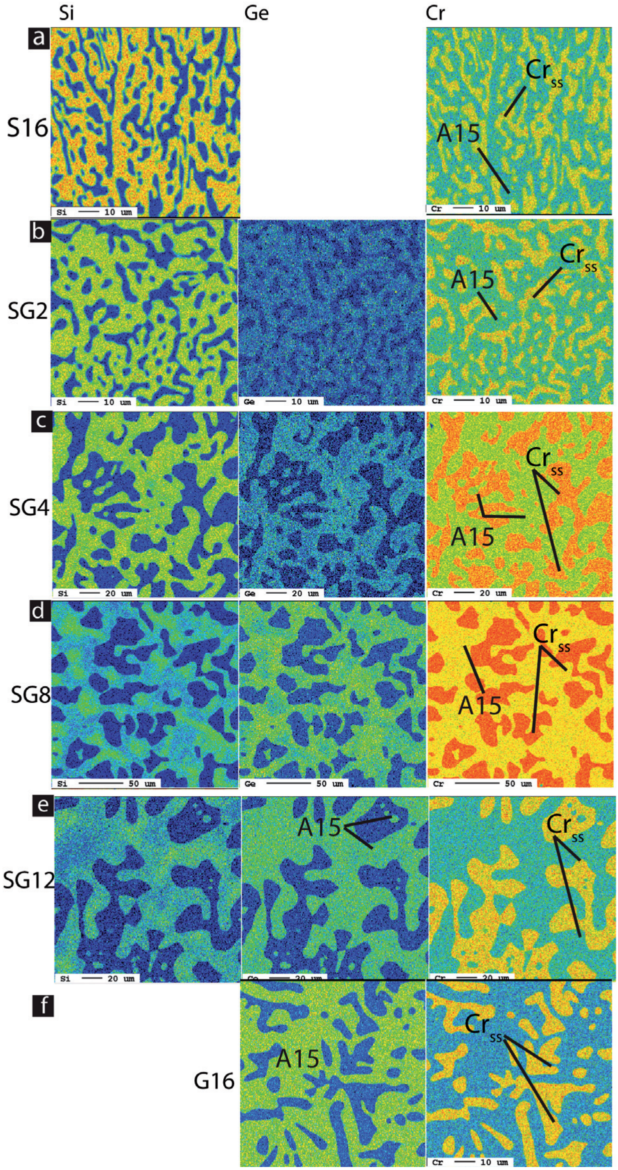

Figure 5-7. Distribution of Cr, Si, and Ge in annealed Cr-Cr_3Si and Cr-Cr_3(Si,Ge) ternary alloys illustrating the partitioning of Si and Ge in the constituent phases. Note the A15 precipitates in the Cr_{ss} phase as the Ge/Si ratio increases.

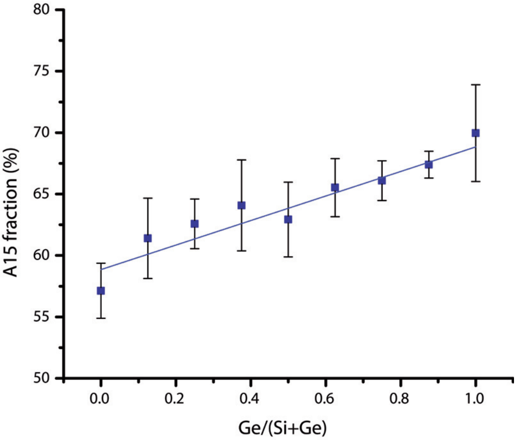

Figure 5-8. Correlation between A15 phase fraction and Ge/Si substitution ratio in the two-phase Cr-A15 alloys.

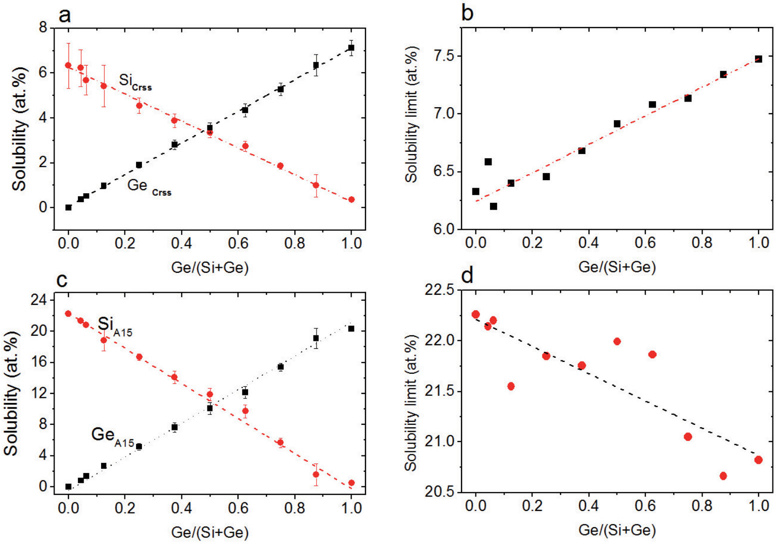

Figure 5-9. Partitioning of Si and Ge content in (a,b) Cr_{ss} and (c,d) A15 phase in alloys as a function of Ge/(Ge+Si) ratio.

5.3.3 X-ray diffraction analysis on Cr-Ge-Si alloys

X-ray diffraction patterns of the two phase alloys S16, G16, and SG1-SG14 show that all alloys are composed of two phases consisting of a chromium solid-solution and the intermetallic A15 phase. The reflection positions of both phases are slightly shifted. These reflection shifts were taken to determine the lattice constants of each phase.

The substitution of Si with Ge in both solid-solution phase and A15 intermetallic linearly increases the lattice constants in these phases (see Figure 5-11). The slope of the linear fit indicates that the lattice constant of the A15 phase shows a much higher dependency on the Ge/Si ratio than that of Cr solid-solution.

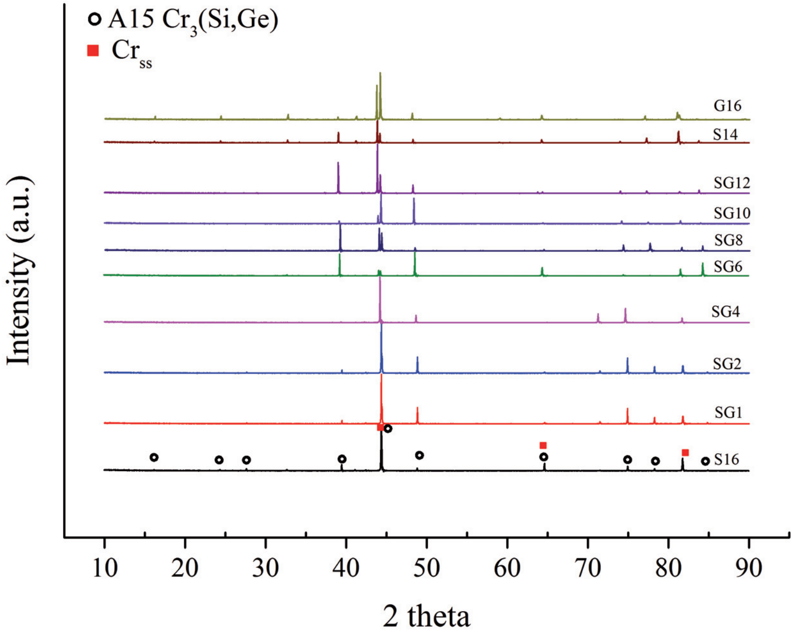

Figure 5-10. X-ray diffraction patterns of the studied binary (Cr-Si) and ternary (Cr-Ge-Si) alloys.

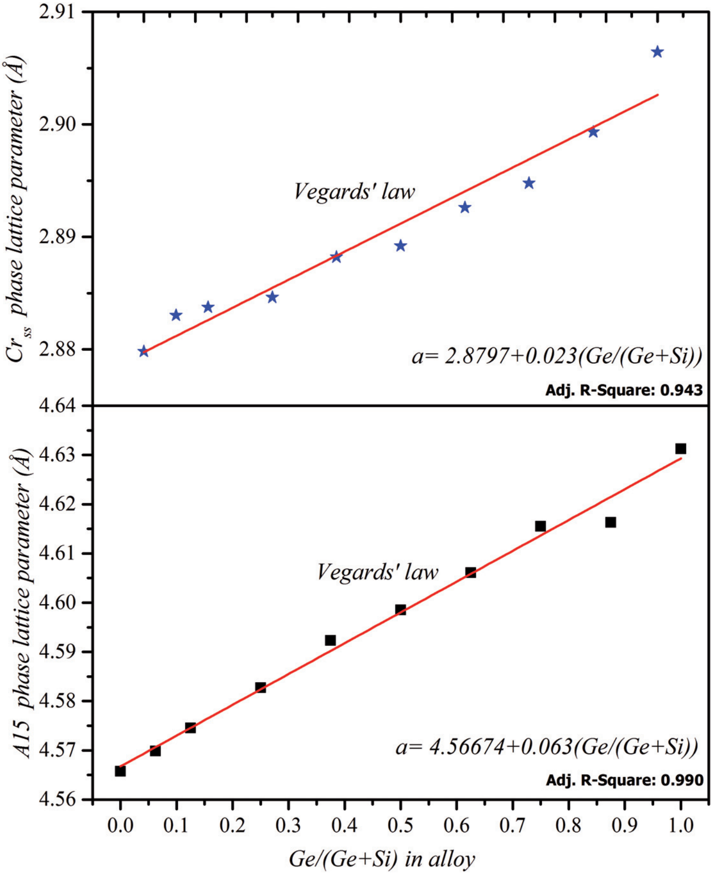

Figure 5-11. Effect of Ge/Si ratio on the lattice constants of bcc-Cr$_{ss}$ and the A15-silicide.

5.3.4 Assessment of the ternary Cr-Ge-Si diagram in the Cr-rich section

Based on the EPMA and XRD measurements, the semi-isothermal section (at 1350°C) of the chromium rich corner of the ternary Cr-Ge-Si phase diagram was assessed (Figure 5-12). The corresponding binary diagrams Cr-Si and Cr-Ge are used as a guide for the accuracy of the assessed diagram. The phase boundaries in binary diagrams agree well with those of the ternary system.

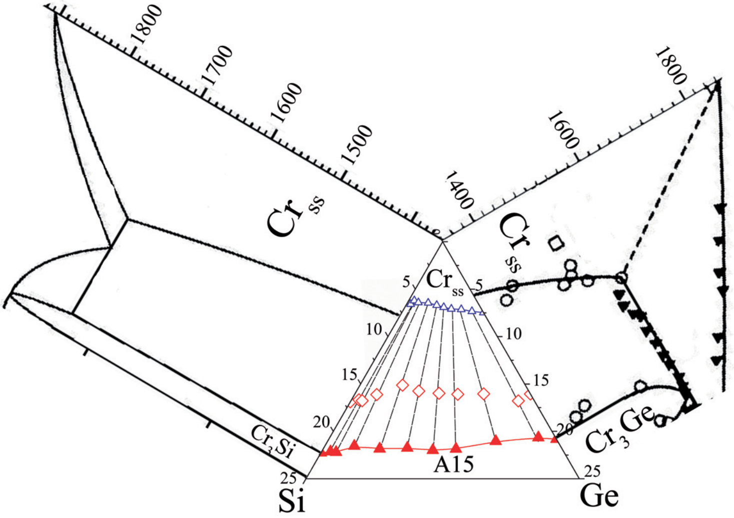

Figure 5-12. Semi-isothermal section of the Cr-Ge-Si ternary system in the high-chromium corner at 1350°C. Cr-Si and Cr-Ge binary diagrams are shown at corresponding edges on ternary diagram [26,137].

5.4 Oxidation behavior of the Cr-Si system in air

Thermogravimetric data at 1200°C in synthetic air for different Cr-Si alloys are shown in Figure 5-13. Addition of 3 at.% Si to Cr significantly improves the oxidation resistance under isothermal conditions. Further additions of Si lead to a continuous decrease in oxidation rate of the alloys. Single phase A15 intermetallic (S25) showed the slowest oxidation kinetics and two-phase Cr-Cr_3Si alloys (S16, S19) show oxidation kinetics between single phase solid-solution and single phase intermetallic alloys.

For quantitative analysis of the oxidation behavior, thermogravimetric data were fitted using Eq. 14 (solid lines in Figure 5-4b). The calculated parabolic rate constants (k_p) and the mass loss rates (k_v) as well as the fit confidence values are summarized in Table 5-4. The reduced Chi-squared and adjusted R-squared values indicate the validity of the fit. Results show that not only the parabolic rate, but interestingly also the volatilization rate are lowered when Si is added. By addition of 3 at.% Si, the oxidation rate (k_p) and volatilization rate (k_v) of pure Cr are reduced by approximate factors of 20 and 25, respectively. The increase of the Si content beyond 3 at.% Si up to 25% further reduces the (k_p), and (k_v) oxidation as shown in Figure 5-13b.

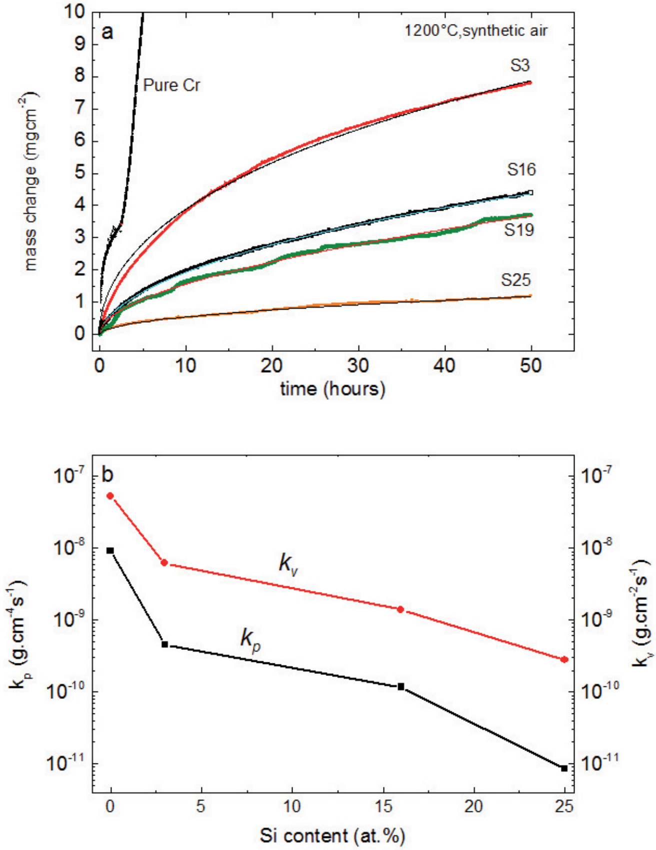

Figure 5-13. a) Thermogravimetric curves (experimental and calculated fit) for Cr-XSi binary alloys (X=0, 3, 16, 19, 25) at 1200°C in synthetic air. b) Effect of Si on parabolic constant (k_p) and mass loss rate (k_v).

Table 5-4. Quantitative values of k_p and k_v for Cr-Si alloys

Alloy	*Si Content (at.%)*	k_p *($g^2cm^{-4}s^{-1}$)*	k_v *($gcm^{-2}s^{-1}$)*	*Reduced (Chi)²*	*Adj. R²*
S3	3	4.5×10^{-10}	6.2×10^{-9}	0.02425	0.99331
S16	16	1.2×10^{-10}	1.4×10^{-9}	5.07E-4	0.99955
S19	19	7.4×10^{-11}	2.7×10^{-10}	0.00703	0.99135
S25	25	8.6×10^{12}	2.8×10^{-11}	6.25×10^{-4}	0.99198

5.5 Nitridation of the Cr-Cr_3Si eutectic alloy in nitrogen

Thermogravimetric analysis was conducted on the Cr-Cr_3Si eutectic alloy (S16) in N_2-5%H_2 atmosphere at 1200°C (see Figure 5-14). It is evident that the rate of nitridation in N_2-H_2 atmosphere is higher than that of oxidation in synthetic air (N_2-O_2). Fitting the TG-curve corresponding to exposure in N_2-H_2 reveals that the kinetics of the Cr-Cr_3Si alloy deviate from the parabolic rate, but can be described by the following general power law [138]

$$\frac{\Delta m}{A} = k\, t^n \tag{17}$$

where k and n are constant and equal to 0.28 and 0.74, respectively.

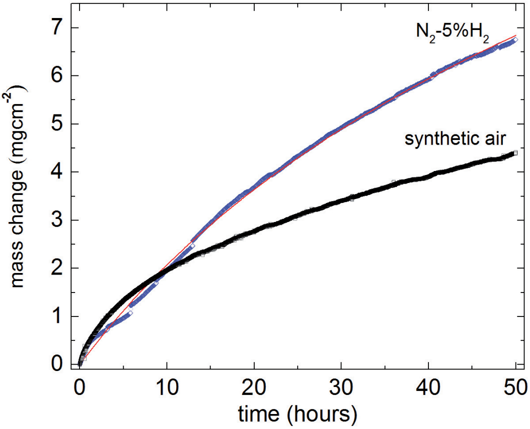

Figure 5-14. Comparative thermogravimetric data for two-phase Cr-Cr_3Si alloy (S16) exposed to N_2-5%H_2 and synthetic air at 1200°C for 50h.

5.6 Discontinuous gravimetry of the Cr-Si system

Discontinuous mass change data for pure Cr and Cr-Si alloys for 1000 hours isothermal exposure in synthetic air at 1200°C are shown in Figure 5-15. Pure chromium shows a continuous massive mass gain which leads to a mass gain of ca. 60 mgcm^{-2} after 1000h. Visual observation of a pure Cr specimen after 1000h clearly showed that the scale was not well adherent to the metal substrate, but just loosely connected to the substrate which is correlated to the unexpected high mass gain observed in Figure 5-15. Mass change curves of the single phase solid-solution alloy (S3) show severe spallation. The first oxidation cycle after 100h indicates a slight mass gain which can be correlated with the local coverage by a thin oxide layer on the surface after 1000h exposure. Two phase alloys also show spallation. However, the extent of spallation is different which can depend on the oxide remaining coverage after each cooling cycle and can affect the mass change. In general, Figure 5-15 indicates that addition of Si significantly reduces the extent of spallation at the end of the test and that the mass change curve of the single phase Cr_3Si alloy (S25) shows stable adhesion behavior throughout the oxidation test. A well adherent oxide appeared to fully cover the specimen surface which was visually observed at the end of the test.

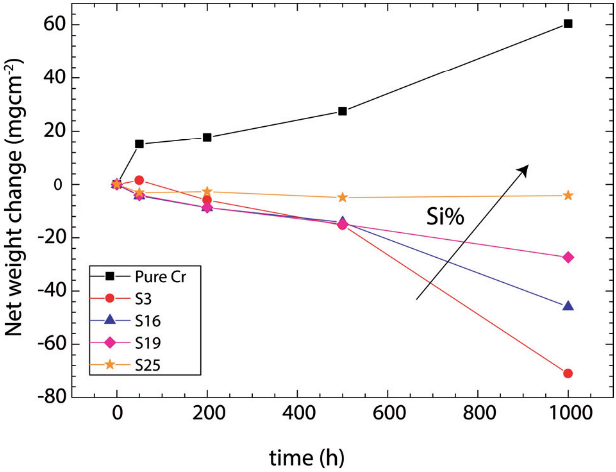

Figure 5-15. Discontinuous gravimetric oxidation measurement of Cr-Si alloys at 1200°C in synthetic air. At each point the sample was air cooled, weighed, and returned to the furnace (with kind permission from Springer Science and Business Media) .

5.7 Microstructural evolution in the Cr-Si system during oxidation

Figure 5-16 illustrates an overview of cross sections of oxidized pure Cr, single phase S3, eutectic S16, hyper-eutectic S19, and single phase S25 alloys after 100 hours isothermal and 1000 hours discontinuous isothermal exposure in synthetic air at 1200°C.

Microprobe analysis of the oxidized pure Cr and chromium solid-solution (S3) showed large differences in the post exposure microstructures. A ~300 µm deep layer of composition 70 at.% Cr, 30 at.% N corresponding to Cr_2N, was identified on the pure chromium substrate already after 100 hours oxidation. Chromium stripes of average composition (90 at.% Cr, 10 at.% N) formed within the nitride layer with different orientations towards the surface (see Figure 5-16a). These stripes are formed as a result of segregation of impurities which stabilize the solid-solution chromium phase during nitridation. The nitride layer shows a sharp transition at the interface to the Cr metal substrate. After 1000 hours oxidation, the bulk of the pure Cr coupon with a thickness of ~2mm was completely converted into nitride (Figure 5-16f).

The solid-solution alloy S3 shows a different morphology in the subscale zone. After 100h, it shows a thin continuous nitride layer and an internally oxidized subsurface region with finely dispersed SiO_2 particles. High magnification BSE images showed needle-shaped nitride precipitates that had formed within the grains and a continuous nitride network along the grain boundaries (Figure 5-16b). These findings are in accordance with observations of Steinmetz et al. on post exposure microstructures of diluted Cr(Si) alloys (0.5-5 at.% Si) oxidized in air at 1300°C for 20 hours [81]. Further oxidation of the alloy up to 1000 hours resulted in a microstructure consisting of a ~200µm thick Cr_2N-layer containing internally dispersed SiO_2 particles and a coarse grain boundary-nitride network (see Figure 5-16g).

Examination of the single phase S25 alloy exposed for 100h showed a subscale microstructure composed of a ~15 µm thick diffusion zone of the composition (63 at.% Cr, 37 at.% Si) corresponding to the stoichiometric Cr_5Si_3 phase, which had formed below the oxide scale (see Figure 5-16e). EPMA analysis revealed no sign of internal nitrides or oxides after 100 hours exposure and only negligible traces of N and O (~0.12 at.% N and 0.15 at.% O).

After 1000 hours exposure, the surface looks surprisingly different. A rough ~20 µm thick continuous Si-rich outer oxide layer remained on the surface (see Figure 5-16j). Under the oxide layer a thin layer of the composition 40 at.% Si, 40 at.% N, 20 at.% O corresponding to the stoichiometric Si_2N_2O (identified with EPMA) was observed. This phase is typically identified as an oxidation product of Si_3N_4 [139]. In contrast to the microstructure after 100 hours exposure, a 10 µm thick A15 layer had formed over an up to 20 µm thick Cr_5Si_3 diffusion layer at the metal-oxide interface, which means that the subsurface zone of the single-phase A15 alloy undergoes a complex microstructural evolution during the course of oxidation.

The microstructure of the eutectic alloy S16 after 100h oxidation shows a ~20 µm Cr_3Si layer underneath the alloy-scale interface, with internal silicon oxide and some nitrides below this A15 zone, which mimics the morphology of the former solid-solution phase in the eutectic structure. (Figure 5-16c). By extending the exposure time to 1000 hours, the A15 layer under the oxide grows to ~55 µm, with a nitrided zone of ~150 µm underneath (see Figure 5-16h).

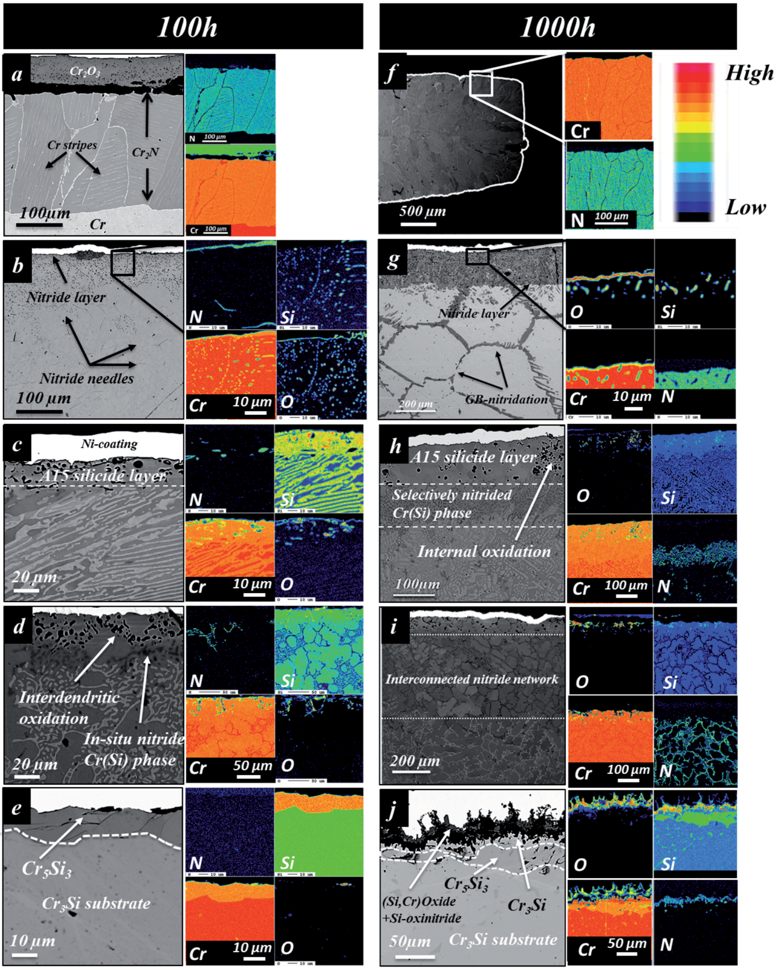

Figure 5-16. Post exposure cross sections of a) pure Cr, b) single phase alloy S3, c) eutectic alloy S16, d) hyper-eutectic alloy S19, and e) single phase alloy S25, after 100h and 1000h exposure in synthetic air at 1200°C (with kind permission from Springer science and business media) [81].

The hyper-eutectic alloy S19 also shows a thin silicon-rich zone after 100 h, but underneath a larger amount of the chromium solid-solution lamellae of the eutectic network around the A15 dendrites was already selectively consumed by nitridation (see Figure 5-16d). After 1000 hours, in contrast to alloy S16, no outer A15 layer is present and the depth of nitridation has strongly increased (Figure 5-16i). It forms an inter-dendritic nitride network throughout the eutectic region of the entire cross section (2 mm thick) due to the merged reaction zone from both sides of the sample.

Figure 5-17 illustrates the influence of additional oxidation (O_2) on nitridation of the two-phase eutectic alloy (S16). The cross section of the alloy after 50h oxidation in synthetic air is compared to that exposed in N_2-5%H_2. It is evident that in the absence of oxygen in the N_2-H_2 atmosphere, a nitridation affected zone of 250 µm thickness is formed which is significantly deeper than that formed under synthetic air for which the formation of a subscale A15 layer and a much lower extent of internal nitridation is observed (see Figure 5-17b).

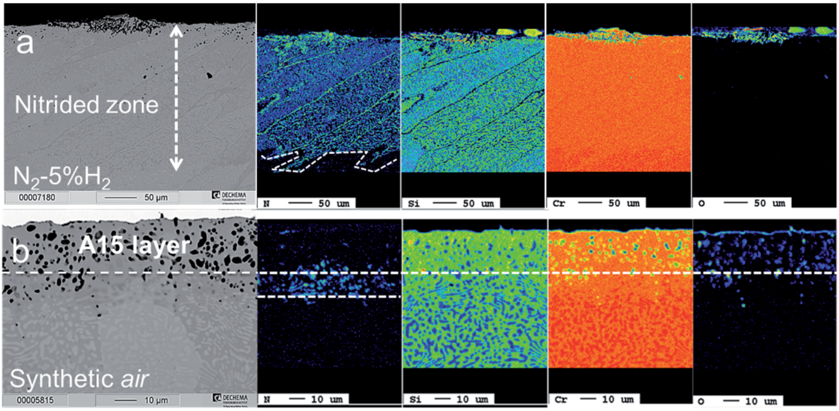

Figure 5-17. Cross section of the two-phase Cr-Cr_3Si alloy (S16) after 50h oxidation at 1200°C in a) N2-5%H_2 and b) synthetic air.

5.8 Oxidation-nitridation in the Cr-Ge-Si system

5.8.1 Ge-alloyed Cr-Cr_3Si alloys

The mass changes of the binary Cr-Cr_3Si (S16) and ternary Cr-Cr_3(Si,Ge) alloys (SG1, SG2, and SG12) at 1350°C are summarized in Figure 5-18. All alloys initially show a rapid mass gain followed by typical parabolic growth. To quantify the detailed oxidation kinetics, mass change curves were fitted with Eq. 14, as explained in section 5.2. The fits show that oxide growth on all alloys follows the paralinear kinetics described by Eq. 14. Several interruptions can be observed in mass change curves in Figure 5-18. Most of these discontinuities are observed for alloy S16, while in the Ge-alloyed specimens only one step is observed at t=18-20h. In order to compare the effect of these discontinuities on the overall oxidation kinetics, fitting was applied for each stage and the corresponding fitting parameters are extracted, averaged, and compared to the single fit applied for the complete exposure range by averaging over stages. Since no noticeable differences are found (see Figure 5-18a), the fit applied to the whole range was applied to further investigations.

Figure 5-19 illustrates the values of k_p and k_v as a function of Ge/Si ratio. It confirms that addition of only 1 at.% Ge to the binary Cr-Si alloy decreases both the parabolic rate constant and the evaporation rate by up to a factor of three, while increasing the Ge-content to 2 at.% does not further improve the oxidation kinetics. By addition of 12 at.% Ge a significant increase in both the parabolic rate constant and the evaporation rate is observed. The TG-curve corresponding to alloy SG12 shows the highest evaporation rate of all alloys.

Considering the results obtained so far, it is known that germanium additions higher than 2 at.% do not improve the oxidation resistance considerably and are rather detrimental. Therefore, 2 at.% Ge were selected for further oxidation studies.

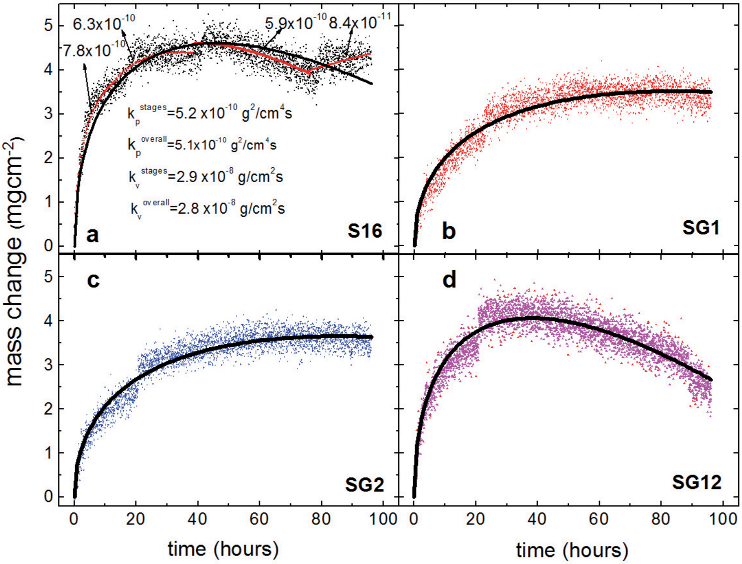

Figure 5-18. Isothermal gravimetric data and corresponding fits for Cr-Ge-Si alloys oxidized in 1 atm synthetic air for 100h at 1350°C (with kind permission from John Wiley and Sons) [14].

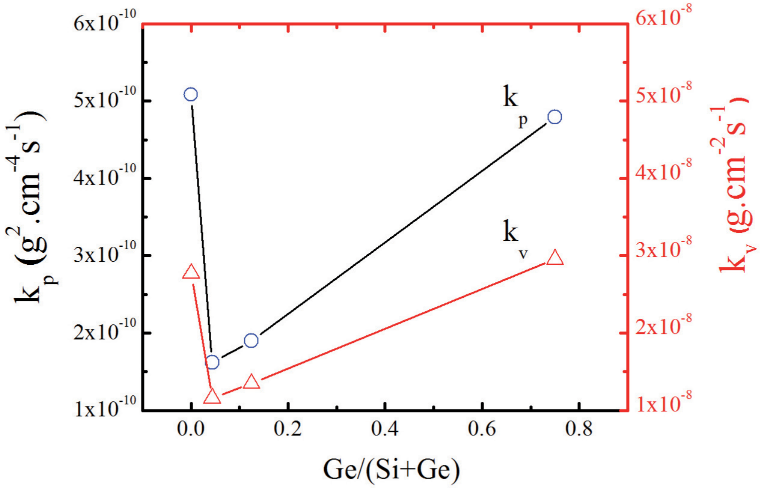

Figure 5-19. Effect of Ge additions on the parabolic constant (k_p) and the volatilization rate (k_v) (with kind permission from John Wiley and Sons) [14].

Figure 5-20 illustrates the thermogravimetric data for the alloys S16, SG1, and SG2 during 50h exposure at 1200°C. The mass change curves were fitted accordingly using Eq. 14 to quantify the paralinear kinetics parameters. Addition of Ge is found to be beneficial for oxidation kinetics as the alloy with 2 at.% Ge shows the slowest oxidation kinetics in accordance with the results at 1350°C. Additions of Ge reduce the maximum mass-gain by a factor of two.

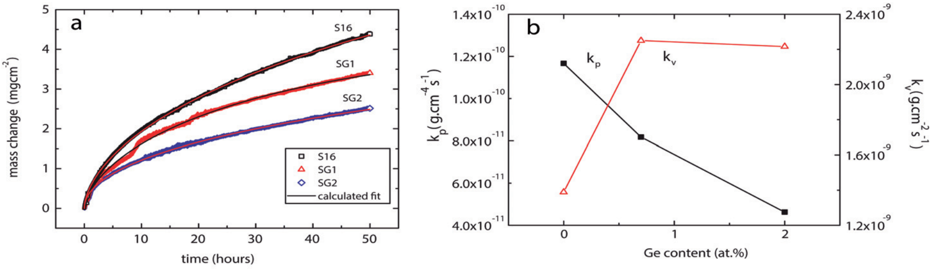

Figure 5-20.a) Thermogravimetric curves of unalloyed and Ge alloyed Cr-Cr_3Si alloys during exposures in synthetic air at 1200°C. b) Effect of Ge on the corresponding values of the parabolic constant k_p and the linear volatilization rate k_v.

5.8.2 Discontinuous Gravimetry of the Cr-Ge-Si alloys

Specific mass change data for unalloyed and Ge-alloyed Cr-Cr_3Si two-phase alloys after 1000h discontinuous isothermal exposure at 1200°C in synthetic air are shown in Figure 5-21. The reference binary alloys S16 and S19 and their long term oxidation behavior upon alloying with Ge were investigated. Isothermal tests were interrupted with cooling stages after 50, 200, 500, and 1000h exposures.

The eutectic Cr-Cr_3Si alloy illustrates mass loss due to spallation of the oxide scales upon cooling. Although 1 at.% Ge addition did not provide significant scale adhesion, additions of 2 at.% showed less spallation with mass gains after 50h oxidation for up to 500h. In the latest stage of oxidation, significant mass loss is also observed, but less than that of alloy S16.

The effect of increasing both Si and Ge contents on the long term oxidation behavior was investigated for hyper-eutectic Cr-Cr_3Si alloy S19 and alloy S18G1. Figure 5-21b shows that the binary hyper-eutectic alloy S19 experiences continuous mass loss after all cooling stages. Alloying of only 1 at.% Ge notably improves the scale adhesion as after all cooling stages mass gain is recorded.

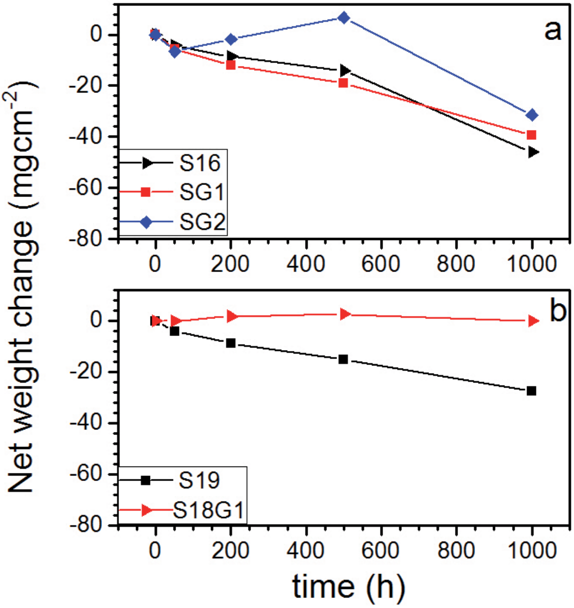

Figure 5-21. Effect of Ge alloying on the long term discontinuous oxidation behavior of a) solid-solution Cr_{ss}, b) eutectic, and c) hyper-eutectic Cr-Cr_3Si alloys.

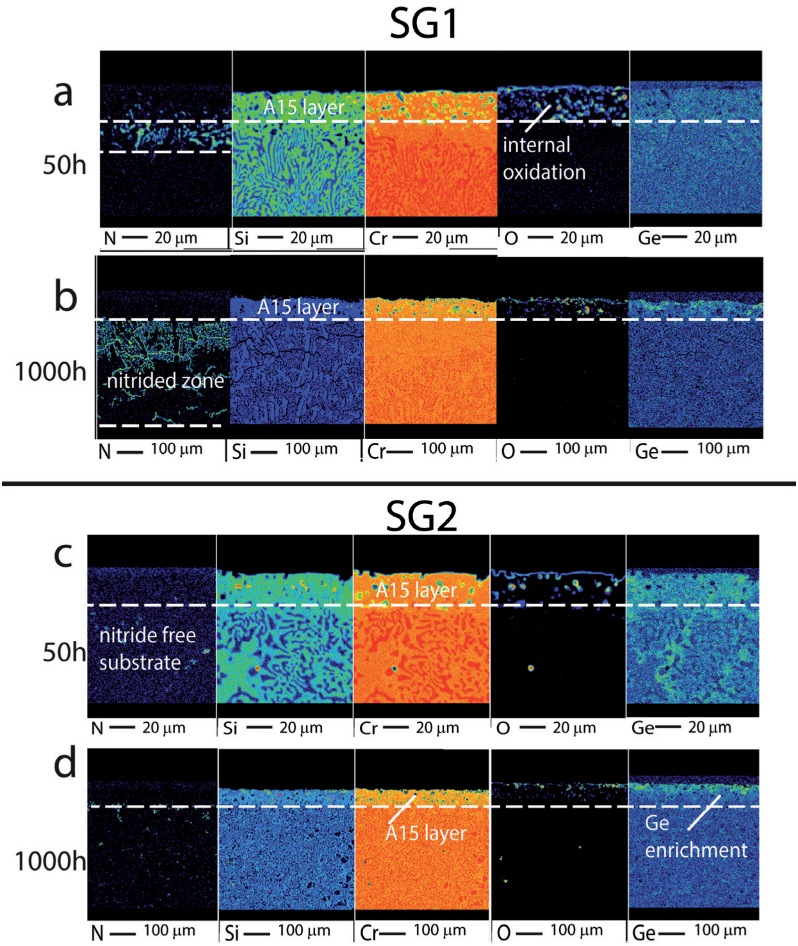

Figure 5-22. Post oxidation cross sections of alloy SG1 (a, b) and SG2 (c, d) after 50h and 1000h exposures in synthetic air at 1200°C.

5.9 Post-oxidation morphology of Ge-alloyed Cr-Cr_3Si alloys

Figure 5-22 shows cross sectional element distribution maps of the oxidized Ge-alloyed two-phase Cr-Cr_3Si alloys after 50 and 1000h exposure in synthetic air at 1200°C. Comparing the subsurface microstructure of the eutectic alloy S16 (Figure 5-16c, h) with alloys SG1 and SG2 similar microstructural features can be noted; a subsurface A15 silicide layer and the substrate microstructure. Attention, must however, be paid to the fine microstructure of the alloy substrate, the internal oxidation in the A15 layer, and the internally nitrided zone below the A15 layer (Figure 5-21). Alloy SG1 shows an A15 silicide layer of ~22µm thickness including internal oxides of mainly chromium but also silicon. Underneath the A15 layer is a 15 µm zone with selectively nitrided lamellae representing nitridation of the chromium solid-solution phase. After longer exposures, the nitridation front advances further into the substrate to ~300-µm depth (Figure 5-22b). Increased Ge content in alloy SG2 (2 at.%Ge) alters the extent of internal porosity that is filled with internal oxides and more importantly the extent of the nitrided zone which does not appear even after 1000h (see N map in Figure 5-22c,d). Compared to alloy SG1, Ge saturation is more significant at the metal-oxide interface and especially in the subsurface A15 layer.

Figure 5-23 shows the quantitative line scan starting from the metal-oxide interface up to the end of the A15 subscale layer in the S16 alloy. Formation of a layer with ~105 µm thickness is evident which represents the stoichiometric composition of the Cr_3Si phase. Throughout the A15 layer, a gradual chemical gradient is observed having Cr concentrations of 75.4 and 77.7 at.% observed at oxide-substrate interface and the inner end of the layer, respectively. A correlative gradient is observed for Si across the A15 layer. Below the A15 layer, the first Cr_{ss} lamellae are evidently transformed into nitride with ~30 at.% N content (see Figure 5-23a).

Quantitative line scans of alloy SG2 (Figure 5-23b), reveal a significantly thinner A15 layer with a thickness of ~52 µm. Similar composition gradients as for alloy S16 are observed at both sides of the A15 layer with 2 at.% difference in Cr contents across the A15 layer. It should be noted, however, that contrary to alloy S16, the gradients of Si and Ge are higher than that of chromium as composition differences of ~4.4 and ~3.8 at.% are observed for Si and Ge at the two sides of the A15 layer (see Figure 5-23b). Beneath the A15 layer, a fluctuation of the chromium content between ~93 and 77 at% can be detected which corresponds to the lamellar structure. The composition of the Cr_{ss} lamellae below the A15 layer show a negligible content of nitrogen (~ 0.1 at.%) which is similar to that measured in the A15 lamellae. The average compositions of the subscale A15 layers in alloys S16 and SG2 are listed in Table 5-5. As Table 5-5 shows, negligible solubility of nitrogen (0.1 at.%) in the A15 phase is detected while there is no solubility for oxygen.

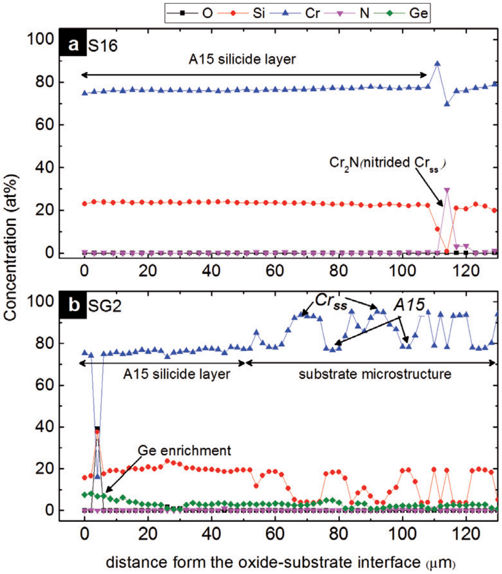

Figure 5-23. Quantitative line scans of elements through the subsurface region of oxidized a) S16 and b) SG2 alloys after 1000h oxidation at 1200°C.

Table 5-5. Average composition of the A15 silicide layer after 1000h oxidation at 1200°C.

Elements	*A15 subscale layer*	
	S16	SG2
O	0	0
Si	23.3	19.7
Cr	76.6	76.4
N	0.1	0.1
Ge	0	3.6

5.10 Characterization of the oxide scales

5.10.1 Oxide scale morphology

Figure 5-24 shows the morphology of the outer surface of the thermally grown scale on different alloys after 100h exposure at 1200°C in synthetic air examined using the SEM. The chromia scale formed on pure chromium shows a fine-grained morphology with microscopic wrinkles forming a wavy oxide topology. As Si is added to chromium (see Figure 5-24b), the morphology of chromia seems to be finer than that of pure Cr. However, very large crystals (20-50µm) with typical trigonal facets embedded in the fine structured scale appear on the surface. Signs of deformation are evident on the crystals as parallel lines on theirs facets formed on alloy S3. Lateral parallel lines indicate dislocation slip planes parallel to the scale growth direction (Figure 5-24b).

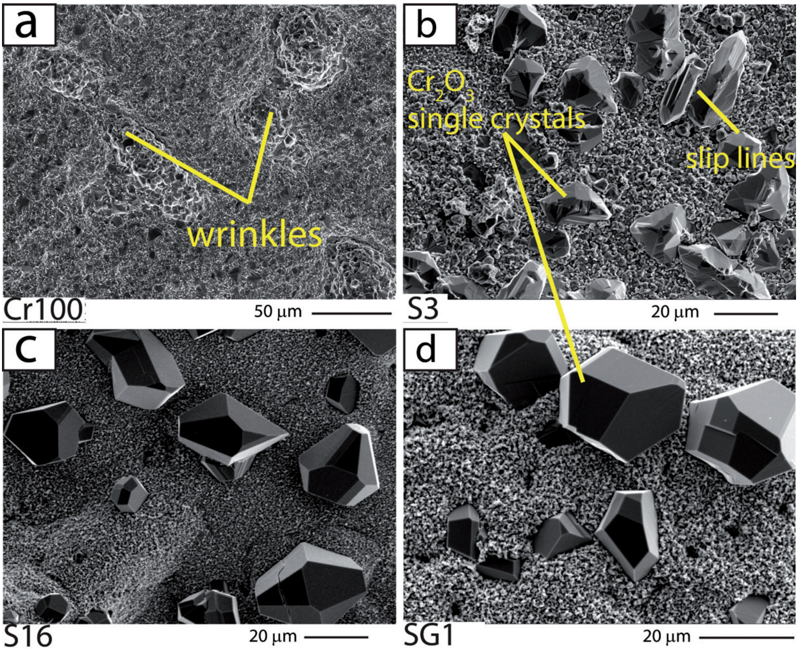

Figure 5-24. Morphology of the oxide scales formed on a) pure Cr, b) S3, c) S16, and d) SG1 after 100h oxidation in synthetic air at 1200°C.

Table 5-6. Compositions of the isothermally grown oxides illustrated in Figure 5-24.

Alloy	*Scale composition (at.%)*			
	Cr	Si	Ge	O
Pure Cr	48.83	0	0	51.17
S3	47.19	0.36	0	52.45
S16	39.34	0.30	0	60.37
SG1	39.19	0.34	0.04	60.43

The oxide scales formed on alloys S16 and SG1 illustrate a morphology composed of a fine chromia matrix and larger chromia single crystals compared to those seen on alloy S3. The single crystals, however, show significantly fewer parallel lines and rather shiny facets (Figure 5-24c-d). SEM images clearly indicate that these crystals form initially within the oxide and grow further outwards from the surface.

The chemical compositions of the outer surface of the scales shown in Figure 5-24 are listed in Table 5-6. They indicate that regardless of the alloys original Si content, the scales contain approximately similar amounts of 0.3 at.% Si for all alloys. In Alloy SG1, the oxide scale shows negligible traces of Ge (Ge ≈ 0.04 at.%).

The morphology of the oxide scales after 50h isothermal exposure at 1050°C are shown in Figure 5-25. The morphology of the chromia scales looks different from that of the alloys oxidized at 1200°C. Scales formed on the alloys S3, S16, and SG1 at 1050°C show a coarser grain structure compared to those formed at 1200°C. In addition, the large embedded single crystals do not appear on the oxide surface (see Figure 5-25b-d).

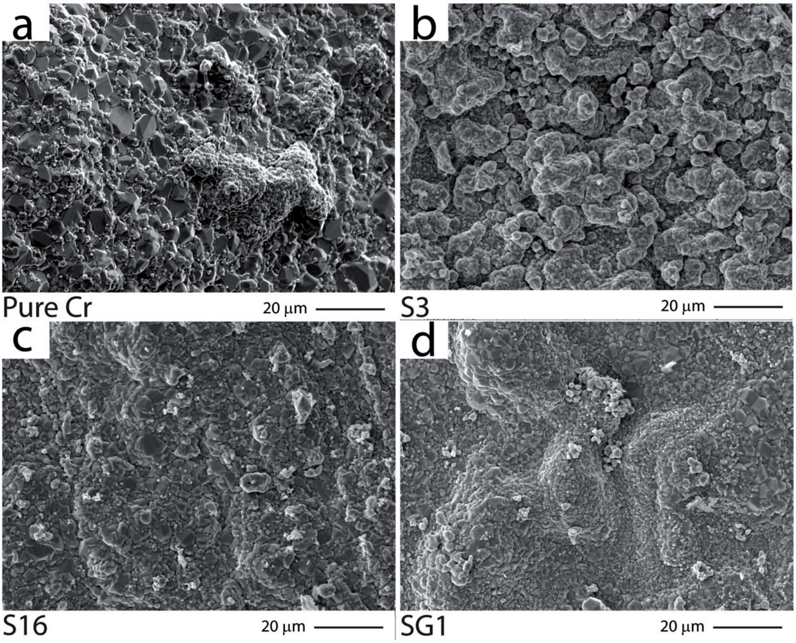

Figure 5-25. Top view of the chromia scales formed on a) pure Cr, and alloys b) S3, c) S16, and d) SG1 after 50h oxidation at 1050°C.

The inner side (facing the metal surface) and the chemical composition of the spalled scales of alloy S3, S16, and SG1 formed after 100h exposure at 1200°C are presented in Figure 5-26. The existence of SiO_2 underneath the chromia scale is evident as Si-rich phases in the form of particles appear when 3 at.% Si is added (Figure 5-26a).

Similar Si-rich regions are detected on the inner side of the scales formed on alloy S16 and alloy SG1 (Figure 5-26b-c). The detected zones locally cover the inner side of the scale. The local observation of Si-rich oxide on the inner side of the scale could mean that SiO_2 residues should be expected in contact with the metal substrate. It has to be noted, however, that locations away from these zones still show significantly higher Si contents compared to the composition of the outer side (see Figure 5-26b). It is important to note that the wrinkles observed on the outer side of the scale (Figure 5-24) appear as deep cavities on the inner side of scales (see Figure 5-26b-c).

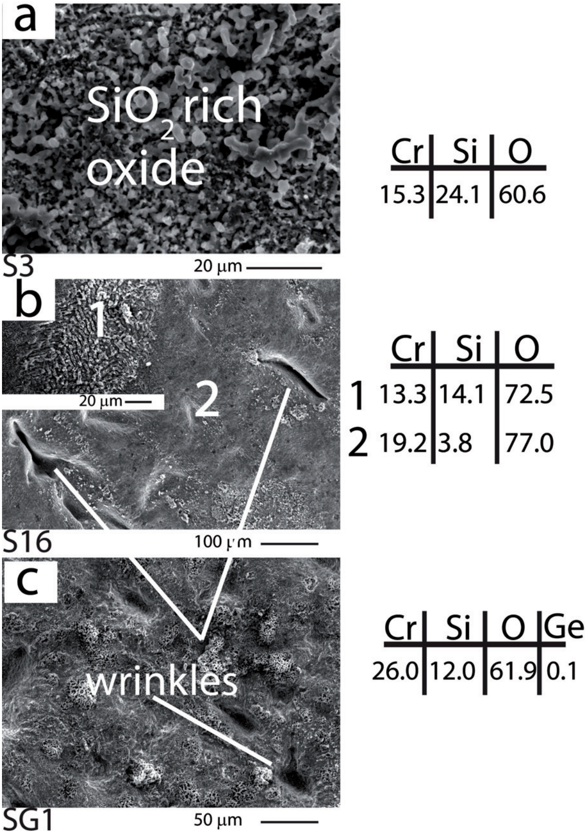

Cr	Si	O
15.3	24.1	60.6

	Cr	Si	O
1	13.3	14.1	72.5
2	19.2	3.8	77.0

Cr	Si	O	Ge
26.0	12.0	61.9	0.1

Figure 5-26. Inner side morphology and composition of the spalled scales which had faced the metal surface on alloys a) S3, b) S16, and c) SG1 after 100h exposure at 1200°C.

5.10.2 Crystallographic Structure of the oxide scales

X-ray powder diffraction patterns of the finely ground oxides formed after 1000 hours exposure at 1200°C are shown in Figure 5-27. They reveal that the predominant oxidation product in all Cr-$Cr_3(Si,Ge)$ alloys is Cr_2O_3 with an eskolaite crystal structure. Comparing the diffractograms representing the oxide scale for pure Cr with that of the Si containing alloys, a low intensity peak can be noted at $2\theta \approx 10°$ which corresponds to (100) α-cristobalite (SiO_2).

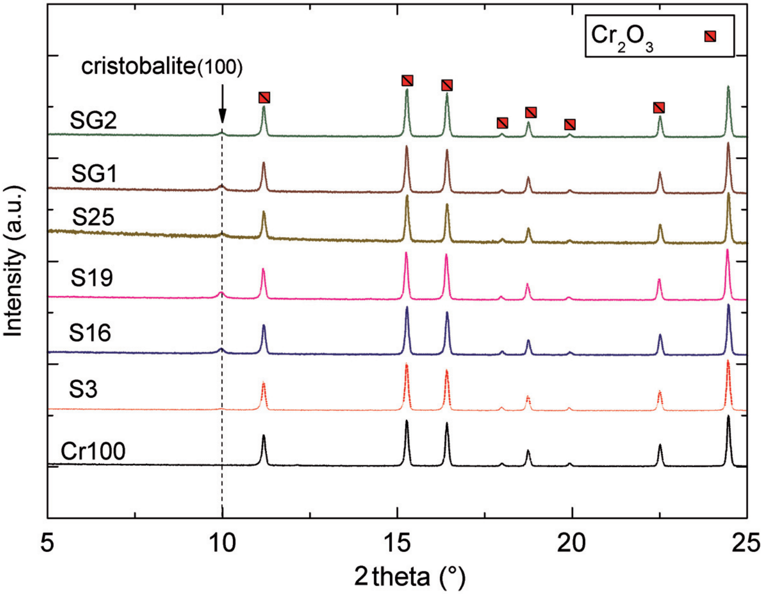

Figure 5-27. X-ray diffraction patterns of the spalled oxide scales after 1000h oxidation at 1200°C (note the single SiO_2 reflection at 2θ = 10°).

The refined X-ray diffraction data on one of the single crystals observed on the scale surface of the alloy SG1 indicate that it is a single crystal of eskolaite (Cr_2O_3) with lattice constants of a = b = 4.958(1) Å, c = 13.596(1) Å, $\alpha = \beta = 90°$, $\gamma = 120°$.

5.10.3 Morphology of the subscale surface

The morphology of the oxide remnants on the substrate after scale spallation after 100h continuous and 1000h discontinuous isothermal exposures is shown in Figure 5-28 and Figure 5-29, respectively. Figure 5-28a shows a position where the cross section of the chromia scale is visible with a thickness of ~15-20 μm. The scale is obviously detached from the substrate. Dispersed crystals growing perpendicularly to the substrate can be detected on both the inner side of the scale and the substrate surface. EDS results indicate that these particles are pure SiO_2 (see Figure 5-28a). At lower magnifications of a spot, where the oxide had spalled, it is clearly seen that SiO_2 particles are concentrated at grain boundary regions. The back scattered image clearly shows that these SiO_2 particles are surrounded by a Cr_2O_3 matrix which covers the surface of the alloy (Figure 5-28a). The subscale morphology of the eutectic binary alloy (S16) shows a higher coverage with SiO_2 which is proven by EDS analysis (Figure 5-28b). SEM analysis of multiple parts of the specimen (not shown here) showed that the SiO_2 is covered with Cr_2O_3. However, at some parts, spallation leads to the appearance of a SiO_2 layer underneath chromia. SEM analysis of the morphology of alloy S25 in BSE mode shows a uniform SiO_2 layer with higher coverage (Figure 5-28c) determining the threshold to form a continuous outer SiO_2 layer in this system. Alloy SG1 shows a similar morphology to alloy S16 (Figure 5-28d). The coverage of SiO_2 and Cr_2O_3 is clearly shown in BSE mode. EDS analysis

Zone	Cr	Si	O
1	1.1	31.3	67.6
2	56.8	0.6	42.7
3	38.4	12.7	48.91

Zone	Cr	Si	O
1	1.3	40.13	58.6
2	43.2	26.3	30.5

Zone	Cr	Si	O	Ge
1	51.8	14.3	32.9	1.1
2	0.8	36.3	62.7	0.2

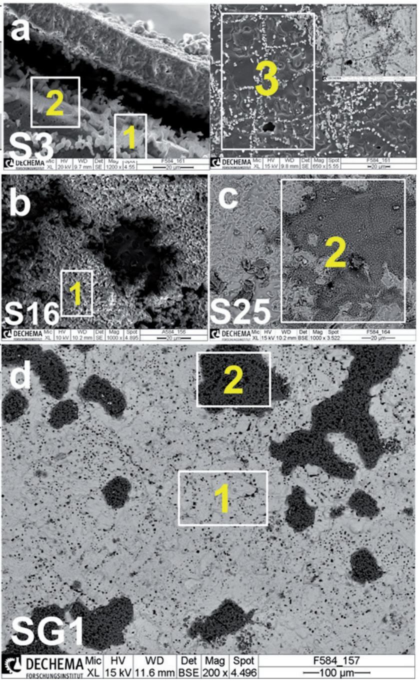

Figure 5-28. Evolution of the subscale substrate of the alloys after 100h isothermal oxidation at 1200°C. a) S3, b) S16, and c) S25and d) SG1, EDS results show the compositions of the white squares in at%.

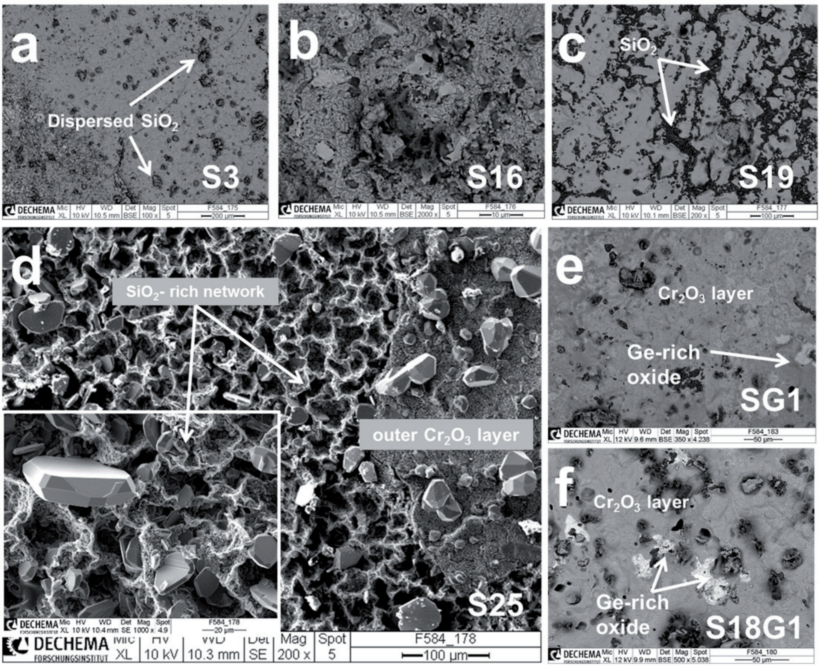

Figure 5-29. Evolution of the subscale surface morphology on alloy a) S3, b) S16, c) S19, d) S25, e) SG1, and f) S18G1 after 1000h discontinuous isothermal exposure at 1200°C.

on the dark and bright parts of the image indicates the composition of the oxides, where position 1 and position 2 in Figure 5-28d represent Cr_2O_3 and SiO_2, respectively. Attention must be paid to the Ge signal in the EDS spectra revealing up to 1.1 and 0.2 at.% Ge in Cr_2O_3-rich and SiO_2-rich oxides, respectively.

Figure 5-29 shows the morphology of the oxide remnants on the substrate alloys which were discontinuously oxidized for 1000h at 1200°C. The corresponding mass change profiles of these substrates are presented in Figure 5-15 and Figure 5-21. The dispersed SiO_2 crystals observed in Figure 5-28a are still evident after 1000h oxidation on the subscale surface of alloy S3 (Figure 5-29a). Higher Si content in alloy S16 and S19 increases the coverage of SiO_2 which shows in some areas higher adherence to the overlaying chromia layer. For instance, alloy S19 shows a pattern of dendritic shape chromia (light grey area) surrounded by SiO_2-rich regions (dark area). The light grey area represents higher adhesion of chromia to the underlying silica layer in those regions while the darker area shows the spallation of chromia from the silica layer in Figure 5-29c.

Single phase Cr_3Si alloy S25 represents an adherent chromia scale which did not spall during discontinuous oxidation and cooling cycles. The outer scale was similar to those described in section 5.10.1. To understand the source of adherence, some part of the outer scale was carefully scratched off to see the morphology underneath the outer chromia oxide layer. Underneath the outer chromia layer a network had formed, composed of SiO_2 with macro-pores in the range of (30-50 µm) covered with chromia crystals (Figure 5-29d).

The effect of Ge addition on the adhesion of the oxide scales can be seen by comparing the morphology of alloys SG1 and S18G1 with that of the alloys S16 and S19, respectively. It is shown that alloy SG1 has a higher coverage of chromia on the underlying SiO_2 layer. (Figure 5-29). A similar feature was observed for alloy SG2 (not shown). Signs of chromia spallation revealing dark SiO_2 areas on alloy S19 are significantly reduced for alloy S18G1 (compare Figure 5-29e and Figure 5-29f). The overall composition of the oxide layers indicates that addition of Ge to the S16 and S19 alloys increases the Ge content in the oxides accordingly. Up to ~3.5 and 0.7 at.% Ge is measured on the substrate surface of alloy SG1 and S18G1, respectively. Enrichment of Ge in some areas of the oxide layers is clearly visible as white areas (Figure 5-29e-f).

6 DISCUSSION

6.1 Oxidation and nitridation of pure chromium

The parabolic rate constants for oxidation in air (k_p), in oxygen (k_p^{ox}), and nitridation in nitrogen (k_p^{nit}) were measured at temperatures of 950-1200°C. The typical Arrhenius plot showing the comparative dependence of k_p values for oxidation of pure chromium determined in this work and in the literature is illustrated in Figure 6-1. The sources of discrepancies in the reported k_p values in the literature have already been discussed in section 2.5.1. However, additional facts should be added to the sources of discrepancies discussed in the literature.

Firstly, k_p values reported for pure chromium oxidized in air (O_2-N_2) are often compared with the values obtained from oxidation in pure oxygen atmosphere (see Figure 6-1). It is shown in Figure 5-2 that nitridation of chromium in nitrogen is significantly faster than oxidation in oxygen atmosphere. Interestingly, the aggregated rate of oxidation plus nitridation in the multi-oxidant atmosphere (i.e. synthetic air) is approximately similar to the sum of independent oxidation and nitridation rates in single oxidant atmospheres. This implies that nitridation adds the main contribution to the parabolic mass change in air which induces a significant difference compared to the parabolic rate constant in pure oxygen. In agreement with this finding, literature k_p values reported for chromium oxidized in air are often reported to be higher than those oxidized in pure oxygen (see Figure 6-1).

Secondly, thermogravimetry of chromium oxidation at high temperatures is usually accompanied by the formation of discontinuities leading to multiple growth steps which in turn, increase the total mass gain and the overall kinetics of oxidation (see

Figure 5-1). Formation of these steps influences the final value of the parabolic rate constant and reflects the observed discrepancies in the reported k_p values. In-situ acoustic emission and electron microscopy of scale cross sections clearly showed that discontinuities in the thermogravimetric curves occur as a result of local oxide failure such as microscopic cracking and blistering, scale detachment, etc. during scaling. Formation of discontinuities as a result of local defect formation in the oxide is a stochastic event and therefore, can hardly be predicted.

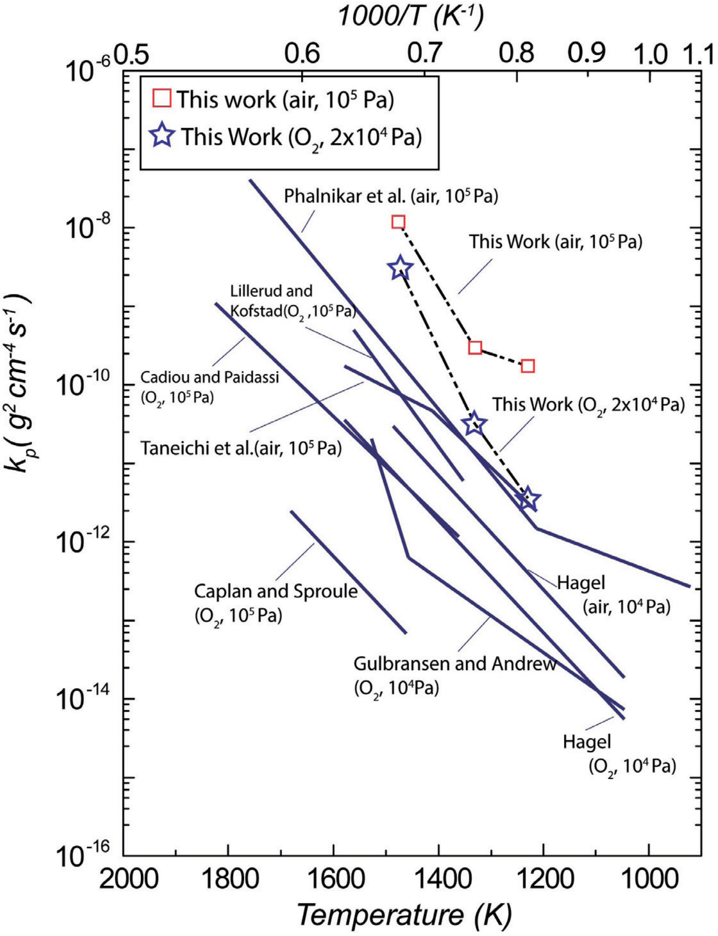

Figure 6-1. Influence of temperature on the parabolic rate constant of pure chromium. Results of this work are marked as squares and stars.

The third factor is volatilization. The kinetics of oxidation at temperatures higher than 900°C should include an additional negative term, k_v. However, in most references, k_p is solely calculated from a parabolic relation without taking the negative term into account which can lead to different values [23,68]. Considering the above mentioned influences and variations in data evaluation and those discussed in section 2.4, it is not surprising that different rates of oxidation are reported from different experiments (see Figure 6-1). The temperature dependence of oxidation, volatilization and nitridation follows an Arrhenius relation (Eq. 5) where Q is the activation energy. Activation energies calculated based on quantitative data in Table 5-1 are summarized in Table 6-1. The activation energy of oxidation in O_2 atmosphere in this work is higher than those reported by Caplan et al. [54], Kofstad et al., and Gulbransen [35,39] which can be related to differences in surface preparation as none of the references used mechanically polished specimens. Other methods such as thermally etched, electro-polished and etched surfaces were used in these works (see Table 1).

It is frequently reported that volatilization of chromia becomes important above 900°C [35,39,40,94,95]. The activation energy of volatilization during oxidation of pure chromium in air and in pure oxygen is listed in Table 6-1 . The close range of activation energies obtained for oxidation in air and Ar-O_2 atmospheres indicates the mutual mechanism of volatilization which is governed by Eq. 8. In fact, as P_{O_2} in both atmospheres is the same, nitrogen and argon are not expected to affect volatilization. To the best of my knowledge, this is the first time a value is given for the activation energy of volatilization of thermally grown chromia; Hagel reported the activation energy for volatilization of sintered chromia as 204.2 kJmol^{-1} [41].

Table 6-1. Activation energies for parabolic growth, volatilization, and nitridation of pure chromium in different atmospheres.

Reaction	*Atmosphere*	*Temperature (°C)*	*Q (kJmol^{-1})*
Oxidation-Nitridation	Syn. air (N_2-21%O_2)	950-1200	248.6
Volatilization	Syn. air (N_2-21%O_2)	1050-1200	296.7
Nitridation	N_2-5%H_2	950-1200	229.4
Oxidation	Oxygen (Ar-20%O_2)	950-1200	404.1
Volatilization	Oxygen (Ar-20%O_2)	950-1200	259.7

Figure 5-1c shows the kinetics of nitridation in N_2-5%H_2 atmosphere at all testing temperatures. Thermogravimetric results of nitridation of Cr in N_2-H_2 atmosphere indicate that nitridation is diffusion controlled showing a parabolic mass gain profile [88,127]. As oxygen is not present in the N_2-H_2 atmosphere, volatilization is not expected to occur and Eq. 8 does not apply. Thus, the kinetics should solely be governed by parabolic kinetics.

The result in Table 5-1 are used to calculate the Arrhenius relation for temperature dependency of the nitridation rate k_p^{nit} as

$$k_p^{nit} = 0.00071 \exp\left({-229359}/_{RT} \right) (g^2 cm^{-4} s^{-2}). \tag{18}$$

Comparing the parabolic rate constants shown in Figure 5-2 reveals that the parabolic rate of mass increase in air (k_p) is approximately similar to the sum of the parabolic rate constants in oxygen (k_p^{ox}) and nitrogen atmosphere (k_p^{nit}) (Eq. 16).

On the other hand it is observed that the isothermally oxidized samples in air show a nitride layer underneath the chromia scale in the form of a continuous nitride layer with a sharp diffusion front to the metallic substrate (see Figure 5-16a). These observations are in accordance with others observations [32,83,84,140] and indicate that chromia does not act as a protective barrier against nitrogen at high temperatures. Nitrogen penetrates through the chromia scale and leads to the formation of a uniform nitride layer.

Three hypotheses can be put forward for nitrogen transport through chromia and subsequent Cr_2N formation under the chromia scale. .

1. Some refer to the thermodynamic requirement for the stability of chromium nitride which requires high nitrogen partial pressure and extremely low oxygen partial pressure. Besides, nitrogen shows negligible solubility in chromia [78]. Therefore, they argue that lattice diffusion of nitrogen in chromia scale cannot take place and thermodynamic conditions can exclusively be granted if scale breakdown or macro cracking take place during oxide growth [23]. However, oxide cracking in air gives way to both nitrogen and oxygen. As a result within a crack the oxygen partial pressure cannot be low enough for the nitride to become stable (see Figure 2-4a) [23].

2. Some others utilized atom probe tomography (APT) to reconstruct the oxide microstructure after high temperature exposure in CO_2 atmosphere. They observed carbon in chromia grain boundaries and assumed that carbon, and in fact other interstitial elements such as nitrogen can penetrate through chromia via grain boundary diffusion [141,142].

3. The third hypothesis is based on dynamic micro-crack formation and a healing process mechanism in the scale via the following progress. The counter current diffusion of chromium and oxygen in the chromia scale grain boundaries causes formation of fresh oxides within the scale. Unlike the growth at the scale-gas interface, this growth process is not stress free. In fact, formation of the new oxide

grains inside the scale leads to compressive stress in the adjacent grains and numerous formations of new oxide grains inside the scale can cause a large accumulative compressive stress. For the example of NiO, Rhines and Wolf proved the development of compressive stresses by the countercurrent diffusion of oxygen anions and metal cations [143]. Later Atkinson et al. showed that the intrinsic compressive stresses in NiO causes micro-crack formation at the oxide grain boundaries which facilitates molecular oxygen transport through the scale [144]. Despite the lack of experimental data, a similar process can be expected for chromia as enormous intrinsic growth stresses are observed in thermally grown chromia [44,56]. The micro-cracks can be accordingly healed with the fresh oxide. The superposition of micro-cracking and healing processes can continue along the scale as long as the new oxide formation inside the scale continues. The dynamic crack formation and healing process leads to the "permeability" of the chromia scale for quasi gas-phase transport (nitrogen and oxygen) through the scale which can temporarily be open to the gas atmosphere [145]. Thus, during oxidation in air, molecular oxygen and nitrogen can simultaneously permeate through the scale via the dynamic micro-crack network explained above. Oxygen is consumed for the healing process (for formation of the fresh oxide grains). Therefore, molecular nitrogen passes through the micro-crack network towards the chromium substrate. In this case, thermodynamic conditions are fulfilled for the formation of the chromium subnitride Cr_2N. A schematic illustration of the hypothesis is shown in Figure 6-3.

None of these theories have been experimentally proven yet. However, the probability of each theory based on thermodynamics and kinetics of nitridation can be discussed.

The formation of Cr_2N requires a significantly lower partial pressure of oxygen than that of nitrogen (see Figure 2-4). Macro-crack formation and oxide breakdown in air gives way to both nitrogen and oxygen at the same time leading to oxide stabilization rather than nitride formation. Thus the theory based on oxide macro cracking and oxide break down is not thermodynamically feasible.

The second theory based on the permeation of nitrogen through the scale via grain boundary diffusion has a certain thermodynamic probability. However, it should also be kinetically feasible. The kinetics data listed in Table 5-1 shows that the rate of nitridation of chromium is approximately three times faster than that of oxidation. Based on this theory, both nitrogen and oxygen are assumed to diffuse along the grain boundary. Thus, in order to meet the thermodynamic requirements for nitride stability, the diffusion rate of nitrogen along the chromia grain boundaries should be markedly higher than that of oxygen. Furthermore, the solid state diffusion rate of nitrogen through the chromia scale should be higher than that in the chromium metal substrate to assure enough nitrogen supply for continuous nitride formation. The use of atom probe tomography is of great help to reveal the transport mechanism. Nevertheless, no experimental data exists for the nitrogen transport in chromia. The observations made for the transport mechanism of carbon are assumed to be similar for nitrogen [141,142]. Local carbon segregations at the chromia grain boundaries are evident in these studies. Considering the grain boundary diffusion of carbon in these studies, it is surprising that carbon is not equally distributed in the grain boundaries and not all the grain boundaries contain carbon. Furthermore, most of the chromia-forming steels do not show internal nitridation. For instance, the stainless steel AISI 446 shows no internal nitridation after 100h oxidation in air when a continuous chromium oxide is formed on the surface (see Figure 6-2). However, nitrides can form locally under the oxide nodules resulted from local oxide failures. With the assumption of nitrogen transport along the grain boundaries, one would expect nitride formation in all chromia-forming steels.

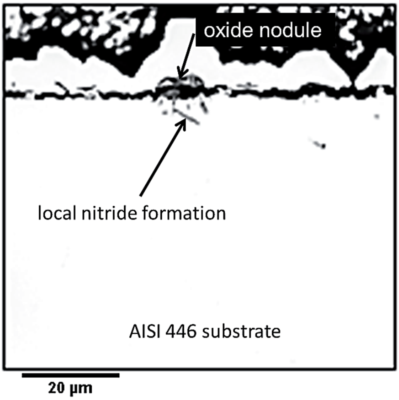

Figure 6-2. Cross section of stainless steel AISI 446 after 100h oxidation in air at 1000°C. Note the local nitride formation under the oxide nodule after [146].

The third hypothesis based on dynamic micro-crack formation and healing process can meet both mentioned thermodynamic and kinetic requirements. The dynamic formation of micro-cracks and their healing can lead to nitrogen transport through the scale, oxygen consumption resulting in marked decrease in the partial pressure of oxygen at the scale-metal interface and leading to the thermodynamic stability of chromium subnitride. The dynamic cracking and healing can provide a fast nitrogen supply through the scale via the molecular gas transport process. Due to the fast kinetics of the process, it can be expected that some nitrogen molecules trapped in the grain boundaries and do not proceed to the next neighboring micro-crack until the next micro-crack appears in the adjacent boundary. This can lead to local observations of nitrogen at grain boundaries similar to what was observed in the atom probe measurements for carbon atoms [141,142].

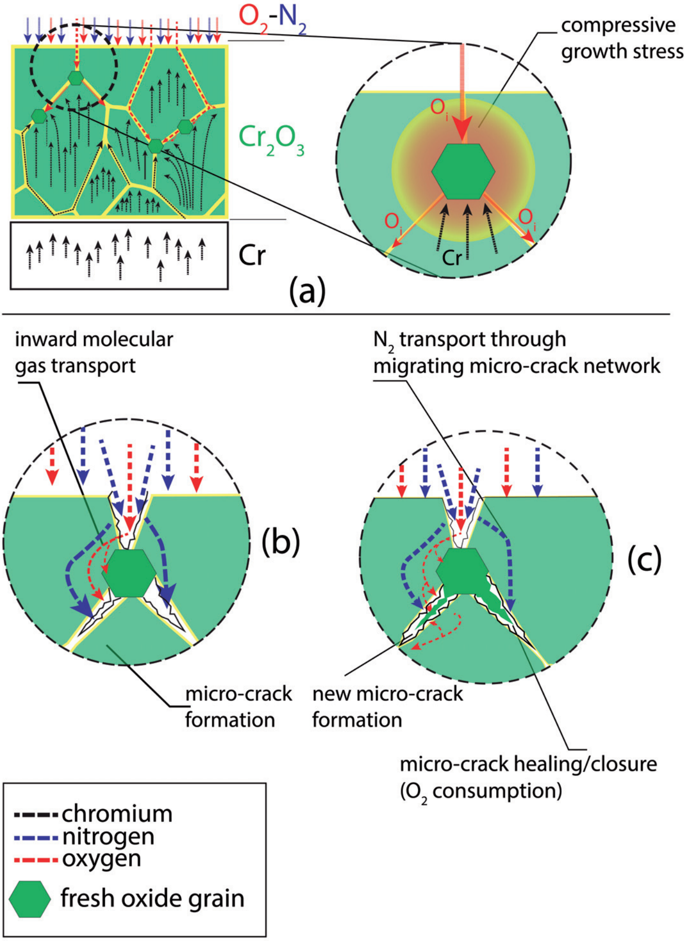

Figure 6-3. Schematic illustration of the molecular nitrogen transport via a dynamic micro-crack formation-healing process. (a) fresh oxide formation inside the scale, (b) development of growth stresses, (c) micro-crack formation and molecular gas transport, (d) cracking-healing-cracking (oxygen consumption) and molecular nitrogen transport.

Kinetics and thermodynamic approaches can be taken to mitigate nitridation in pure Cr via additions of alloying elements. As for kinetics, the diffusion of nitrogen can be controlled by alloying elements. In two phase alloys, this can be offered by a second phase with a low nitrogen permeability which can act as a barrier against nitridation. Alloying of an element can also promote a second oxide layer which is more protective and stable than chromia at high temperatures.

Thermodynamically, the addition of an alloying element can lead to the stabilization of an alloy in nitrogen containing atmospheres by shifting the nitride stability zone towards higher partial pressures of nitrogen preferably above atmospheric pressure. Similarly, a second phase with higher nitrogen stability can form via alloying which enhances the nitridation resistance of the alloy.

The oxidation behavior resulting from alloying will be discussed for the Cr-Si and the Cr-Ge-Si systems in the following.

6.2 Oxidation behavior in Cr-Si binary alloys

The binary Cr-Si system in the chromium rich section (Cr > 75 at.%) contains three phase fields starting with (from the lowest Si content) solid-solution Cr (S3), two phase Cr_{ss}-Cr_3Si (hypo-/hyper-) eutectic (S16, S19), and single phase A15 silicide phase (S25). The high temperature oxidation behavior of alloys in the Cr-Si system differs based on the composition and individual phases in the microstructure. The oxidation behavior of multiphase alloys is in many aspects different from single phase alloys and mostly more complicated. These differences mainly arise from the diffusion behavior of alloy components and the thermodynamic stability of individual phases during oxide growth [129]. Gesmundo et al. intensively investigated the mechanism and modes of oxidation of two-phase alloys in single oxidant atmospheres (O_2) [129,147]. It is generally agreed that the oxidation mechanisms of different multiphase alloys are not similar. Thus, understanding the mechanism of oxidation in two-phase Cr-Cr_3Si alloys requires multilateral investigations. In order to show the role of each individual phase during oxidation single phase alloys representing each constituent phase of the two-phase alloy should be first separately investigated. Until recently, there has been only a limited number of studies devoted to this approach for two-phase alloys [13]. In this work, the alloys S3 and S25 representing Cr_{ss} and the A15 silicide phase in the two-phase Cr-Cr_3Si alloys were studied and their kinetics and thermodynamics of oxidation and nitridation were investigated individually and in combination (two-phase alloy).

6.2.1 Single phase solid-solution alloy (S3)

Thermogravimetric data showed that the kinetic parameters of Cr-Si alloys (i.e. k_p and k_v) are significantly reduced by the addition of 3 at.% Si to chromium in single phase solid-solution (Figure 5-13). The achievement of a protective SiO_2 layer as a result of Si alloying is possible when the Si content in a single phase alloy lies above the critical concentration of Si ($N_{c,Si}$). This value can be obtained from the solution of general equation for diffusion and can be expressed by Wagner's expression (Eq. 19) [145,148,149].

$$N_{c,Si} = \left(\frac{\pi k_i}{2D}\right)^{1/2} \tag{19}$$

with

$$k_i = \left(\frac{2V_A}{\mu\, M_{O_2}}\right)^2 k_p \tag{20}$$

where V_A is the molar volume of the alloy, μ is the ratio of oxygen anions to metal cations in the oxide (for SiO_2, $\mu = 2$), D is the inter-diffusion coefficient, and M_{O_2} is the molecular mass of oxygen. Eq. 19 indicates that the ratio k_i/D is characteristic for an alloy to form a protective scale. The $N_{c,Si}$ value could be even higher than what Eq. 19 predicts when a less protective outer scale (here chromia) is initially formed [150]. Although the value of critical Si concentration cannot be calculated (due to the unknown diffusion coefficients), the broad range of internal oxidation in Figure 5-16c-d composed of SiO_2 internal precipitates indicates that the concentration of Si was not sufficient to form a continuous SiO_2 layer.

SEM results on the isothermally oxidized alloy S3, however, clearly show that the crystalline SiO_2 particles are locally formed at the metal-scale interface, mainly at the grain boundaries (see Figure 5-28a). The partial coverage of the metal-oxide interface with SiO_2 particle reduces the available surface area for Cr outward diffusion leading to reduced oxidation kinetics. On the other hand, it is known that a significant part of the apparent chromium diffusion during oxidation is supplied from grain boundaries [44]. Thus, formation of SiO_2 particles at grain boundaries can block the major chromium outward diffusion path and reduce the oxidation rate. This hypothesis is in good agreement with findings of Bamba et al. who reported the beneficial influence of local SiO_2 formation for Fe-Cr alloys [151].

Doping of Si in chromia scales can also be considered in correlation with the oxidation kinetics, as EDS results indicated that traces of Si exist in the chromia scale formed on alloy S3 (see Table 9). The solubility of Si in chromia can change the defect structure in chromia by annihilating interstitial Cr defects ($Cr_i^{\cdots}$) via the following reaction:

$$3SiO_2 + Cr_i^{\cdots} \xrightarrow{Cr_2O_3} 3Si_{Cr}^{\cdot} + Cr_{Cr}^{X} + 6O_O^{X} \tag{21}$$

which in turn can reduce the rate of oxidation [152]. The extremely reduced internal nitridation for alloy S3 should be taken as a key factor for the significantly lower mass gain during oxidation (Figure 5-13).

6.2.2 Single phase A15 silicide alloy (S25)

The single phase A15 Cr_3Si silicide alloy (S25) showed the highest oxidation resistance amongst the investigated Cr-Si binary alloys (Figure 5-13). The activity profile in this composition range (23-25 at.%) shows that the activity of Si is raised close to that of chromium. In accordance with the higher thermodynamic stability, multiple signs of formation of external SiO_2 were clearly observed. X-ray diffraction results showed that the scale contains crystalline SiO_2 (Figure 5-27). SEM/EDS observations showed higher (but not continuous) coverage of SiO_2 compared to that of alloy S3 after 100h isothermal exposure. However, after 100h oxidation, chromium oxide was still the major oxidation product in alloy S25 (Figure 5-28c). At this point, the reduced oxidation kinetics of single phase A15 alloy 25 can be attributed to the higher partial coverage of SiO_2 leading to less Cr-consumption at the alloy-scale interface and in turn, less outward Cr-transport. It is noteworthy that the k_i/D ratio in the A15 single phase is different from that of the Cr solid-solution phase. The diffusion behavior in the intermetallic A15 phase significantly differs from that of the single phase solid-solution alloy. During the first 100h of oxidation, chromium was the major diffusing element and the outward Cr transport in the A15 substrate resulted in Cr depletion at the subsurface region which in turn, changes the composition at this zone to the stoichiometric Cr_5Si_3 silicide at the alloy-oxide interface (see Figure 5-16e).

Surprisingly, after 1000h discontinuous isothermal exposure, alloy S25 formed a continuous Si-rich oxide layer beneath the chromia scale (see Figure 5-16j and Figure 5-29d). This layer with a full coverage of the surface is well adherent to the surface and the outer chromia layer (see Figure 42d). Indeed, the exceptional long term oxidation resistance of the single phase silicide alloy (S25) can be attributed, to a large extent, to the formation of this Si-rich oxide layer.

Cross section microscopy and EPMA maps of alloy S25 after 100h and 1000h oxidation shown in section 5.4.2 revealed the mechanism which leads to the evolution of oxide scales at long exposure times. In fact, the evolution of scale composition with time is induced by the alteration of the diffusion behavior in the subscale zone which is governed by microstructural evolution.

The physical metallurgy behind this microstructural development can be explained by the defect structure and diffusion behavior of the A and B elements in A_3B silicide. Calculations and experimental studies on the diffusion behavior of A and B elements in several A15 structures (Nb_3Sn, V_3Si, V_3Ga ….) all agreed that the B element (i.e. Sn, Si, and Ga) diffusion rate is negligible and in some cases not even measurable. As extensively discussed in the literature [153-155], this behavior can be explained by consideration of the A15 structure. The A15 structure has two types of sublattices for A and B elements. In a perfect crystal each A atom has a coordination number of 14 consisting of 10 A atoms and 4 B atoms while the atom B is surrounded by 12 A atoms (Figure 6-5). This clearly shows that while element A can easily diffuse through its sublattice by hopping to its neighboring vacancy or anti-site defect in sublattice B, diffusion of element B exclusively requires anti-site defects in sublattice A since atom B needs to jump over its neighboring position and move to the next B site in its own sublattice.

Considering the A15 crystal structure of Cr_3Si, it can be concluded that during oxidation at high temperatures, A15 Cr_3Si primarily supplies chromium to the surface. It should be noted however, that although Si is not as mobile as Cr, it can still be oxidized close to the surface without requiring a significant diffusion rate as SiO_2 formation is thermodynamically more favorable than Cr_2O_3 [14].

Selective outward diffusion of Cr again results in extensive depletion of chromium below the scale and further enrichment of silicon, which can even stabilize the D8m Cr_5Si_3 of composition 63 at.% Cr and 37 at.% Si (see Figure 2-8a and Figure 6-6).

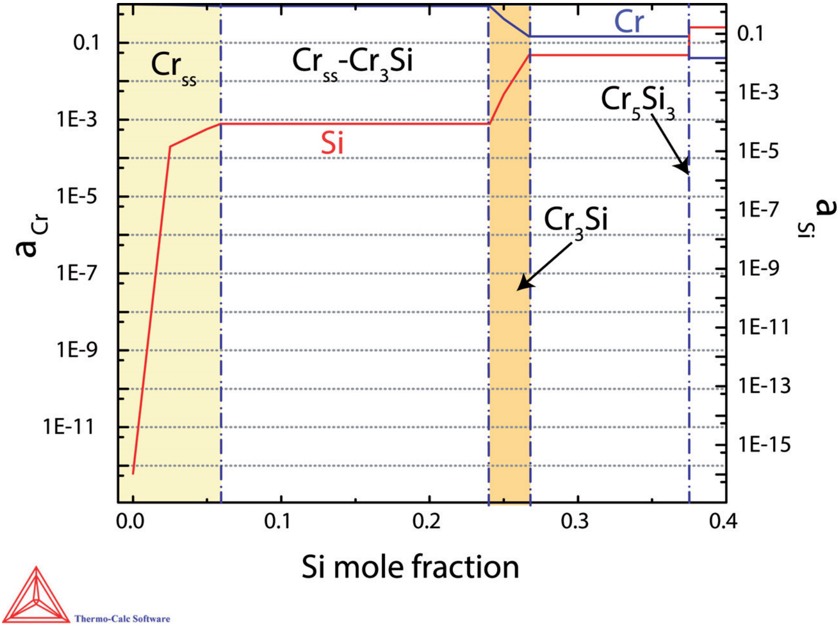

Figure 6-4. Activity profiles of Cr and Si in the Cr-Si binary system at 1200°C [156].

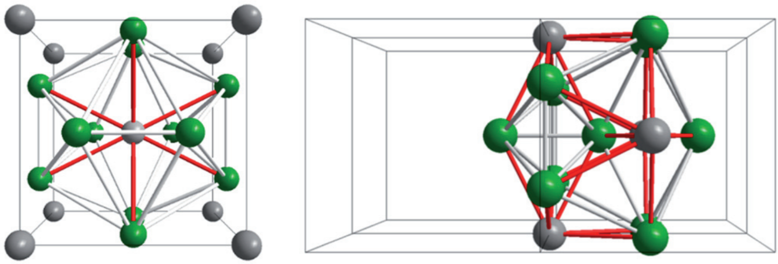

Figure 6-5. The coordination and bonding structure of Si (left, a-direction) and Cr (right, b-direction) in the A15 Cr_3Si unit cell. Cr is in green and Si is in grey. Cr-Cr bond (white), Cr-Si bond (red).

D8m Cr_5Si_3 silicide exhibits a different diffusion behavior than the A15 phase. According to diffusion studies on different X_5Si_3 refractory silicides (X= Nb, Mo,V and W), it was found that in this intermetallic structure Si is the predominant diffusing species [154,155]. The ratio of the diffusion coefficient of Si to the refractory element in this phase was found to be 31 and 103 for Nb_5Si_3 and Mo_5Si_3, respectively [157,158]. Although such data are not found for Cr_5Si_3, the observation of Si depletion at the subscale diffusion zone proves the predominant outward diffusion of Si from the initially formed Cr_5Si_3 layer during isothermal exposure (see Figure 6-6). Additionally, the activity of Si in this phase suddenly rises to a level above the activity of Cr which facilitates formation of SiO_2 (see Figure 6-4). At this point, the depletion of Si again results in a stabilization of the second A15 layer between the substrate surface and the earlier formed Cr_5Si_3 diffusion layer and the formation of Si-rich oxide and oxy-nitride at the metal surface (see Figure 5-16j and Figure 6-6). Thus, the formation of a continuous protective Si-rich oxide layer in the A15 alloy S25 arises from the sudden increase of the diffusion rate of Si in the Cr_5Si_3 phase formed during oxidation.

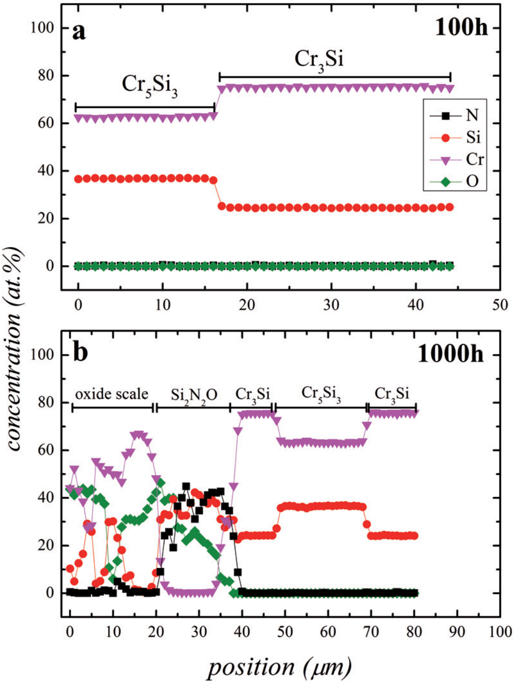

Figure 6-6. Cross sectional quantitative EPMA analysis of single phase Cr_3Si alloy oxidized at 1200°C in synthetic air after a) 100h (Figure 5-16e) b) 1000h (Figure 5-16j).

6.2.3 Two-phase Cr-Cr_3Si alloys

The oxidation behavior of alloys representing Cr_{ss} and the A15 silicide phase was discussed in the previous section. It was revealed that at least for the first 100h, oxidation in both alloys is governed by primary outward diffusion of chromium. In the case of A15 silicide, evolution of the subscale microstructure resulted in primary

Si diffusion after a certain exposure time. It is also observed that the A15 silicide is the most oxidation resistant phase.

Thermogravimetric results indicated that the oxidation kinetics of eutectic (S16) and hyper-eutectic (S19) Cr-Cr_3Si alloys lie between the oxidation kinetics of alloys representing the individual phases (see Figure 5-13). Alloy S19 showed slower oxidation kinetics than alloy S16.

Oxidation of two-phase alloys is somewhat different from that of single phase alloys. Depending on whether the individual phases oxidize independently or cooperatively, oxidation products may change in composition and morphology [129,159,160]. From a thermodynamic point of view, it is important to note that regardless of differences in the chemical composition of individual phases, the chemical potential and therefore, the activity of Cr and Si in both solid-solution and A15 phase must be similar when they are in equilibrium with each other (see Figure 6-4). Nevertheless, deviation from equilibrium in real practice can occur due to the primary diffusion of one alloy component, which in turn, may cause disappearance of a phase in the oxidation-affected zone. In addition, significant differences in oxidation behavior of individual phases due to the different availability of the most protective scale forming alloy component can disturb the thermodynamic equilibrium condition [129]. Thus, formation of oxidation products and evolution of the subscale substrate may be different from what the equilibrium thermodynamics expects. Important factors in the two-phase alloys are the diffusivity and concentration of elements to enable protective scale formation. These factors depend on size, shape, crystal structure, volume fraction, and composition of the matrix phase [13]. Gesmundo et al. reviewed the modeled oxidation process for two-phase alloys utilizing a so called “reservoir effect”. This effect is observed in alloys in which the most protective oxide former alloy component is supplied through the second phase precipitation dissolution process (e.g. dissolution of $NbAl_3$ precipitates in the NiCrAl system). Figure 6-7 illustrates the mechanism schematically. They discussed that if the precipitation phase fraction is high enough, the dissolution process will be uniform with a planar front which is favored by lateral diffusion of alloy components in the region of transition between the single- and two-phase zones.

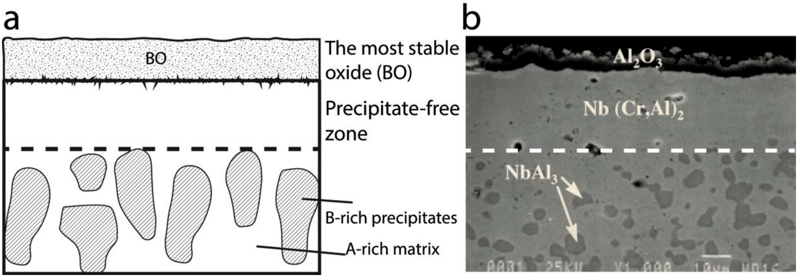

Figure 6-7. a) Schematic illustration of the two-phase alloys with solute-rich precipitates acting as a reservoir for the growth of a solute scale (BO), b) The precipitate dissolution effect during oxidation of Nb-49Al-20Cr-1W-0.1Y alloy after 100 one-hour cycles at 1200°C in air. After [13,161] (with kind permission from Springer Science and Business Media).

At the first glance, post-oxidation microstructure of the Cr-Cr_3Si eutectic alloy resembles those observed in a precipitation dissolution process discussed by Gesmundo and Gleeson et al. [13,129], where the precipitates were dissolved by outward diffusion of the more stable oxide forming alloy constituent (e.g. Cr in Fe-Cr alloys and Al in Nb-Al-Cr alloys). However, unlike the alloy systems described there (e.g. 25Cr-20Ni steel with Cr-rich $Cr_{23}C_6$ precipitates [162,163], or Nb-49Al-20Cr-1W-0.1Y with Al-rich $NbAl_3$ precipitates), alloy S16 shows Cr-rich phase (Cr_{ss}) dissolution instead of the Si-rich phase Cr_3Si (compare Figure 6-7 with Figure 5-16c).

It was shown in the previous section that the diffusivity of Cr in both Cr_{ss} and the A15 silicide phase is higher than that of Si. Furthermore, the activity of Cr in the two-phase alloy is higher than that of Si. Therefore, chromium is the primary oxidizing alloy component in the two-phase alloy. Thus, outward supply of chromium leads to depletion of chromium in the subscale zone. To maintain the two Cr_{ss} and Cr_3Si phases in equilibrium, the Cr-rich phase (Cr_{ss}) supplies more chromium and its Cr content decreases. This in turn, results in destabilization of the Cr_{ss} phase in the subscale region and formation of a Cr_{ss}-free zone i.e. a single phase A15 zone (see Figure 5-16c). This process is schematically illustrated in Figure 6-8. Such a dissolution process is governed by the lateral diffusion of alloy components at the transition zone between the single phase A15 layer and the two-phase Cr-Cr_3Si zone [129]. Increasing the oxidation time results in a wider Cr_{ss}-free zone (see Figure 5-16h). As a side effect of the outward Cr supply process, Kirkendall pores form in the Cr_{ss}-free zone (see Figure 5-16c). Interestingly, element distribution maps in Figure 5-16c,h indicate that these porosities are filled mostly with Cr_2O_3 which in turn, proves the predominant diffusivity of chromium although the formation of SiO_2 is thermodynamically favored.

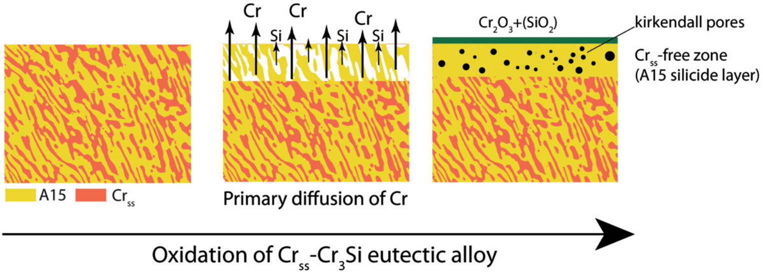

Figure 6-8. Schematic illustration of the oxidation mechanism in two-phase Cr-Cr_3Si alloys. Predominant Cr diffusion leads to the dissolution of the Cr_{ss} phase and formation of an A15 silicide layer.

It is important to note that besides the predominant Cr supply from the substrate, a minor diffusion of Si is enough to form SiO_2 underneath the chromia scale. X-ray diffraction data clearly showed formation of SiO_2 (Figure 5-27). In addition, higher coverage of SiO_2 compared to the single phase solid-solution alloy S3 is evident in Figure 5-28 which can be accounted for the reduced oxidation kinetics.

Increasing the Si content to 19 at.% (S19) leads to formation of primary Cr_3Si phase surrounded with a eutectic lamellar microstructure (Figure 5-4). Thus, based on the lever rule, alloy S19 has a higher A15 phase fraction compared to alloy S16 which in turn, gradually affects the mechanism of oxidation explained above. Although no diffusion data are available for this alloy system, it can be intuitively assumed that the Cr_{ss} dissolution process is slower when the phase fraction of Cr_{ss} is significantly reduced in the microstructure. Thus, the Cr supply for oxide formation can mainly be maintained by the A15 phase (see Figure 5-16d,i) which hinders the overall diffusion kinetics and in turn, slows down the oxidation rate (see Figure 5-13).

6.2.4 Nitridation of Cr-Si binary alloys

Schwerdtfeger described the thermodynamic equilibrium of the Cr-N system for the temperature range of 1100°C to 1310°C [88]

$$\log P_{N_2\,(\mathrm{atm})} = -\frac{11{,}080}{T} + 5.32 \qquad (22)$$

which equals $P(N_2) = 6.28\times 10^{-3}$ atm. at 1200°C in N_2-H_2 atmosphere. Thermodynamic calculations showed that this value can change when oxygen is added to nitrogen (see Figure 2-4b). The characterized reaction products are qualitatively in agreement with the thermodynamic equilibrium of the Cr-O-N system (Figure 2-4b). At the gas-oxide scale interface where the chromium concentration is lowest and the oxygen partial pressure is highest the most stable product is chromia (Cr_2O_3). Underneath the chromia scale, where the chromium concentration is highest and the oxygen partial pressure is low, a very low partial pressure of nitrogen is required to stabilize chromium nitride (Cr_2N) which can be formed at $P_{N_2} \geq 4.7 \times 10^{-2}$ atm and $P_{O_2} \leq 1.2 \times 10^{-18}$ atm. According to the phase stability diagram, Cr_2N is the only possible nitride which can exist at sub-atmospheric nitrogen pressures at 1200°C.

The effect of Si additions on the stability in the Cr-O-N system is shown in Figure 6-9 for Si mole fractions 0 < Si/(Si+Cr) < 0.25. The major differences with the addition of Si is the stability of the two-phase (Cr_{ss}+Cr_3Si) system at very low oxygen and nitrogen partial pressures, the stability of the secondary oxide SiO_2 below the chromium oxide and selective transformation of the Cr solid-solution phase to Cr_2N at $P_{N_2} \geq 5.4 \times 10^{-2}$atm and $P_{O_2} \leq 4.5 \times 10^{-19}$ atm.

Silicon generally enhanced the resistance to nitridation, and even the addition of 3 at.% Si improved the internal nitridation resistance of the solid-solution Cr(Si) alloy. Still intensive nitridation was observed after long term oxidation exposure, preferentially at the grain-boundaries (see Figure 5-16g). By adding 3 at.% silicon to chromium the predominant path of diffusion for nitrogen changes from lattice diffusion in the subscale nitride and chromium substrate to grain boundary diffusion of nitrogen (see Figure 5-16g).

Interestingly, the highest nitridation resistance in the Cr-Si-system was observed for the A15 silicide, owing to its high thermodynamic stability in the whole range of nitrogen partial pressures (see Figure 6-9). Additionally, the A15 crystal structure showed good diffusion barrier properties for nitrogen and interstitial elements [153]. The A15 structure has three tetrahedral interstices and four triangular base bipyramid interstices (see Figure 6-10). Only one tetrahedron and a single bipyramid position (the largest ones) are the preferential sites for interstitials (including nitrogen) according to ab-initio calculations by Sluiter et al. [153]. On the other hand, nitrogen cannot substitute Si or Cr considering its small atomic size compared to the two elements (N = 65 pm, Si = 117 pm and Cr = 140 pm). Thus, for diffusion within this structure, interstitial nitrogen needs to hop between no-adjacent tetrahedrons or bipyramids which demands high activation energy. This structural condition makes diffusion of nitrogen in A15 Cr_3Si more difficult than in bcc Cr(Si) [153] and can be the key explanation for nitrogen transport in the Cr_3Si silicide phase in comparison to the chromium solid-solution at high temperatures [81].

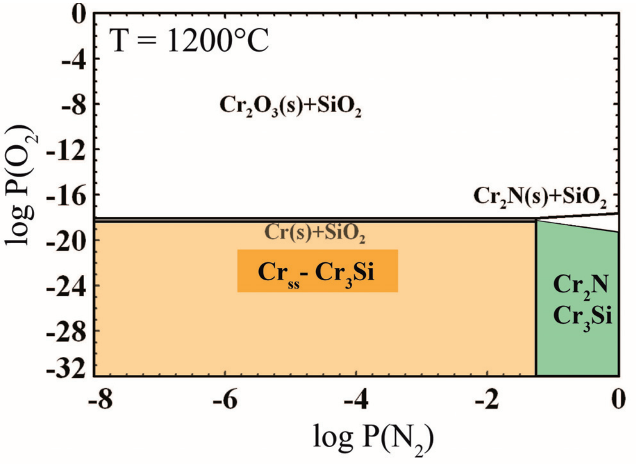

Figure 6-9. The stability diagram for the Cr-Si-O-N system at 1200°C. (FactSage).

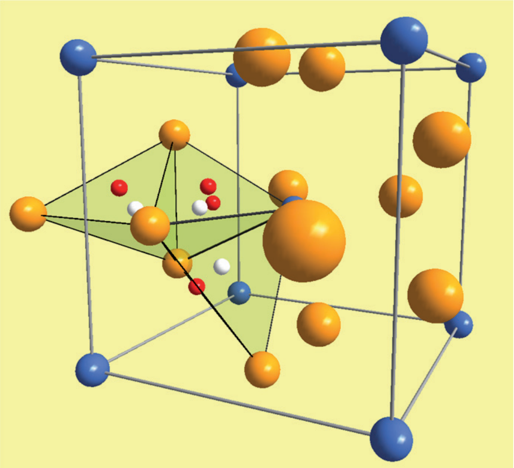

Figure 6-10. Interstitial sites in the A15 Cr_3Si structure: the white spheres are the tetrahedral interstices and the red spheres are the four triangular base bipyramid interstices (after Sluiter et al. [153]).

The sequence of oxidation products observed in the EPMA analyses (Figure 5-16e,j) are in accordance with the thermodynamic equilibrium of the Cr-Si-O-N system (Figure 6-9).

6.2.4.1 Microstructural correlation with internal nitridation

Cross section analysis of the oxidized two-phase alloys in synthetic air and in N_2-5%H_2 atmosphere confirms the different nitridation behavior of the individual phases. The nitrided microstructures of the two-phase alloys in Figure 5-16 and Figure 5-17 indicate that the solid-solution phase is selectively nitrided while the A15 silicide phase remains immune to nitridation. This is in agreement with the thermodynamic prediction discussed in the previous section. The inward diffusion of nitrogen through the Cr_{ss} lamellae has to be the mechanism of nitridation in the two-phase Cr_{ss}-Cr_3Si alloys.

It is important to note that although the A15 phase shows protective character against nitridation, the morphology of the individual phases in the microstructure determines to a high extent the nitridation behavior of the alloys. Comparing the cross sections of Cr-Cr_3Si eutectic alloy (S16) exposed in N_2-5%H_2 and in synthetic air (see Figure 5-17), it is noticed that in the absence of oxygen, the A15 layer (resulting from the dissolution of the Cr_{ss} phase) does not form which in turn caused severe selective nitridation of the Cr_{ss} lamellae (up to 250 µm deep after 50h). As the Cr_{ss} phase has an interconnected network in the eutectic microstructure, inward growth of nitride can easily advance throughout the substrate without being hindered by a barrier. The severe internal nitridation is obvious in the thermogravimetric curves as a significant mass change e.g. when alloy S16 is exposed to synthetic air and N_2-5H_2 atmospheres (see Figure 5-14). Oxidation of the Cr-Cr_3Si eutectic alloy (S16) in synthetic air offers a self-protecting character via formation of the A15 phase layer at the subsurface region which protects the underlying substrate from nitridation (Figure 6-8). The extent of nitridation attack cannot be directly related to the Si content of the two-phase alloy, rather to the microstructural morphology and the orientation of the A15 phase, as alloy S19 showed a higher extent of nitridation compared to alloy S16 (see Figure 5-16d and i). This is due to the original microstructure of alloy S19 composed of primary A15 dendrites surrounded by inter-dendritic eutectic structures. In this case, the inter-connected network of Cr_{ss} lamellae leads to intensive inter-dendritic nitridation. Therefore, unlike oxidation, the extent of nitridation cannot be directly related to the Si content, rather to the microstructural morphology and the orientation of the nitridation resistant phase i.e the A15 silicide.

The self-protecting character discussed above has not yet been observed in other classes of Cr-alloys. Brady et al. compared the nitridation behavior of Cr-Cr_2Nb and Cr-Cr_2Ta alloys [12]. Severe nitridation of both alloys was observed when oxidized in air at 1100°C. The extent of nitridation in Cr-Cr_2Nb was significantly higher than that of Cr-Cr_2Ta alloys. They reported that both Laves phases, Cr_2Nb and Cr_2Ta, were selectively nitrided within the composition ranges of (40–50)Cr–(20–25)Nb-(25–35)N and 40Cr-20Ta-40N [123]. Recently, Bhowmik and coworkers reported similar degrees of nitridation in both, solid-solution and laves phase, in Cr-Cr_2Ta during high temperature oxidation in air [124]. They also reported a high degree of oxygen solubility (up to 7.7 at.% O) in both nitrided phases and showed that additions of Si to Cr-Cr_2Ta can significantly reduce nitridation. The underlying mechanism explaining why Si has such beneficial effects on subscale nitridation was not reported there, however.

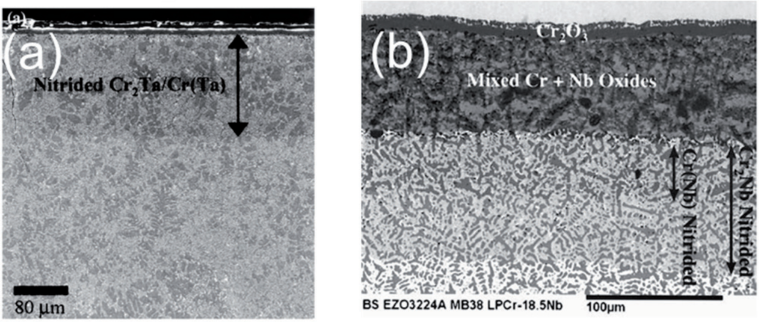

Figure 6-11. Nitridation of a) Cr-Cr_2Ta and b) Cr-Cr_2Nb in air after 24h isothermal exposure at 1100°C in air [12,164] (with kind permission from Springer Science and Business Media and Taylor & Francis Group).

The present findings for the Cr-Cr_3Si system are very promising, especially in comparison with the results on binary Cr-Laves phase alloys (Cr-Cr_2X(X=Ta, Nb) in which the intermetallic laves phase is even more prone to oxidation and nitridation than the chromium matrix (Figure 6-11) [12,123].

At long term exposure, the A15 layer is damaged through large amounts of Kirkendall pores which in turn offer a pathway to nitrogen. This leads to a loss of the protective character of the A15 layer and further internal nitridation of the chromium solid-solution phase (see Figure 5-16h). In sections 6.3 and 6.4, it will be shown that Ge-addition can help to maintain the self-protecting character of the Cr-Cr_3Si eutectic alloy during long term oxidation.

6.3 Phase equilibrium in the Cr-Ge-Si system

6.3.1 Microstructural evolution

Substitution of Si by Ge in the Cr-Cr_3Si eutectic alloy altered the microstructure of the resulting ternary alloys. As Figure 5-5 shows, the extent of microstructural changes depends on Ge/Si ratio. Figure 5-5b shows that there is a transition point where the micro structure changes from a fine eutectic lamellar structure to a coarse dendritic microstructure. Although the exact quantitative transient composition cannot be found, Figure 5-5 illustrates that alloys with a Ge/Si ratio higher than 0.125 do not show a fine microstructure anymore but rather show a coarser microstructure with dendritic primary Cr_{ss} phases. This is indeed an important point in terms of alloy design for high temperature applications. It is required to have a fine homogenous microstructure which ensures the mechanical stability at high temperatures [2,119].

Considering the nature of the peritectic transformation in the Cr-Ge binary system [27], it can be assumed that additions of Ge change the simultaneous growth of the A15 and Cr_{ss} phase in eutectic solidification in a way that first, the primary Cr_{ss} dendrite forms and then the A15 phase results from the reaction between primary Cr_{ss} and the liquid phase. The A15 phase surrounds the primary Cr_{ss} dendrites and hinders the diffusion during the growth process which in turn, alters the microstructure from a fine lamellar one to a coarse peritectic one (depending on Ge contents) [165]. Strong evidence for such an effect is the significant coring effect (segregation) in the A15 phase formed during casting of ternary alloys (see Figure 5-5) which is typically caused by the complexities of the peritectic reaction [166].

After annealing at high temperatures, a common feature of the ternary alloys with coarse microstructure SG4, SG8, and SG 12 is that they show precipitates of the A15 phase within the Cr_{ss} phase (see Figure 5-6). These precipitates are formed as a result of the diffusion of the solutes (Si and Ge) which are supersaturated in the Cr_{ss} phase during casting. During annealing at 1350°C, the supersaturated solid-solution chromium (Cr_{sss}) undergoes the following transformation resulting in Cr_{ss} with A15 precipitates in equilibrium [167].

$$Cr_{sss} \xrightarrow{1350℃,100h} Cr_{ss}^{eq} + Cr_3(Si,Ge) \qquad (23)$$

It has to be noted that the precipitates within the Cr_{ss} are mostly observed in ternary alloys with co-addition of Si and Ge. As Figure 5-6 shows, an increasing Ge/Si ratio results in more precipitates. Such precipitates are not observed in Cr_{ss} dendrites in the peritectic microstructure of the Cr-Ge binary alloy (G16). An increase of the A15 phase fraction with increasing Ge/Si ratio in the ternary alloys (Figure 5-8) can be in one part attributed to the peritectic reaction which promotes the A15 phase formation and in another part be correlated to the A15 precipitates formed in the Cr_{ss} primary dendrites during annealing.

6.3.2 Partitioning of Si and Ge in constituent phases of ternary Cr-Ge-Si alloys

Figure 5-9 illustrates the partitioning of Si and Ge in each individual phase (Figure 5-9a,c). It is evident that Si and Ge show mutual solubility in both Cr_{ss} and A15 phases for the whole Ge/Si range which shows a complete substitution of Si by Ge in both phases within the whole composition range. It is important to note that although the mutual substitution of Si and Ge is evident, the solubility limit of each phase shows different dependence on the Ge/Si ratio. The fact that the solubility limit of the Cr solid-solution phase increases with the Ge/Si ratio while that of the A15 phase decreases is somewhat surprising because both phases show higher solubility ranges in the binary Cr-Si system compared to the Cr-Ge system [26,27].

6.3.3 Crystallography of the ternary Cr_{ss}-A15 alloys

The fact that substitution of Si by Ge does not introduce an additional phase to the Cr-A15 silicide alloys within the composition range of the two-phase Cr-Cr_3(Si,Ge) zone is proven by X-ray diffraction analysis (Figure 5-10) which is a rare character for ternary two-phase alloys and is not observed in any other analogous A15 phase that forms within ternary systems such as Cr-Ru-Pt. Here a discontinuity is observed between the Cr_3Ru and Cr_3Pt phase fields at the high-chromium end of the ternary system at 1000°C [168].

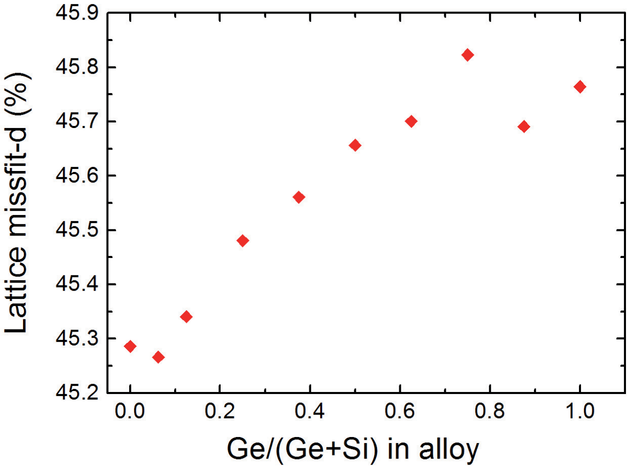

Figure 6-12. Dependence of lattice misfit between Cr_{ss} and A15 phase in two-phase ternary Cr-Ge-Si alloys.

The influence of Si substitution by Ge on the crystal structure of each constituent phase can be observed in the variation of lattice constants. Figure 5-11 illustrates that the lattice constant of both bcc solid-solution and A15 intermetallic structure increases linearly with increasing Ge/Si ratio following the Vegard's law. The increase of the lattice constant is not surprising when the atomic size of Si (117.6 pm) and Ge (125 pm) are considered. However, it is important to note that the influence of Ge on the lattice constant of the A15 phase is significantly higher (by a factor of 2.7) than that on the Cr-solid-solution phase. The lattice misfit (δ) between Cr_{ss} and A15 phase for each Ge/Si ratio is illustrated in Figure 6-12 using equation 30.

$$\delta = \frac{2(a_{[Crss]} - a_{[A15]})}{(a_{[Crss]} + a_{[A15]})} \tag{24}$$

The lattice misfit of 45-46% categorizes the interface between the A15 and the solid-solution phase as "incoherent".

6.4 Oxidation behavior of Ge-alloyed Cr-Cr_3Si alloys

The gravimetric results at 1350°C (Figure 5-18) and at 1200°C (Figure 5-20) indicated that the paralinear oxidation kinetics (Eq. 14) discussed in section 6.1 and 6.2 can successfully represent the kinetics of oxidation for ternary Cr-Ge-Si alloys with highly accurate fits. It has to be noted that, although volatilization of Cr is a well-known effect at high temperatures, the negative term regarding this step is still missing in many investigations of oxidation kinetics on Cr-based alloys [40,124,169].

It is clearly seen that up to 2 at.% Ge alloying can increase the oxidation resistance as the parabolic rate is decreased at both 1200°C and 1350°C (Figure 5-19 and Figure 5-20b). Germanium enrichment is observed in both the SiO_2 and the Cr_2O_3 scales of the isothermally oxidized alloy SG1 (see Table 5-6 and Figure 5-26). The higher Ge content observed in SiO_2 (1.05 at.%) proves its dissolution in SiO_2, as SiO_2 and GeO_2 both have the same crystallographic structure and show mutual solubility in both amorphous and crystalline form, according to their phase diagram (see Figure 6-13). The beneficial influence of Ge on the oxidation resistance of silicide containing alloys and coatings was first reported by Rapp et al. [24,170-172] followed by Brady et al. [173]. It is reported that Ge can increase the coefficient of thermal expansion (CTE) of the amorphous SiO_2 significantly which in turn, improves adhesion of the SiO_2 layer. In this work formation of crystalline SiO_2 was evident (see Figure 5-27). The influence of Ge on the CTE of crystalline SiO_2 was studied by Schlichting [174] and Bachmann et al. [175], where a significant increase (by up to a factor of two at 800°C) is reported for the CTE of the GeO_2 doped silica. Thus, it is safe to generally say that in amorphous as well as crystalline SiO_2, Ge can increase the CTE of silica. On the other hand, Schlichting reported that Ge has an impact on crystallinity of SiO_2 by stabilizing the amorphous phase and reducing the viscosity of oxide [176]. He showed enhanced oxidation behavior in the range of 600-1400°C in Si-based ceramics such as $MoSi_2$, Si_3N_4 etc as a result of GeO_2 doping. Similar impacts, at least in part, play a role in the enhanced oxidation of Ge-containing alloy via enhanced adhesion of the scale to the substrate, as reported by others [24,171,173].

Minor traces of Ge are observed in the chromia scale (see Table 5-6). The Ge-doped chromia scale may show different growth behavior compared to the un-doped one. To the best of the author's knowledge no phase diagram and solubility information exists for GeO_2 and Cr_2O_3. However, assuming that GeO_2 is similar to SiO_2, formation of a mixed oxide is ruled out. Therefore, the influence of Ge on chromia growth kinetics may be a doping effect that affects the diffusion process within the scale [177]. This possible effect must be studied via tracer diffusion similar to what was conducted by Tsai et al. [178-180]

It is important to note that substitution of 4 to 12 at.% Si by Ge negatively affected the oxidation resistance by increasing both growth and volatilization rate (Figure 5-19). Considering the significantly reduced Si content in this alloy, it is not surprising to have a higher growth rate (k_p). On the other hand, the increase of the k_v values for alloy SG12 at 1350°C (Figure 5-18 and Figure 5-19) and alloy SG1 and SG2 at 1200°C indicates that Ge addition plays a role in increasing the volatilization rate. The quantitative ratio of stable oxide species for oxidation of the two-phase alloys at 1350°C (see Table 6-2) shows that in all Ge-containing alloys GeO_2 is a thermodynamically stable oxide under oxidizing conditions. GeO_2 with a melting point of about 1100°C is volatile at 1350°C at similar partial pressures as the volatile CrO_3 [14] which explains the increased volatilization observed in alloy SG12. The SiO_2-GeO_2 phase diagram (Figure 6-13) indicates that Ge should form a mixed oxide with SiO_2 as they show solid solubility at low GeO_2 contents and liquid phase solubility at high GeO_2 ratios. It can be clearly seen here, that substitution of Si by Ge leads to a higher GeO_2 /SiO_2 ratio (e.g. for alloy SG12, GeO_2/SiO_2 = 19.6/7) which supports the volatilization behavior discussed above.

Table 6-2. Calculated thermodynamically stable compounds at oxide/gas interface.

alloys/oxides (mole%)	*S16*	*SG1*	*SG2*	*SG12*
Cr_2O_3	72.4	73.3	73.4	73.4
SiO_2	27.6	26.2	24.5	7
GeO_2	0	0.5	2.1	19.6

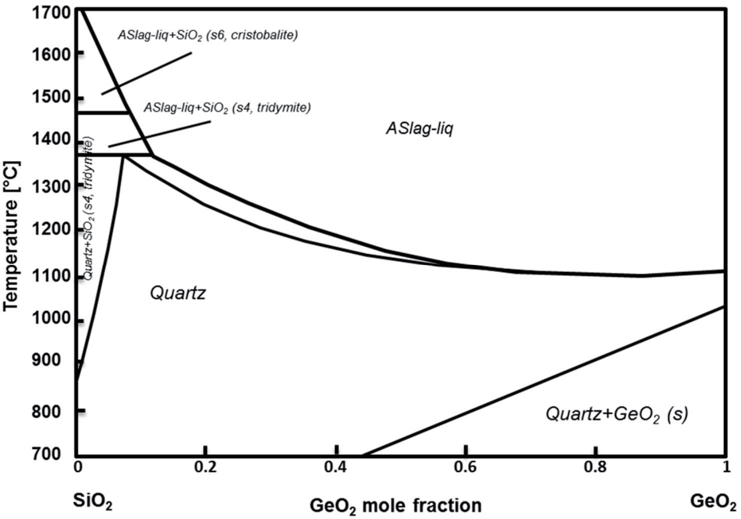

Figure 6-13. SiO2-GeO2 binary phase diagram (from FT oxide, FactSage SGTE database).

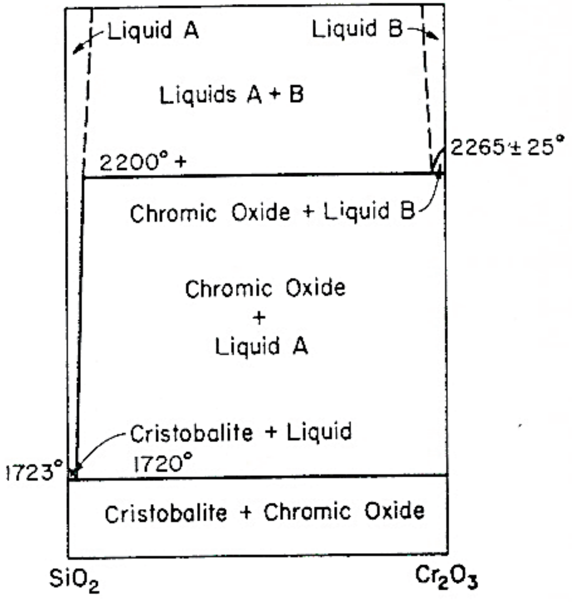

Figure 6-14. The Cr2O3-SiO2 system, adopted from [181].

6.4.1 The influence of Ge on internal nitridation of Cr-Cr_3Si alloys

Significant resistance against internal nitridation of the Ge-alloyed two-phase alloys is evident after short term and long term isothermal exposures. The role of the A15 phase in the subsurface region is discussed in depth in section 6.3. The barrier character and the thermodynamic stability of the A15 layer against diffusion of interstitial elements such as nitrogen offer significant protection against internal nitridation. During long term oxidation, however, defects form within this layer allowing nitrogen to penetrate to the substrate microstructure which leads to selective nitridation of Cr_{ss}.

The microstructural investigations, phase identifications, and solubility determination of the Cr-Ge-Si ternary system showed that up to 2 at.% Ge can be added to the two-phase Cr-Cr_3Si eutectic alloy without losing the fine microstructure. The post oxidation investigation of alloys SG1 and SG2 after short term (50h) and long term (1000h) oxidation at 1200°C (Figure 5-22) showed some similarities and some differences from that of eutectic alloy S16. The highest nitridation resistance is observed for alloy SG2. The subsurface A15 layer in this alloy seems to act protective even for long term oxidation exposures. The alloy shows not only a fine structure, but also a nitride free one and is a significant improvement compared to the oxidation performance of other chromium-intermetallic based alloys which nitride much faster even at lower temperatures (see Figure 6-11) [12,164]. To understand the mechanism behind the protective behavior of alloy SG2, quantitative line scans have been analyzed (Figure 5-23). It is evident that after 1000h alloy SG2 forms a subsurface A15 layer with a thickness half of that of alloy S16. Considering the mechanism of oxidation for two-phase alloys discussed in 6.2.3, the thinner A15 layer in alloy SG2 can be attributed to the lower rate of outward diffusion of Cr as the faster diffusing element in the systems. This in turn, reduces the dissolution rate of the Cr_{ss} phase that leads to thinner A15 layer formation. It must be noted that the Kirkendall pores (filled with internal oxides) are side effects of the outward diffusion of chromium. Therefore, less porosity throughout the A15 layer in alloy SG2 (Figure 5-22c-d) compared to that observed in alloy S16 implies a slower chromium diffusion rate.

The fact that a gradual chromium gradient exists throughout the A15 layer formed on both alloy S16 and SG2 can be attributed to the equilibrium stability of the phase during the dissolution process. The quantitative composition data showed that the composition at the inner side of this layer in contact with the two-phase substrate is 77.4 at% for both alloys which is in agreement with the reported value for the equilibrium composition of the A15 phase.

It is important to note that the gradient of Si within the A15 layer is significantly higher in alloy SG2 and does not correlate with the chromium gradient (as observed for alloy S16) (see Figure 5-23). The accumulation of Ge at the outer surface of the alloy is evident. As the Cr gradient does not change, Ge enrichment is only possible through substitution of Si in the alloy. Therefore, in ternary Cr-Ge-Si alloys Si and Ge show a correlative chemical gradient. It is not clear if Ge enrichment in the A15 phase would also decrease the diffusion of interstitials. This would require an in depth theoretical calculation similar to the work of Sluiter et al. [153]. The quantitative EPMA result showed negligible solubility of nitrogen in the A15 silicide phase (0.1 at.%) which indirectly shows the barrier character of the A15 phase for nitrogen diffusion (see Table 5-5). Further evidences of suppressed nitrogen access can be seen in the nitrogen map in Figure 5-22d and in Figure 5-23b showing no signs of the nitrogen signal in the solid-solution phase.

6.5 Structure, morphology, and adhesion of the protective scale

6.5.1 Crystal structure of oxide scales

It is evident from x-ray powder diffraction analysis that oxide scales formed on both binary Cr-Si and ternary Cr-Ge-Si alloys are mainly composed of chromia with eskolaite structure, and some SiO_2 with cristobalite structure (see Figure 5-27). It seems that there is a preferred orientation of cristobalite since only one reflection at $2\Theta\approx10°$ is visible which corresponds to the (111) reflection of the alpha-cristobalite phase. The needle-like shape of the cristobalite grains (Figure 5-28) is reflected by a preferred orientation in the XRD experiment, where the needle's long axes are aligned along the scattering direction in transmission geometry. Therefore, only one peak can be detected in the XRD pattern. Formation of cristobalite at 1200°C is in agreement with the previous study by Evans et al. in which the cristobalite phase was formed at temperatures between 1200 and 1400°C [182]. The fact that Ge is doped in the SiO_2 crystal or forms a mixed oxide (as discussed in section 6.4) cannot be studied using the conventional x-ray diffraction methods, as GeO_2 and SiO_2 in amorphous and crystalline form are of similar pattern. Therefore, high-resolution x-ray diffraction, and other characterization techniques are required to see the influence of Ge [183]. Nevertheless, EDS-analysis of the bottom side of the oxide scale representing the metal-oxide interface, where the most stable oxide forms (i.e. SiO_2), reveals up to 0.14 at.% of Ge in the oxide (see Figure 5-26). This supports the existence of Ge doped into the scale. Since pure GeO_2 is gaseous in the applied temperature range, a mixed oxide $(Si,Ge)O_2$ is most likely as discussed in section 6.4 [183,184].

6.5.2 Scale morphology

Despite the importance, only a few studies have focused on the morphology of oxide scales [52,53,56,185]. The chromia scale growth is associated with development of compressive stresses in the scale due to the formation of new oxides inside the scale [45,77,143]. However, the scale can only accommodate a certain amount of strain and higher growth stresses cannot be tolerated by creep deformation of the scale. They will be released by pseudo-plastic deformation which is based on a continuous microscopic defect formation and healing process in the scale [143,145]. In micro-scale, formation of micro-cracks can locally release a part of the growth stress (see section 6.1). However, the superimposed healing process can bring a part of the growth stress back to the scale. When the overall growth stress in the scale exceeds a critical value, the physical contact will be lost by local detachment (disbonding) of scale from the substrate surface leading to a wavy morphology known as "oxide buckling, -wrinkling, or –blistering". Figure 6-15a-b illustrates the mechanism of scale wrinkling schematically. The observation of scale wrinkling for pure Cr and chromium alloys at 1200°C and 1050°C (see Figure 5-25 and Figure 5-26) is in agreement with those reported by Polman, Kofstad, and Hindam for pure chromium [44,53,77]. It should be noted that when the wrinkle is formed, a complex stress concentration will be formed at the boundary line (Figure 6-15b) which can lead to oxide failure and a subsequent molecular oxygen transport and healing process. However, a considerable amount of Cr metal is evaporated from the blank surface and is accumulated under the detached scale. Thus, as soon as the thermodynamically required oxygen partial pressure is provided, a rapid scaling can proceed on the blank metal surface. Besides, since volatile chromium Cr(g) exists under the detached surface, further oxide growth can proceed at the underside of the scale (see Figure 6-15c). This procedure has been observed on TG-curves as discontinuities in the form of stages with rapid and large mass changes (see Figure 5-1). The buckling has been characterized by acoustic emission (Figure 5-3) during isothermal oxidation and electron microscopy of the oxidized specimen after isothermal oxidation (Figure 5-25a). The columnar growth of chromia between the gaps indicates that the gap between the chromia layers was formed at temperature and not during cooling (Figure 5-25a).

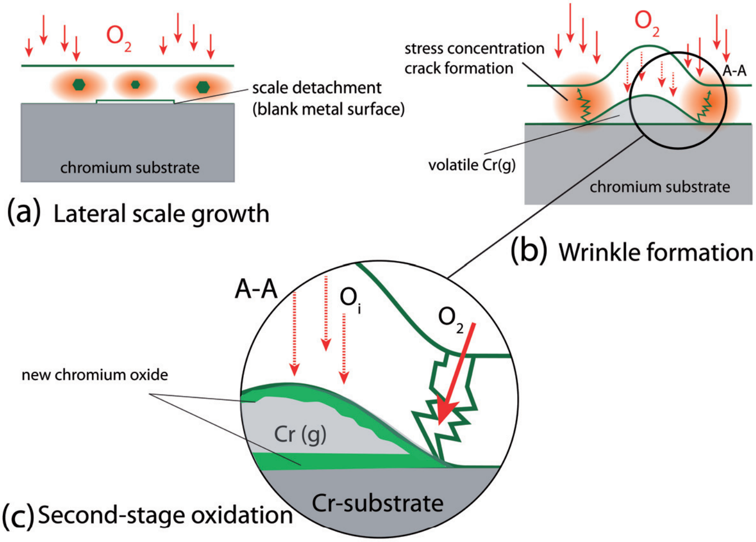

Figure 6-15. Schematic illustration of the wrinkling process in chromium oxide at high temperature oxidizing atmosphere (a) the initial lateral growth and scale detachment. (b) wrinkle formation (c) scale failure, second stage oxidation (detailed description in the text).

In Si containing alloys, chromia scales with finer grain structures form which can be attributed to the doped Si in the scale. The composition of the scales formed during isothermal oxidation at 1200°C (Table 7) reveal constant traces of Si in both binary and ternary alloys. Considering the average thickness of the oxide scales (e.g. ~20µm for alloy S3) and the voltage used for EDS analysis (15KV), it is reasonable to say that the signal is exclusively from the scale. The Cr_2O_3-SiO_2 phase diagram shows that SiO_2 is not soluble in chromia (see Figure 6-14). As SiO_2 is more stable than Cr_2O_3, the doped Si in the chromia scale can reduce chromia via a silicothermic reaction (Eq. 25).

$$3Si + 2Cr_2O_3 \rightarrow 3SiO_2 + 4Cr \tag{25}$$

The newly formed SiO_2 micro particles can act as heterogeneous nucleation sites for Cr_2O_3 which in turn, results in the recrystallization of Cr_2O_3 at high temperatures. This process was observed elsewhere for chromia forming alloys [186].

It is important to note that, the grains formed during isothermal exposure at 1200°C (Figure 5-24) are finer than those formed at 1050°C (Figure 5-25). This can be related to a recrystallization process at higher temperatures where the scale is under larger growth stresses which, in turn, leads to a finer oxide microstructure. This is in agreement with observations at 1350°C [14] where a finer microstructure of chromia is evident. Otherwise, one would expect a coarser grain structure at higher temperatures.

To the best of the author's knowledge, formation of Cr_2O_3 single crystals on the surface of chromia scales (see Figure 5-24) has not been reported elsewhere. These crystals appeared exclusively on Si-containing alloys. In addition, it is important to note that single crystals form only at temperatures higher than 1050°C. Experimental results proved the formation of these single crystals at 1200°C (Figure 5-24) and 1350°C [14]. The exact mechanism of single crystal formation has not been discussed elsewhere yet. The distinct difference between the size of these single crystals and the scale morphology implies that their growth mechanism is independent of the rest of the scale.

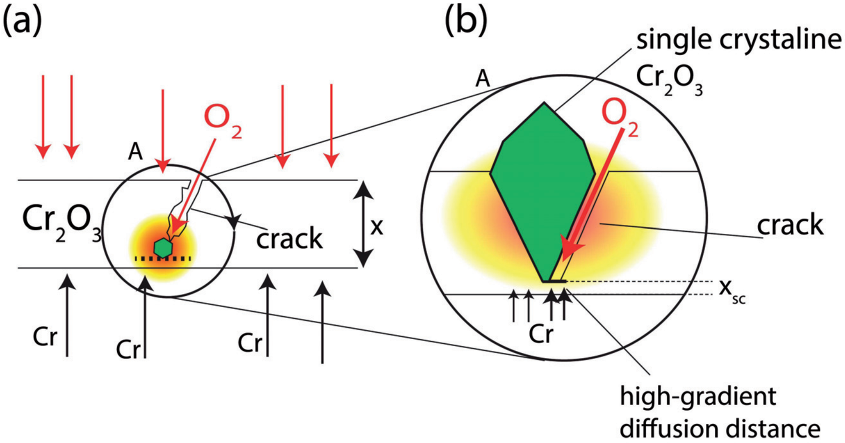

Figure 6-16. Schematic illustration of a possible mechanism for single crystal growth within the chromia scale.

The fact that these crystals nucleate inside the scale is proven by microscopic observations (see Figure 5-24). One can speculate that some Cr_2O_3 grains can nucleate on the newly formed SiO_2 particle and (under certain conditions) grow faster than other grains in the structure. However, the epitaxial growth can also be accelerated by a large concentration gradient of chromium and oxygen which can be induced by mechanical defects, such as cracks. When a large crack is formed in the scale, the crack tip will be healed by the fresh oxide as explained before. This offers a locally short diffusion distance (oxide thickness) which, in turn, provides a fast oxidation kinetics resembling the initial stage of the parabolic growth. This process can continue as long as the growth stress in the oxide is high enough to keep the crack open. Both of these theories require that the growth exclusively occurs at a preferred orientation at the heterogeneous nucleation site or at the end of the open crack. **Figure 6-16** illustrates the proposed model schematically.

6.5.3 Adhesion of chromia to the alloys substrate

Discontinuous oxidation behavior of Cr, Cr-Si, and Cr-Ge-Si alloys can also give information on the adhesion properties of the oxide scale, as the alloy-scale interface showed different coverage of oxide residues after the oxidation test.

Severe spallation was expected for the pure chromium substrate due to the high mismatch between Cr and Cr_2O_3. However, visual observations showed that the scale was already detached from the substrate and was severely deformed during the exposure without spallation. The mass change curves (see Figure 5-15) and the post exposure microscopy of oxide residues (see Figure 5-29) showed that alloys with higher Si contents offer higher scale adherence to the substrate and accordingly less spallation. The significant adherence of the oxide scale to the single phase A15 alloy (S25) is surprising. The micrograph in Figure 5-29d showed a full coverage of the scale on the A15 single phase substrate. The coefficient of thermal expansion (CTE) of Cr, Cr_2O_3, Cr_2N and Cr_3Si has been reported to be 4.9, 8.8, 9.4, and 9.2 $\times 10^{-6}$ K^{-1}, respectively [32,187]. The lowest CTE mismatch between the chromia scale and substrate can be obtained for Cr_3Si. This is in good agreement with the high adherence of the chromia scale to alloy S25 substrate (see Figure 5-15). Improved adherence of the scale is found when a Cr_3Si silicide layer is developed in the subscale zone. This is clearly evident from the subscale surface morphology of the hyper-eutectic alloy S19 (with primary A15 dendrites) where the chromia coverage is evident on the primary A15 dendrites (see Figure 5-29c). Thus, the A15-layer formed on the chromium alloy substrates can act as a “bond coat” for the chromia scale. Since the single phase alloy S3 does not form a A15-silicide layer, this effect on the oxide scale cannot occur in turn, severe spallation is observed. (Figure 5-15, Figure 5-29a).

Observation of the higher chromia coverage on the substrate when alloyed with Ge in Figure 5-29 showed that the co-addition of both of Ge and Si can significantly improve the adherence of the scale to the substrate as alloy S18G1 shows the highest resistance to discontinuous oxidation compared to other two-phase alloys (Figure 5-21). This can be correlated to the enhanced adherence and re-healing behavior of silica upon Ge doping as explained in section 6.4.

7 CONCLUDING REMARKS

This study was focused on the high temperature oxidation-nitridation of pure chromium and chromium-based alloys in air. Oxidation and nitridation kinetics of pure chromium were compared in single oxidant (i.e. Ar-20%O_2 and N_2-5%H_2) and multi-oxidant (i.e. synthetic air) atmospheres. It was clearly shown that the major part of oxidation kinetics in air is attributed to the internal nitridation of the Cr-substrate. Thermogravimetric results and post exposure cross section investigations showed that the chromia scale does not offer protection against inward nitrogen permeation at the test temperatures.

Oxidation and nitridation behavior of the Cr-Si system revealed that regardless of the Si content in solid-solution and the silicide phases, chromium is the primarily diffusing alloy component.

It was found that Si additions lead to the local formation of SiO_2 resulting in slower oxidation kinetics by reducing the outward diffusion of chromium and inward diffusion of nitrogen. The A15 silicide showed the highest oxidation resistance via full coverage of a Si-rich oxide beneath the chromia scale. Long term oxidation resistance (up to 1000h) of the A15 silicide phase was associated with the phase transformation in the subsurface zone during oxidation. This led to the formation of a SiO_2-former silicide phase (Cr_5Si_3) which offered higher protection during long term exposures.

In addition, thermodynamic calculations and experimental characterization showed that Cr_3Si is stable under nitriding atmospheres and does not form Cr-nitride of any kind even after long term exposure at 1200°C.

Under oxidizing atmospheres, the technically interesting two-phase Cr-Cr_3Si eutectic alloy showed cooperative oxidation of both constituent phases as outward diffusion of chromium governed the oxidation behavior leaving a single phase A15 layer behind at the alloy-oxide interface. The self-developing homogeneous A15 layer was later shown to be a barrier against inward nitrogen diffusion protecting the substrate microstructure from selective nitriding of the solid-solution phase.

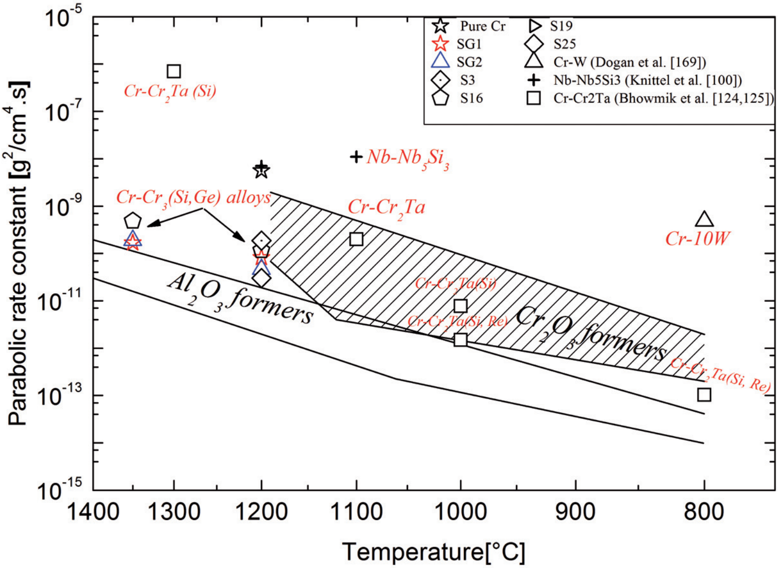

Figure 7-1. The parabolic rate constant for oxidation kinetics of the recently developed Cr-based and Nb-based alloys.

The beneficial influence of Ge in oxidation-nitridation of Cr-Si binary alloys was revealed after crystallographic and microstructural investigations of the Cr-Ge-Si system. The facts that Ge can substitute Si in both solid-solution and silicide phases in the Cr-Cr_3Si system and the peritectic reaction in Cr-Ge system provided a two-phase microstructure with higher stability of the A15 phase. Alloy SG2 (Cr-14Si-2Ge) showed the optimized oxidation-nitridation behavior with a nitride-free microstructure after 1000h exposure at 1200°C in air. Lower outward diffusion of Cr and higher microstructural stability of the A15 phase were found to be responsible for the self-protecting character of the alloy against nitriding.

The developed Cr-Cr_3(Si,Ge) alloys offer promising oxidation behavior at temperatures above the stability of Ni-based superalloys. These alloys showed significantly enhanced oxidation resistance close to that of alumina formers and are superior to other structural alloys such as Nb-Nb_5Si_3 and Cr-Cr_2(Ta,Nb) alloys (see Figure 7-1).

As nitridation has long been the major drawback in the development of Cr-based alloys, its mitigation in Cr-Ge-Si alloys opens a new window towards the future of chromium-based alloys.

8 OUTLOOK

The research presented in this thesis resulted in a solution preventing nitridation of chromium based alloys above 1000°C. There are, however, remaining challenges with regards to this class of alloys.

1. It is necessary to understand the mechanical behavior of these alloys at room and high temperatures. Mechanical properties such as room- and high-temperature toughness, creep behavior, and ductile-brittle transition behavior need to be studied in the future. In addition, the influence of current alloying elements and further elements on the mechanical properties should be investigated.

2. The fact that A15-intermetallic precipitates form during the annealing of Cr-Si-Ge alloys opens a new window to the design of microstructure via heat treatment processes. The high alloying capacity of Cr with other refractory elements such as Pt (A15-former) and Mo (highly soluble in Cr) offer unique chances to design alloys with microstructures similar to that of longstanding Ni-based superalloys for high temperature structural applications.

3. The most important finding of this work is that a self-developing A15-silicide layer at the surface of the alloy acts as a barrier against nitridation at high temperatures and can be used for the development of novel silicide coatings to protect Cr- and other engineering alloys against nitridation. Single phase Cr-alloys can be coated with this silicide which ensures protection against nitrogen embrittlement at high temperatures.

4. This work provided further experimental proofs that nitrogen transport can occur through chromia scales formed on pure Cr and Cr-based alloys. So far the mechanism is not finally clear and can be either the grain boundary transport or the dynamic crack formation and healing process (pseudo-plasticity). A systematic measurement using

atom probe tomography or two-step thermogravimetry switching from oxidation in pure oxygen to exposure in pure nitrogen can provide a clear answer.

9 BIBLIOGRAPHY

[1] J.H. Schneibel, Beyond nickel-base superalloys, World Scientific, 2005, p. 563.

[2] H. Bei, G.M. Pharr, and E.P. George, A review of directionally solidified intermetallic composites for high-temperature structural applications, J. Mater. Sci., 39 (2004) 3975-3984.

[3] J.H. Perepezko, The Hotter the Engine, the Better, Science, 326 (2009) 1068-1069.

[4] J.A. Lemberg and R.O. Ritchie, Mo-Si-B Alloys for Ultrahigh-Temperature Structural Applications, Adv. Mater., 24 (2012) 3445–3480.

[5] B.P. Bewlay, M.R. Jackson, P.R. Subramanian, and J.C. Zhao, A review of very-high-temperature Nb-silicide-based composites, Metallurgical and Materials Transactions A, 34 (2003) 2043-2052.

[6] J.H. Schneibel, High temperature strength of Mo–Mo_3Si–Mo_5SiB_2 molybdenum silicides, Intermetallics, 11 (2003) 625-632.

[7] D.L. Anton and D.M. Shah, High temperature properties of refractory intermetallics, Mat. Res. Soc. Symp. Proc., 213 (1991) 733-738.

[8] B.P. Bewlay, J.A. Sutliff, M.R. Jackson, and K.M. Chang, Processing, Microstructures, and Properties of Cr-Cr_3Si, Nb-Nb_3Si, and V-V_3Si Eutectics, Materials and Manufacturing Processes, 9 (1994) 89-109.

[9] B.P. Bewlay, K.M. Chang, J.A. Sutliff, and M.R. Jackson, Microstructures and Properties of Refractory Metal-Silicide Eutectics, Cambridge Univ Press, 1992.

[10] D.M. Dimiduk and J.H. Perepezko, Mo-Si-B alloys: Developing a revolutionary turbine-engine material, MRS Bulletin-Materials Research Society, 28 (2003) 639-645.

[11] M. Takeyama and C.T. Liu, Microstructure and mechanical properties of Laves-phase alloys based on Cr2Nb, Materials Science and Engineering: A, 132 (1991) 61-66.

[12] M.P. Brady, P.F. Tortorelli, and L.R. Walker, Correlation of alloy microstructure with oxidation behavior in chromia-forming intermetallic-reinforced Cr alloys, Materials at High Temperatures, 17 (2000) 235-243.

[13] M.P. Brady, I.G. Wright, and B. Gleeson, Alloy design strategies for promoting protective oxide-scale formation, Journal of the Minerals, Metals and Materials Society, 52 (2000) 16-21.

[14] A. Soleimani-Dorcheh, W. Donner, and M.C. Galetz, On ultra-high temperature oxidation of Cr–Cr_3Si alloys: Effect of germanium, Mater. Corros., 65 (2014) 1143-1150.

[15] S.V. Raj, An evaluation of the properties of Cr3Si alloyed with Mo, Materials Science and Engineering: A, 201 (1995) 229-241.

[16] J. Ang, V.A. Vorontsov, C.L. Hayward, G. Balakrishnan, H.J. Stone, and C.M.F. Rae, Quarternary and Quinary Additions to Directionally-Solidified X-X3Si Eutectics of Chromium and Vanadium, Cambridge Univ Press, 2011.

[17] H. Bei, E.P. George, and G.M. Pharr, Elastic constants of single crystal Cr3Si and Cr–Cr3Si lamellar eutectic composites: a comparison of ultrasonic and nanoindentation measurements, Scripta Materialia, 51 (2004) 875-879.

[18] H. Bei, E.P. George, and G.M. Pharr, Effects of Solidification Parameters on Lamellar Microstructures of Near Eutectic Cr-Cr_3Si Alloys, MRS Proceedings, 753 (2003) BB2.5.

[19] A. Gali, H. Bei, and E.P. George, Effect of processing and Microalloying Elements on the Thermal Stability of Cr-Cr_3Si and NiAl-Mo eutectic alloys, Advanced Intermetallic-Based Alloys, 980 (2007) 0980-II05-36.

[20] Y. Gu, H. Harada, and Y. Ro, Chromium and chromium-based alloys: Problems and possibilities for high-temperature service, JOM Journal of the Minerals, Metals and Materials Society, 56 (2004) 28-33.

[21] H. Johansen and G. Asai, Room–Temperature Ductile Chromium, J. Electrochem. Soc., 101 (1954) 604-612.

[22] D.M. Scruggs, Ductile Chromium Composition. [3175279]. 30-3-1965. US PATENTS.

[23] L. Royer, X. Ledoux, S. Mathieu, and P. Steinmetz, On the Oxidation and Nitridation of Chromium at 1300°C, Oxidation of Metals, 74 (2010) 79-92.

[24] B.V. Cockeram and R.A. Rapp, Oxidation-resistant boron- and germanium-doped silicide coatings for refractory metals at high temperature, Materials Science and Engineering: A, 192-193, Part 2 (1995) 980-986.

[25] B.V. Cockeram, Growth and oxidation resistance of boron-modified and germanium-doped silicide diffusion coatings formed by the halide-activated pack cementation method, Surf. Coat. Technol., 76–77, Part 1 (1995) 20-27.

[26] H. Okamoto, Cr-Si (Chromium-Silicon), Journal of Phase Equilibria and Diffusion, 22 (2001) 593.

[27] H. Okamoto, Cr-Ge (Chromium-Germanium), Journal of Phase Equilibria and Diffusion, 31 (2010) 487-488.

[28] W. Kroll, Das duktile Chrom, Zeitschrift für anorganische und allgemeine Chemie, 226 (1935) 23-32.

[29] American Society for Metals, Ductile chromium and its alloys, *Metal Congress and Exposition of the American Society for Metals*, American Society for Metals, United States.Office of Ordnance Research, 1957.

[30] H.B. Goodwin, E.A. Gilbert, C.M. Schwartz, and C.T. Greenidge, A Preliminary Study of the Ductility of Chromium, J. Electrochem. Soc., 100 (1953) 152-160.

[31] E.A. Brandes, H.T. Greenaway, and H.E.N. Stone, Ductility in Chromium, Nature, 178 (1956) 587.

[32] K. Taneichi, T. Narushima, Y. Iguchi, and C. Ouchi, Oxidation or Nitridation Behavior of Pure Chromium and Chromium Alloys Containing 10 mass% Ni or Fe in Atmospheric Heating, Materials transactions, 47 (2006) 2540.

[33] A.U. Seybolt and D.H. Haman, Oxidation-Nitrification of Chromium at 1000°C, Transactions of the Metallurgical Society of AIME, 230 (1964) 1294.

[34] P. Kofstad, High Temperature Corrosion, Elsevier Applied Science, 1988.

[35] E.A. Gulbransen and K.F. Andrew, A Preliminary Study of the Oxidation and Vapor Pressure of Chromium, J. Electrochem. Soc., 99 (1952) 402-406.

[36] H. Taimatsu, Kinetic Analysis of High Temperature Oxidation of Metals Accompanied by Scale Volatilization, J. Electrochem. Soc., 146 (1999) 3686-3689.

[37] W.H. Smith and A.U. Seybolt, Ductile chromium, J. Electrochem. Soc., 103 (1956) 347-352.

[38] D.J. Young and M. Cohen, Pressure Effects in the Oxidation of Chromium, J. Electrochem. Soc., 124 (1977) 775-779.

[39] E.A. Gulbransen and K.F. Andrew, Kinetics of the Oxidation of Chromium, J. Electrochem. Soc., 104 (1957) 334-338.

[40] D. Caplan and M. Cohen, The Volatilization of Chromium Oxide, J. Electrochem. Soc., 108 (1961) 438-442.

[41] W.C. Hagel, Factors controlling the high-temperature oxidation of chromium, Trans. ASM, 56 (1963) 583-599.

[42] A.H. Sully, E.A. Brandes, and A.G. Provan, The properties of cast chromium alloys at elevated temperatures. 1. The melting and casting of chromium-rich alloys, Journal of Institute of Metals, 81 (1953) 569-572.

[43] R.M. Parke and F.P. Bens, Chromium-Base Alloys, ASTM International, 1946, p. 80.

[44] K.P. Lillerud and P. Kofstad, On High Temperature Oxidation of Chromium I. Oxidation of Annealed, Thermally Etched Chromium at 800-1100° C, J. Electrochem. Soc., 127 (1980) 2397-2410.

[45] D.J. Young, High temperature oxidation and corrosion of metals, Access Online via Elsevier, 2008.

[46] N. Birks, G.H. Meier, and F.S. Pettit, Introduction to the high temperature oxidation of metals, Cambridge University Press, 2006.

[47] C. Wagner, Formation of Composite Scales Consisting of Oxides of Different Metals, J. Electrochem. Soc., 103 (1956) 627-633.

[48] G.A. Hope and I.M. Ritchie, Mechanism of chromium oxidation, J. Chem. Soc. , Faraday Trans. 1, 77 (1981) 2621-2631.

[49] D.J. Young and M. Cohen, Oxidation Behavior of Chromium Between 300° and 600° C, J. Electrochem. Soc., 124 (1977) 769-774.

[50] Y. Sakisaka, H. Kato, and M. Onchi, Oxygen chemisorption and initial oxidation of Cr(110), Surface Science, 120 (1982) 150-170.

[51] A.S. Khanna, Introduction to High Temperature Oxidation and Corrosion, ASM International, 2002.

[52] K.P. Lillerud and P. Kofstad, Chromium transport through Cr2O3 scales. II. Changes in scale morphology during high vacuum treatment of oxidized chromium specimens, Oxid Met, 17 (1982) 195-203.

[53] H. Hindam and D.P. Whittle, Microstructure, adhesion and growth kinetics of protective scales on metals and alloys, Oxid Met, 18 (1982) 245-284.

[54] D. Caplan and G.I. Sproule, Effect of oxide grain structure on the high-temperature oxidation of Cr, Oxid Met, 9 (1975) 459-472.

[55] E.W.A. Young, J.H. Gerretsen, and J.H.W. De Wit, The oxygen partial pressure dependence of the defect structure of chromium (III) oxide, J. Electrochem. Soc., 134 (1987) 2257-2260.

[56] P. Kofstad and K.P. Lillerud, On High Temperature Oxidation of Chromium: II . Properties of and the Oxidation Mechanism of Chromium, J. Electrochem. Soc., 127 (1980) 2410-2419.

[57] F.A. Kröger, Defects and Transport in SiO2, Al2O3, and Cr2O3, in: R.A. Rapp (Ed.), Proceedings of High Temperature Corrosion, Houston, NACE, 1983, pp. 89-100.

[58] A. Holt and P. Kofstad, Electrical conductivity and defect structure of Cr2O3. I. High temperatures, Solid State Ionics, 69 (1994) 127-136.

[59] P. Kofstad, Defects and transport properties of metal oxides, Oxid Met, 44 (1995) 3-27.

[60] P. Kofstad and K.P. Lillerud, Chromium transport through Cr2O3 scales I. On lattice diffusion of chromium, Oxid Met, 17 (1982) 177-194.

[61] K. Hoshino and N.L. Peterson, Cation Self-Diffusion in Cr2O3, J. Am. Ceram. Soc., 66 (1983) c202-c203.

[62] A.C.S. Sabioni, A.M. Huntz, F. Millot, and C. Monty, Self-diffusion in cr2o3 III. Chromium and oxygen grain-boundary diffusion in polycrystals, Philosophical Magazine A, 66 (1992) 361-374.

[63] A.C.S. Sabioni, A.M. Huntz, F. Millot, and C. Monty, Self-diffusion in cr2o3 II. Oxygen diffusion in single crystals, Philosophical Magazine A, 66 (1992) 351-360.

[64] A.C.S. Sabioni, B. Lesage, A.M. Huntz, J.C. Pivin, and C. Monty, Self-diffusion in cr2o3 I. Chromium diffusion in single crystals, Philosophical Magazine A, 66 (1992) 333-350.

[65] A.C.S. Sabioni, A.M. Huntz, J. Philibert, B. Lesage, and C. Monty, Relation between the oxidation growth rate of chromia scales and self-diffusion in Cr2O3, J Mater Sci, 27 (1992) 4782-4790.

[66] A.C.S. Sabioni, F.L. Freire Jr, C.V.B. Leite, B.A. Amami, C. Dolin, C. Monty, and F. Millot, Study of oxygen self-diffusion in oxides by ion beam techniques: comparison between nuclear reaction analysis and SIMS, Nuclear Instruments and Methods in Physics Research Section B: Beam Interactions with Materials and Atoms, 73 (1993) 85-89.

[67] W.C. Hagel and A.U. Seybolt, Cation Diffusion in Cr_2O_3, J. Electrochem. Soc., 108 (1961) 1146-1152.

[68] K. Taneichi, T. Narushima, Y. Iguchi, and C. Ouchi, Oxidation or nitridation behavior of pure chromium and chromium alloys containing 10mass% Ni or Fe in atmospheric heating, Materials transactions, 47 (2006) 2540-2546.

[69] L. Cadiou and J. Paidassi, Contribution to the study of the reaction of chromium with oxygen at elevated temperatures, Mem. Sci. Rev. Met., 66 (1969) 217-225.

[70] M. Michalik, Effect of water vapour on growth and adherence of chromia scales on pure chromium. 2007. Universitätsbibliothek RWTH Aachen.

[71] G. Hultquist, B. Tveten, and E. Hörnlund, Hydrogen in Chromium: Influence on the High-Temperature Oxidation Kinetics in H2O,Oxide-Growth Mechanisms, and Scale Adherence, Oxid. Met., 54 (2000) 1-10.

[72] S.R.J. Saunders, M. Monteiro, and F. Rizzo, The oxidation behaviour of metals and alloys at high temperatures in atmospheres containing water vapour: A review, Progress in Materials Science, 53 (2008) 775-837.

[73] P. Fox, D.G. Lees, and G.W. Lorimer, Sulfur segregation during the high-temperature oxidation of chromium, Oxid Met, 36 (1991) 491.

[74] M. Hänsel, W.J. Quadakkers, and D.J. Young, Role of Water Vapor in Chromia-Scale Growth at Low Oxygen Partial Pressure, Oxid. Met., 59 (2003) 285-301.

[75] X.G. Zheng and D.J. Young, High-temperature corrosion of Cr2O3-forming alloys in CO-CO2-N2 atmospheres, Oxid Met, 42 (1994) 163-190.

[76] S.R.J. Saunders, M. Monteiro, and F. Rizzo, The oxidation behaviour of metals and alloys at high temperatures in atmospheres containing water vapour: A review, Progress in Materials Science, 53 (2008) 775-837.

[77] E.A. Polman, T. Fransen, and P.J. Gellings, Oxidation kinetics of chromium and morphological phenomena, Oxid. Met., 32 (1989) 433-447.

[78] X.G. Zheng and D.J. Young, High temperature reaction of chromium with multi-oxidant atmospheres, Trans Tech Publ, 1997, pp. 567-574.

[79] M. Hänsel, E. Turan, V. Shemet, D. Grüner, U. Breuer, D. Simon, B. Gorr, H.J. Christ, and W.J. Quadakkers, Effect of specimen thickness on chromia scaling of Ni25Cr in N2-O2-H2O test gases at 1000C, Materials at High Temperatures, 32 (2015) 160-166.

[80] C.S. Giggins and F.S. Pettit, Corrosion of Metals and Alloys in Mixed Gas Environments at Elevated Temperatures, Oxid. Met., 14 (1980) 363-413.

[81] A. Soleimani Dorcheh and M.C. Galetz, Oxidation and Nitridation Behavior of Cr-Si Alloys in Air at 1473K, Oxid. Met., 84 (2015) 73-90.

[82] I. Murris, Y.P. Jacob, V.A.C. Haanappel, and M.F. Stroosnijder, High-Temperature Oxidation Behavior of Chromium: Effect of Different Batches, Oxid. Met., 55 (2001) 307-331.

[83] M. Michalik, S.L. Tobing, M. Hänsel, V. Shemet, W.J. Quadakkers, and D.J. Young, Effects of water vapour on the high temperature nitridation of chromium, Mater. Corros., 65 (2014) 260-266.

[84] D.J. Young, T.D. Nguyen, P. Felfer, J. Zhang, and J.M. Cairney, Penetration of protective chromia scales by carbon, Scripta Materialia, 77 (2014) 29-32.

[85] T. Nguyen, J. Zhang, and D. Young, Water Vapor Effects on Corrosion of Fe-Cr and Fe-Cr-Ni Alloys Containing Silicon in CO2 Gas at 818°C, Oxid Met, (2015) 1-20.

[86] T. Mills, The solubility of nitrogen in solid chromium, Journal of the Less Common Metals, 23 (1971) 317-324.

[87] T. Mills, Thermodynamic relations in the chromium-nitrogen system, Journal of the Less Common Metals, 26 (1972) 223-234.

[88] K. Schwerdtfeger, The Nitriding of Chromium in N2-H2 Gas Mixtures at Elevated Temperatures, Transactions of the Metallurgical Society of AIME, 239 (1968) 1432-1438.

[89] K.N. Strafford, A comparison of the high temperature nitridation and oxidation behaviour of metals, Corrosion Science, 19 (1979) 49-62.

[90] T. Mills, Nitriding of chromium in nitrogen gas at high temperatures, Oxid Met, 15 (1981) 437-445.

[91] T. Mills, Diffusivity of nitrogen in chromium subnitride Cr2N, Oxid Met, 15 (1981) 447-454.

[92] Z.B. Qi, B. Liu, Z.T. Wu, F.P. Zhu, Z.C. Wang, and C.H. Wu, A comparative study of the oxidation behavior of Cr2N and CrN coatings, Thin Solid Films, 544 (2013) 515-520.

[93] P. Kofstad, On the formation of porosity and microchannels in growing scales, Oxid Met, 24 (1985) 265-276.

[94] Y.W. Kim and G.R. Belton, The thermodynamics of volatilization of chromic oxide: Part I. the species CrO_3 and CrO_2 OH, MT, 5 (1974) 1811-1816.

[95] H. Graham and H. Davis, Oxidation/Vaporization Kinetics of Cr_2O_3, J. Am. Ceram. Soc., 54 (1971) 89-93.

[96] R.T. Grimley, R.P. Burns, and M.G. Inghram, Thermodynamics of the vaporization of Cr_2O_3: dissociation energies of CrO, CrO_2, and CrO_3, The Journal of chemical physics, 34 (1961) 664-667.

[97] C.S. Tedmon, The Effect of Oxide Volatilization on the Oxidation Kinetics of Cr and Fe-Cr Alloys, J. Electrochem. Soc., 113 (1966) 766-768.

[98] B. Pujilaksono, T. Jonsson, M. Halvarsson, I. Panas, J.-E. Svensson, and L.-G. Johansson, Paralinear Oxidation of Chromium in O2 + H_2O Environment at 600–700°C, Oxidation of Metals, 70 (2008) 163-188.

[99] M. Hänsel, W.J. Quadakkers, L. Singheiser, and H. Nickel, Korrosions-und Kompatibilitätsstudien an Cr-Basislegierungen für den metallischen Interkonnektor der Hochtemperaturbrennstoffzelle (SOFC). 1998. Forschungszentrum Jülich GmbH.

[100] S. Mathieu, S. Knittel, M. Francios, L. Portebois, S. Mathieu, and M. Vilasi, Towards the improvement of the oxidation resistance of Nb-silicides in situ composites: A solid state diffusion approach, Corrosion Science, (2013).

[101] S. Knittel, S. Mathieu, and M. Vilasi, Effect of tin addition on Nb–Si-based in situ composites. Part I: Structural modifications, Intermetallics, (2014).

[102] S. Knittel, S. Mathieu, L. Portebois, and M. Vilasi, Effect of tin addition on Nb–Si-based in situ composites. Part II: Oxidation behaviour, Intermetallics, (2014).

[103] Z. Li and L.M. Peng, Ultra-high temperature Mo-Si-B alloys; Synthesis, microstructural and mechanical characterization, Materials Letters, 62 (2008) 2229-2232.

[104] Y.F. Gu, H. Harada, and Y. Ro, Chromium and chromium-based alloys: Problems and possibilities for high-temperature service, Journal of the Minerals, Metals and Materials Society, 56 (2004) 28-33.

[105] M. Gao, Ö. Dogan, P. King, A. Rollett, and M. Widom, The first-principles design of ductile refractory alloys, JOM Journal of the Minerals, Metals and Materials Society, 60 (2008) 61-65.

[106] M. Gao, Y. Suzuki, H. Schweiger, Ö. Dogan, J.A. Hawk, and M. Widom, Phase stability and elastic properties of Cr-V alloys, Journal of Physics: Condensed Matter, 25 (2013) 075402.

[107] A. Bhowmik, H.J. Stone, and I.M. Edmonds, Chromium alloy. 23-4-2013. Google Patents.

[108] Y. Gu, Y. Ro, and H. Harada, Tensile properties of chromium alloyed with silver, Metallurgical and Materials Transactions A, 35 (2004) 3329-3331.

[109] G.R. Wilms, The tensile properties of some extruded chromium alloys between 800 and 1000, Journal of the Less Common Metals, 6 (1964) 169-183.

[110] Y. Matsumoto, J. Fukumori, M. Morinaga, M. Furui, T. Nambu, and T. Sakaki, Alloying effect of 3d transition elements on the ductility of chromium, Scripta Materialia, 34 (1996) 1685-1689.

[111] Ö. Dogan, S. Chen, X. Song, and J. Sears, Structurally modulated precipitates in a refractory Cr–V alloy, J. Alloys and Comp., 509 (2011) 6556-6560.

[112] D.R. Lide, CRC Handbook of Chemistry and Physics, Boca Raton, FL, itd: CRC Press, (2003) 4-93.

[113] Y. Gu, Y. Ro, T. Kobayashi, and H. Harada, Microstructural evolution and mechanical properties of Cr-Ru alloys, Metallurgical and Materials Transactions A, 36 (2005) 577-582.

[114] J.R. Stephens, Exploratory investigation of Y, La, and Hf coatings for nitridation protection of chromium alloys, Metallurgical Transactions, 3 (1972) 2075-2086.

[115] W. Chan, M. Gao, Ö. Dogan, P. King, and A. Rollett, Thermodynamic Assessment of Cr-Rare Earth Systems, J. Phase Equilib. Diffus., 30 (2009) 578-586.

[116] J. Lei, B. Chen, S. Guo, K. Wang, L. Tan, E. Khosravi, J. Yan, S.V. Raju, and S. Yang, Structural and mechanical stability of dilute yttrium doped chromium, Applied Physics Letters, 102 (2013) 021901.

[117] D.M. Scruggs, L.H. Vlack, and W.M. Spurgeon, Reaction between nitrogen and spinel in chromium, J. Am. Ceram. Soc., 51 (1968) 473-481.

[118] M.P. Brady, I.G. Wright, I.M. Anderson, V.K. Sikka, E.K. Ohriner, C. Walls, G. Westmoreland, and M.L. Weaver, Ductilization of Cr via oxide dispersions, 2001.

[119] S.V. Raj, A preliminary assessment of the properties of a chromium silicide alloy for aerospace applications, Materials Science and Engineering: A, 192–193, Part 2 (1995) 583-589.

[120] S.V. Raj, J. Daniel Whittenberger, B. Zeumer, and G. Sauthoff, Elevated temperature deformation of Cr3Si alloyed with Mo, Intermetallics, 7 (1999) 743-755.

[121] L. Royer, S. Mathieu, C. Liebaut, and P. Steinmetz, Elaboration and Characterization of the Properties of Refractory Cr Base Alloys, Advances in Science and Technology, 72 (2011) 46-52.

[122] C.T. Liu, P.F. Tortorelli, J.A. Horton, and C.A. Carmichael, Effects of alloy additions on the microstructure and properties of $CrCr_2Nb$ alloys, Materials Science and Engineering: A, 214 (1996) 23-32.

[123] M.P. Brady, J.H. Zhu, C.T. Liu, P.F. Tortorelli, and L.R. Walker, Oxidation resistance and mechanical properties of Laves phase reinforced Cr in-situ composites, Intermetallics, 8 (2000) 1111-1118.

[124] A. Bhowmik, H.T. Pang, I.M. Edmonds, C.M.F. Rae, and H.J. Stone, Effect of silicon additions on the high temperature oxidation behaviour of Cr–Cr2Ta alloys, Intermetallics, 32 (2013) 373-383.

[125] A. Bhowmik, R.J. Bennett, B. Monserrat, G.J. Conduit, L.D. Connor, J.E. Parker, R.P. Thompson, C.N. Jones, and H.J. Stone, Alloys based on Cr-Cr2Ta containing Si, Intermetallics, (2013).

[126] M. Schütze, Fundamentals of High Temperature Corrosion, Corrosion and Environmental Degradation, Wiley-VCH, 2000, pp. 67-130.

[127] P. Steinmetz, S. Mathieu, L. Royer, and C. Liebaut, Oxidation and Nitridation of Pure Chromium at Elevated Temperature in Synthetic Air-Effect of Silicon Addition, Trans Tech Publ, 2008, pp. 1047-1055.

[128] V.M. Chad, M.I.S.T. Faria, G.C. Coelho, C.A. Nunes, and P.A. Suzuki, Microstructural characterization of as-cast Cr–Si alloys, Materials Characterization, 59 (2008) 74-78.

[129] F. Gesmundo and B. Gleeson, Oxidation of multicomponent two-phase alloys, Oxidation of Metals, 44 (1995) 211-237.

[130] A. Gali, Thermal Stability of Binary Cr-Cr3Si and Ternary NiAl-Mo Eutectic Alloys. 1-114. 2006. United States - Tennessee, The University of Tennessee.

[131] T.A. Cruse and J.W. Newkirk, Evaluation of methods to produce tough Cr3Si based composites, Materials Science and Engineering: A, 239–240 (1997) 410-418.

[132] J.A. Sago and J.W. Newkirk, Ductile phase toughening of Cr3Si with chromium, Intermetallic Matrix Composites, 194 (1990) 183-189.

[133] J.B. Nelson and, An experimental investigation of extrapolation methods in the derivation of accurate unit-cell dimensions of crystals, Proceedings of the Physical Society, 57 (1945) 160.

[134] A. Berche, J.C. Tedenac, and P. Jund, Ab-initio calculations and CALPHAD description of Cr-Ge-Mn and Cr-Ge-Si, Calphad, 49 (2015) 50-57.

[135] H. Baker and H. Okamoto, ASM handbook, ASM International, Materials Park, Ohio, 1992.

[136] H. Bei, E.P. George, and G.M. Pharr, Effects of composition on lamellar microstructures of near-eutectic CrCr3Si alloys, Intermetallics, 11 (2003) 283-289.

[137] A. Gokhale and G. Abbaschian, The Cr–Ge (Chromium-Germanium) system, Journal of Phase Equilibria, 7 (1986) 477-485.

[138] W.J. Quadakkers, Growth mechanisms of oxide scales on ODS alloys in the temperature range 1000-1100°C, Mater. Corros., 41 (1990) 659-668.

[139] Y.G. Gogotsi and V.A. Lavrenko, Corrosion of high-performance ceramics, Springer Science & Business Media, 2012.

[140] S. Han and D.J. Young, Oxidation - Nitridation of Ni-Cr-Al alloys, Materials Research, 7 (2004) 11-16.

[141] D.J. Young, T.D. Nguyen, P. Felfer, J. Zhang, and J.M. Cairney, Penetration of Protective Chromia Scales by Carbon, Scripta Materialia, (2014).

[142] A. La Fontaine, B. Gault, A. Breen, L. Stephenson, A.V. Ceguerra, L. Yang, T. nh Nguyen, J. Zhang, D.J. Young, and J.M. Cairney, Interpreting atom probe data from chromium oxide scales, Ultramicroscopy, (2015).

[143] F.N. Rhines and J.S. Wolf, The role of oxide microstructure and growth stresses in the high-temperature scaling of nickel, Metallurgical Transactions, 1 (1970) 1701-1710.

[144] A. Atkinson, R.I. Taylor, and P.D. Goode, Transport Processes in the Oxidation of Ni Studied Using Tracers in Growing NiO Scales, Oxidation of Metals, 13 (1979) 519-543.

[145] M. Schütze, Protective oxide scales and their breakdown, Wiley Chichester, 1997.

[146] M. Schütze, Course notes:High temperature corrosion, RWTH Aachen. 2011.

[147] P. Carter, B. Gleeson, and D.J. Young, Calculation of precipitate dissolution zone kinetics in oxidising binary two-phase alloys, Acta Mater., 44 (1996) 4033-4038.

[148] D.P. Whittle, Spalling of protective oxide scales, Oxidation of Metals, 4 (1972) 171-179.

[149] C. Wagner, Reaktionstypen bei der Oxydation von Legierungen, Ztschr. Elektrochem., 63 (1959) 772-782.

[150] F. Gesmundo and F. Viani, Transition from internal to external oxidation for binary alloys in the presence of an outer scale, Oxidation of Metals, 25 (1986) 269-282.

[151] G. Bamba, Y. Wouters, A. Galerie, F. Charlot, and A. Dellali, Thermal oxidation kinetics and oxide scale adhesion of Fe-15Cr alloys as a function of their silicon content, Acta Mater., 54 (2006) 3917-3922.

[152] L. Mikkelsen, S. Linderoth, and J.B. Bilde-Sorensen, The effect of silicon addition on the high temperature oxidation of a Fe-Cr alloy, Trans Tech Publ, 2004, pp. 117-122.

[153] M.H. Sluiter, Interstitials in tetrahedrally close-packed phases: C, N, O, and F in β–tungsten from first principles, Phys. Rev. B, 80 (2009) 220102.

[154] S. Prasad and A. Paul, Diffusion mechanism in XSi2 and X5Si3 (X= Nb, Mo, V) phases, Trans Tech Publ, 2012, pp. 459-464.

[155] S. Roy and A. Paul, Diffusion in tungsten silicides, Intermetallics, 37 (2013) 83-87.

[156] J. Shan. and Thermocalc, Personal communication. 2015.

[157] S. Prasad and A. Paul, Growth mechanism of phases by interdiffusion and diffusion of species in the niobium–silicon system, Acta Mater., 59 (2011) 1577-1585.

[158] S. Prasad and A. Paul, Growth mechanism of phases by interdiffusion and atomic mechanism of diffusion in the molybdenum–silicon system, Intermetallics, 19 (2011) 1191-1200.

[159] F. Gesmundo, P. Castello, and F. Viani, The steady-State corrosion kinetics of two-phase binary alloys forming the most-stable oxide, Oxidation of Metals, 46 (1996) 383-398.

[160] F. Gesmundo, F. Viani, and Y. Niu, The possible scaling modes in the high-temperature oxidation of two-phase binary alloys. Part I: High oxidant pressures, Oxid Met, 42 (1994) 409-429.

[161] J. Doychak and M.G. Hebsur, Protective Al2O3 scale formation on NbAl3-base alloys, Oxidation of Metals, 36 (1991) 113-141.

[162] R.N. Durham, B. Gleeson, and D.J. Young, Factors Affecting Chromium Carbide Precipitate Dissolution During Alloy Oxidation, Oxidation of Metals, 50 (1998) 139-165.

[163] R.N. Durham, B. Gleeson, and D.J. Young, The oxidation of multiphase iron-base alloys, Proceedings to the 13th International Corrosion Congress: Vol.III, Melbourne, Australia, 1996.

[164] M.P. Brady, P.F. Tortorelli, E.A. Payzant, and L.R. Walker, Oxidation behavior of Cr2N, CrNbN, and CrTaN phase mixtures formed on nitrided Cr and Laves-reinforced Cr alloys, Oxidation of Metals, 61 (2004) 379-401.

[165] D.R.F. West, Ternary equilibrium diagrams, Chapman and Hall, 1982.

[166] R.E. Reed-Hill and R. Abbaschian, Physical metallurgy principles, (1973).

[167] A. Soleimani Dorcheh and M.C. Galetz, Cr-Ge-Si Alloys for High-Temperature Structural Applications: Microstructural Evolution, Metall and Mat Trans A, 45 (2014) 1639-1645.

[168] L.A. Cornish, R. Suss, A. Watson, and S.N. Prins, Building a thermodynamic database for platinum-based superalloys: Part I, Platinum Metals Review, 51 (2007) 104-115.

[169] Dogan.Ö.N., Effect of Al on High-Temperature Oxidation of Cr–W Alloys, Oxidation of Metals, 69 (2008) 233-247.

[170] A. Mueller, G. Wang, R.A. Rapp, E.L. Courtright, and T.A. Kircher, Oxidation behavior of tungsten and germanium-alloyed molybdenum disilicide coatings, Materials Science and Engineering: A, 155 (1992) 199-207.

[171] Y.R. He, R.A. Rapp, and P.P. Tortorelli, Oxidation-resistant Ge-doped silicide coating on Cr-Cr_2Nb alloys by pack cementation, Mater. Sci. Eng. A, 222 (1997) 109-117.

[172] A. Mueller, G. Wang, R.A. Rapp, and E.L. Courtright, Deposition and Cyclic Oxidation Behavior of a Protective $(Mo,W)(Si, Ge)_2$ Coating on Nb-Base Alloys, J. Electrochem. Soc., 139 (1992) 1266-1275.

[173] M.P. Brady, J.H. Zhu, C.T. Liu, P.F. Tortorelli, L.R. Walker, C.G. McKamey, J.L. Wright, C.A. Carmichael, D.J. Larson, and M.K. Miller, Intermetallic reinforced Cr alloys for high-temperature use, Materials at High Temperatures, 16 (1999) 189-193.

[174] J. Schlichting and S. Neumann, GeO_2/SiO_2-glasses from gels to increase the oxidation resistance of porous silicon containing ceramics, Journal of Non-Crystalline Solids, 48 (1982) 185-194.

[175] P.K. Bachmann, D.U. Wiechert, and T.P.M. Meeuwsen, Thermal expansion coefficients of doped and undoped silica prepared by means of PCVD, J. Mater. Sci., 23 (1988) 2584-2588.

[176] J. Schlichting and S. Neumann, GeO_2/SiO_2-glasses from gels to increase the oxidation resistance of porous silicon containing ceramics, Journal of Non-Crystalline Solids, 48 (1982) 185-194.

[177] B. Pieraggi and R.A. Rapp, Chromia Scale Growth in Alloy Oxidation and the Reactive Element Effect, J. Electrochem. Soc., 140 (1993) 2844-2850.

[178] A.M. Huntz and S.C. Tsai, Diffusion in oxide scales: application to Cr_2O_3 scales, Journal of Materials Science Letters, 13 (1994) 821-825.

[179] S.C. Tsai, A.M. Huntz, and C. Dolin, Diffusion of18-O in massive Cr_2O_3 and in Cr_2O_3 scales at 900C and its relation to the oxidation kinetics of chromia forming alloys, Oxid Met, 43 (1995) 581-596.

[180] S.C. Tsai, A.M. Huntz, and C. Dolin, Growth mechanism of Cr_2O_3 scales: oxygen and chromium diffusion, oxidation kinetics and effect of yttrium, Materials Science and Engineering: A, 212 (1996) 6-13.

[181] E.M. Levin, C.R. Robbins, and H.F. McMurdie, System Cr_2O_3-SiO_2, Phase Diagrams for Ceramists, American Ceramic Society, Columbus, Ohio, 1 (1964) 130.

[182] J.W. Evans and S.K. Chatterji, Kinetics of the Oxidation and Nitridation of Silicon at High Temperatures, J. Phys. Chem., 62 (1958) 1064-1067.

[183] M. Micoulaut, L. Cormier, and G. Henderson, The structure of amorphous, crystalline and liquid-GeO_2, Journal of Physics: Condensed Matter, 18 (2006) R753.

[184] G.S. Henderson, D.R. Neuville, B. Cochain, and L. Cormier, The structure of GeO_2-SiO_2 glasses and melts: A Raman spectroscopy study, Journal of Non-Crystalline Solids, 355 (2009) 468-474.

[185] B. Nestler and A.A. Wheeler, A multi-phase-field model of eutectic and peritectic alloys: numerical simulation of growth structures, Physica D: Nonlinear Phenomena, 138 (2000) 114-133.

[186] W. Haitao, W. Yuqing, Y. Huashun, and M.G. Zhifu, Effects of composite scale on high temperature oxidation resistance of Fe-Cr-Ni heat resistant alloy, Research & Development, (2009).

[187] Y.S. Touloukian, R.K. Kirby, R.E. Taylor, and P.D. Desai, Thermophysical Properties of Matter: Thermal Expansion Metallic Elements and Alloys, DTIC Document, 1975.